



저작자표시-비영리-변경금지 2.0 대한민국

이용자는 아래의 조건을 따르는 경우에 한하여 자유롭게

- 이 저작물을 복제, 배포, 전송, 전시, 공연 및 방송할 수 있습니다.

다음과 같은 조건을 따라야 합니다:



저작자표시. 귀하는 원저작자를 표시하여야 합니다.



비영리. 귀하는 이 저작물을 영리 목적으로 이용할 수 없습니다.



변경금지. 귀하는 이 저작물을 개작, 변형 또는 가공할 수 없습니다.

- 귀하는, 이 저작물의 재이용이나 배포의 경우, 이 저작물에 적용된 이용허락조건을 명확하게 나타내어야 합니다.
- 저작권자로부터 별도의 허가를 받으면 이러한 조건들은 적용되지 않습니다.

저작권법에 따른 이용자의 권리는 위의 내용에 의하여 영향을 받지 않습니다.

이것은 [이용허락규약\(Legal Code\)](#)을 이해하기 쉽게 요약한 것입니다.

[Disclaimer](#)

공학박사 학위논문

**Synthesis of Bimetallic Nanomaterials for
Stretchable Biomedical Device and
Radioprotective Agent**

방사선보호제와 신축성 의료소자로의 활용을 위한 이중금속
나노재료의 제조

2019년 8월

서울대학교 대학원
화학생물공학부
한 상 인

Abstract

**Synthesis of Bimetallic
Nanomaterials for Stretchable
Biomedical Device and
Radioprotective Agent**

SangIhn Han

School of Chemical and Biological Engineering

The Graduate School

Seoul National University

Nanomaterials have been extensively studied in various fields such as medicine, catalysis, stretchable device to utilize their unique properties. In medical applications, toxicity of nanomaterials is the most crucial issue. The effective circumvention strategy is to maximize nanomaterials performance so that therapeutic concentration can be lowered to minimize the toxicity. In catalytic applications, lowering the working concentration of catalysts by boosting their performance or developing cheaper element catalysts with improved performance is effective approach for developing cost effective catalysts. For stretchable device applications, using high-performing filler materials with high conductivity, stretchability and biocompatibility is the key factor in maximizing performance of stretchable device. Recent study focuses on the synthesis of bimetallic nanomaterials which consists of two different elements. By combining two elements, nanomaterials can boost their catalytic performance or overcome the drawbacks of monometallic nanomaterials alone.

Following the Introduction chapter, Chapter 2 describes the highly conductive, stretchable and biocompatible nanocomposite using Ag-Au core sheath nanowire for bioelectronics. Constructing wearable and

implantable devices requires conductive, stretchable and biocompatible materials. However, obtaining composites that simultaneously fulfil these requirements is challenging due to a trade-off between conductivity and stretchability. To this end, ultralong gold-coated silver nanowires (bimetallic Ag-Au nanowires) is synthesized. Owing to the high aspect ratio and percolation network of the Ag–Au bimetallic nanowires, the nanocomposites exhibit an optimized conductivity of $41,850 \text{ S cm}^{-1}$ (maximum of $72,600 \text{ S cm}^{-1}$). The thick gold sheath formation on surface of silver nanowire prevents oxidation and silver ion leaching, overcoming the drawbacks of silver nanowire alone. Wearable and implantable soft bioelectronics devices built from the Ag-Au nanocomposite demonstrated successful integration with human skin and swine heart.

In Chapter 3, I present heterostructured ceria-manganese oxide nanocrystals as an antioxidant for mitigation of acute radiation syndrome. Nanomaterials with catalytic activities exhibit inherent antioxidant property and therefore attract significant interests for their potential therapeutic applications in reactive oxygen species (ROS)-related diseases. However, due to the potential toxicity of inorganic

nanomaterials, it is highly desired to reduce therapeutic dose by improving their catalytic activity. The heterostructured ceria-manganese oxide nanocrystals ($\text{CeO}_2/\text{Mn}_3\text{O}_4$) are synthesized and they exhibited powerful antioxidant property. The Mn_3O_4 layer formed on the surface of ceria nanocrystals is epitaxially strained, resulting in the tuning of the surface catalytic reactivity. Moreover, increased oxygen vacancies on the surface of $\text{CeO}_2/\text{Mn}_3\text{O}_4$ enhance the efficiency of surface oxygen adsorption. These synergistic effect between two metal oxides boosts catalytic performance. We utilize $\text{CeO}_2/\text{Mn}_3\text{O}_4$ as a radio-protectant that can prevent acute radiation syndrome (ARS) caused by total body irradiation (TBI). In the human intestinal organoid (hIO) model, $\text{CeO}_2/\text{Mn}_3\text{O}_4$ successfully protect regenerative intestinal stem cells without causing significant radiation-induced transcriptional modulations. Furthermore, low dose of $\text{CeO}_2/\text{Mn}_3\text{O}_4$ improves survival rate from TBI of lethal dose in mouse model by significantly mitigating both hematopoietic and gastrointestinal manifestations. These findings highlight the great potential of $\text{CeO}_2/\text{Mn}_3\text{O}_4$ for radio-protectant where ARS can be prevented with very low therapeutic dose derived from their remarkable antioxidant property.

Keywords: nanoparticle, biomedical application, bimetallic nanomaterial, core-shell nanowires, radioprotection, organoid, stretchable device, nanocomposite.

Student number: 2014-30265

Contents

Chapter 1. Bimetallic nanomaterials for nanoenzyme and stretchable device application	1
1.1 Introduction.....	1
1.2 Nanomaterials as antioxidant nanoenzyme.....	4
1.2.1 Ceria nanoparticles as antioxidant nanoenzyme and their applications.....	5
1.2.2 Other nanomaterials for antioxidant nanoenzyme and their applications	12
1.2.3 Bimetallic nanomaterials for improving catalytic performance.....	17
1.3 Nanomaterials for stretchable device application	22
1.3.1 Carbon-based nanomaterials	23
1.3.2 Metal-based nanomaterials.....	25

1.3.3	Bimetallic nanomaterials for improving device performance.....	31
1.3.4	Application for stretchable devices.....	35
1.4	Dissertation overview	41
1.5	References.....	43

Chapter 2. Highly conductive, stretchable and biocompatible nanocomposite using Ag-Au core sheath nanowire for bioelectronics 51

2.1	Introduction.....	51
2.2	Experimental section.....	54
2.3	Result and discussion.....	71
2.4	Conclusion	120
2.5	References.....	122

Chapter 3. Heterostructured ceria-manganese oxide nanocrystals as an antioxidant for mitigation of acute radiation syndrome	128
3.1 Introduction.....	128
3.2 Experimental section.....	131
3.3 Result and discussion.....	144
3.4 Conclusion	187
3.5 References.....	189
Bibliography	192
국문 초록 (Abstract in Korean).....	195

List of Figures

- Figure 1.1.** A model of the reaction mechanism for the dismutation of superoxide by cerium oxide nanoparticles 7
- Figure 1.2.** Optimal doses of ceria nanoparticles reduced infarct volumes and the rate of ischemic cell death in vivo 8
- Figure 1.3.** Infarct volume and ischemic cell death in vivo..... 9
- Figure 1.4.** Triphenylphosphonium-conjugated ceria nanoparticles that localize to mitochondria and suppress neuronal death.... 10
- Figure 1.5.** Schematic illustrations of ceria NP, TPP-ceria NP, cluster-ceria NP and their ROS scavenging reactions..... 11
- Figure 1.6.** Characterization and GPx-like activity of Vanadium oxide nanowires 14
- Figure 1.7.** Schematic illustration of peroxidase-like activity induced cytotoxicity by iron oxide nanoparticles 15
- Figure 1.8.** The Mn_3O_4 nanozyme with remarkable redox modulatory

effects	16
Figure 1.9. Ceria–zirconia (CZ) NPs utilized as therapeutic models of in vitro inflammation and in vivo sepsis	19
Figure 1.10. Elemental maps of Pt–Cu bimetallic nanoparticle precursors and their ORR activity.....	20
Figure 1.11. Structure analysis and electrocatalytic performance of PtPb nanoplates	21
Figure 1.12. Conductivity flow chart of various types of conductive fillers based on their dimensions.....	28
Figure 1.13. Carbon based conductive fillers	29
Figure 1.14. Metal based conductive fillers.....	30
Figure 1.15. Stretchable Conductive Composites from Cu– Ag Nanowire Felt.....	33
Figure 1.16. TEM image and SAED pattern of Cu–Ni NWs	34
Figure 1.17. Elastomeric polymer LED and stretchable photodetector	38

Figure 1.18. Stretchable optoelectrophysiological probe and Epicardial mesh	39
Figure 1.19. Hyper-stretchable elastic-composite energy harvester and Stretchable self-powered patchable sensor	40
Figure 2.1. Fabrication of Ag-Au nanocomposite	76
Figure 2.2. Synthesis of ultra-long Ag nanowires	77
Figure 2.3. . HAADF-STEM image of the Ag-Au NWs with reaction solution at different pH.....	78
Figure 2.4. Illustration of the solvent drying and phase separation process.....	79
Figure 2.5. Conductivity plot with material categorization.....	80
Figure 2.6. Optical camera image, modulus and conductivity of the Ag-Au nanocomposite before heat rolling press	81
Figure 2.7. Optical camera image, stretchablility and conductivity of Ag-Au nanocomposite after heat rolling press.....	82
Figure 2.8. Characterization of Ag-Au nanowires.....	83

Figure 2.9. Oxidation resistance of Ag-Au nanowires	84
Figure 2.10. Effect of length of nanowires and Ag-Au nanowires wt% on conductivity	85
Figure 2.11. Oxidation resistance of Ag-Au nanocomposite	86
Figure 2.12. Scanning electron microscope (SEM) image of phase separation of Ag-Au nanocomposite	90
Figure 2.13. Computer simulation of the phase separation effect	91
Figure 2.14. Conductivity change of the Ag-Au nanocomposite under tensile strain.....	92
Figure 2.15. Changes of Young's modulus Ag-Au nanocomposite film according to the fraction of hexylamine.....	93
Figure 2.16. Map showing stretchability and conductivity of the nanocomposite at different weight fractions	94
Figure 2.17. Graphs showing conductivity and stretchability of Ag-Au nanocomposite after heat rolling-press	95
Figure 2.18. Graphs showing conductivity and stretchability of Ag-Au nanocomposite at different weight ratios of Ag-Au NW and	

SBS.....	96
Figure 2.19. ICP-MS analysis of Ag ions released.....	99
Figure 2.20. Confocal microscope image of H9C2 cells and CCD-986sk cells after exposure to DMEM extracts.....	100
Figure 2.21. MTT assay and ICP-MS analysis in various organs	101
Figure 2.22. Histological analyses of Ag-Au nanocomposite	102
Figure 2.23. Optical camera image of a multifunctional wearable electronic patch	105
Figure 2.24. Optical camera images show the wearable device can be stretched	106
Figure 2.25. Impedance of the Ag-Au nanocomposite electrode at the skin/electrode interface	107
Figure 2.26. EMG signals measured during electrical stimulation ...	108
Figure 2.27. Temperature profiles and resistance change under applied strain of heating elements.....	109
Figure 2.28. Infrared camera images	110

Figure 2.29. 3D cardiac MRI image of a swine heart.....	114
Figure 2.30. Schematic illustrating and optical image of cardiac mesh	115
Figure 2.31. Optical camera image of implanted cardiac mesh on a swine heart.....	116
Figure 2.32. Representative intracardiac electrograms and voltage map in swine model	117
Figure 2.33. Surface ECG and intracardiac electrograms recording.	118
Figure 2.34. Representative surface ECG presents different QRS configurations.....	119
Figure 3.1. STEM image and FFT patterns of CeO ₂ /Mn ₃ O ₄	148
Figure 3.2. XRD patterns of CeO ₂ and CeO ₂ /Mn ₃ O ₄	149
Figure 3.3 XAS analysis of thin and thick Mn ₃ O ₄ shell	150
Figure 3.4 Ce 3d XPS spectra showing the oxidation state of Ce	151
Figure 3.5 Visible Raman spectra show the heterostructure of defective CeO ₂ and strained Mn ₃ O ₄	152

Figure 3.6. UV Raman spectra show the presence of higher degree of O- vacancies in CeO ₂ /Mn ₃ O ₄ than in CeO ₂	153
Figure 3.7. O 1s XPS spectra were fitted with O _{latt} , O _{ads} and O _{surf}	154
Figure 3.8. H ₂ -TPR curves comparing CeO ₂ , CeO ₂ /Mn ₃ O ₄ , and Mn ₃ O ₄	155
Figure 3.9. CVs for H ₂ O ₂ reduction and oxygen reduction.....	156
Figure 3.10. Hydrodynamic size of CeO ₂ /Mn ₃ O ₄ in PBS	157
Figure 3.11. Confocal image of cystic stage hIOs and visualization of ROS levels.....	163
Figure 3.12. Apoptotic rate of hIOs using caspase 3/7 assay	164
Figure 3.13. Morphology analysis of hIOs after IR.....	165
Figure 3.14. Number of genes transcriptionally up- or down-regulated are expressed using venn diagram.....	166
Figure 3.15. Hierarchical clustering based on expressional similarity is expressed as a dendrogram.....	167
Figure 3.16. Log ₂ fold transcriptional changes of total mRNAs are	

scatter plotted against expressional volume	168
Figure 3.17. Gene expression of hIOs after irradiation expressed as heat map	169
Figure 3.18. <i>In vivo</i> toxicity analysis by measuring weight changes and histology analysis in various organs.....	174
Figure 3.19. Timeline for in vivo radioprotection assays.	175
Figure 3.20. Kaplan meier survival graph after TBI.....	176
Figure 3.21. Serum IL-1b, IL-6, TNF-a levels after irradiation	177
Figure 3.22. MDA levels in plasma	178
Figure 3.23. MDA levels in five critical organs	179
Figure 3.24. Acute blood ROS level was estimated by quantifying plasma MDA levels	180
Figure 3.25. Intracellular ROS in BMC after irradiation.....	181
Figure 3.26. Visualization of villus using H&E staining.....	182
Figure 3.27. Visualization of proliferative stem cells in crypts	183
Figure 3.28. Number of organoids formed per 1000-seeded crypts ..	184

Figure 3.29. Long term toxicity analysis of crypt number and fibrotic change..... 185

Figure 3.30. Histology analysis of long term toxicity in key organs. 186

Chapter 1. Introduction:

Bimetallic nanomaterials for nanoenzyme and stretchable device application

1.1 Introduction

In recent years, nanomaterials have attracted enormous attention as a cutting edge technology in physics, biology, catalysis, medicine and materials science owing to their interesting properties as well as utility.^[1]

In medicine, nanomaterials are widely employed as nanoenzyme (nanomaterials with enzyme-like characteristics) due to their catalytic activities. These catalytic activities mimic those of natural redox enzymes such as peroxidase, oxidase, catalase and superoxide dismutase.^[2] Although nanoenzymes have many advantages over natural enzymes in terms of cost, stability and massive production, the issue of their innate toxicity remains unsolved. The ultimate goal is to improve the catalytic performance, enabling an effective treatment with minimal dose.

In materials science, especially for stretchable device application, carbon-, polymer-, and metal-based nanomaterials with elastomeric

polymers are widely employed as conductive fillers. Silver nanowires (Ag NWs), among other materials, gained much attention as a promising filler material for enhancing the electrical and mechanical properties of stretchable conductive nanocomposites due to their intrinsically high electrical conductivity and long structural dimensions.^[3] However, direct exposure of human tissues to the Ag ions that leach out from Ag nanowires has potentially adverse health effects.^[4] Due to the high oxidation tendency of Ag, Ag nanowires are highly corrosive in biological environments, limiting their applications in bioelectronics.^[5] Bimetallic nanomaterials have attracted enormous attention in that regard for improving the performance or overcoming drawbacks of monometallic nanomaterials.^[1] Bimetallic nanomaterials are formed by the combination of two different metals and can be synthesized in various shape, size and structure. For nanoenzyme application, using bimetallic nanoparticles can improve catalytic activities through ensemble, strain, or ligand effect.^[6] Through those improvements, treatment of diseases in medical application using bimetallic nanoenzyme is possible with minimal dose, which can reduce the risk of toxicity. In stretchable device application, surface of Ag NW can be coated with noble gold metal to produce Ag-Au bimetallic NW. The inert

gold shell ensures that the nanowires are biocompatible and resistant to oxidation while maintaining high electrical conductivity and stretchability. Therefore, improving performance or overcoming drawbacks of monometallic nanomaterials using bimetallic nanomaterials is necessary to broaden the applications of nanomaterials in catalytic nanoenzymes and stretchable devices.

1.2 Nanomaterials as antioxidant nanoenzyme

Generally, reactive oxygen species (ROS) are produced as byproduct of normal physiological process in aerobic organisms, and the concentration of ROS is controlled by antioxidant defense system such as super dismutase (SOD), catalase (CAT), glutathione peroxidase (GPx).^[7] However, overproduction of ROS may cause oxidative stress and result in various ROS-related diseases.^[8] Recently, nanomaterials with enzyme-like properties, such as ceria nanoparticles, Mn_3O_4 nanoparticles, iron oxide nanoparticles, and vanadium oxide nanowires gained significant interest due to their ability to remove ROS and treat ROS-related diseases.^[9] In the following chapters, ceria nanoparticles and other nanomaterials as antioxidant nanoenzyme and their applications towards ROS-related diseases will be described. Furthermore, boosting antioxidant performance using bimetallic nanomaterials will also be discussed.

1.2.1 Ceria nanoparticles as antioxidant nanoenzyme and their applications

Ceria nanoparticles have gained much attention owing to their potential ability to act as antioxidant to treat ROS-related diseases.^[10] The ceria nanoparticles that are less than 5 nm are reported to have powerful antioxidant activity because the nanoparticles have high portion of Ce³⁺ (reduced) state on their surface. ROS are scavenged by autocatalytic redox cycle between Ce³⁺ (reduced) and Ce⁴⁺ (oxidized) states and the antioxidant effect of ceria nanoparticles are maintained for a sustained period (Figure 1.1).^[11] These properties were successfully applied to cells *in vitro* and superoxide (O₂⁻) and hydrogen peroxide (H₂O₂) were removed through SOD and catalase mimetic activities. A recent study demonstrated that ceria nanoparticles protected neuron cells from ischemic stroke injury in an *in vivo* rat model (Figure 1.2).^[12] During the ischemic periods, ROS were generated, accumulated and induced oxidative damage. Neurovascular units were destroyed during oxidative damage and the brain function was stopped.^[13] Therefore eliminating excessive ROS in cerebrum can be a critical strategy for mitigating ischemic stroke. In this report, ceria nanoparticles targeted the damaged region by disruption of blood-brain barrier after ischemia and an optimal

dose of ceria nanoparticles were able to reduce the ischemic brain damage (Figure 1.3).^[12] Treatment of neurodegenerative diseases is another important application of ceria nanoparticles. A β -induced mitochondrial dysfunction through overproduction of ROS is known as a possible cause of Alzheimer's disease.^[14] Therefore reducing ROS using ceria nanoparticles can be an effective strategy to treat the disease. In a recent study, triphenylphosphonium-conjugated ceria nanoparticles that target mitochondria, were able to reduce neuronal death in a 5XFAD transgenic Alzheimer's disease mouse model by mitigating gliosis and mitochondrial damage (Figure 1.4).^[15] Another important neurodegenerative disease is Parkinson's disease. Kwon et al. demonstrated that Parkinson's disease could be treated by three different types of ceria nanoparticles targeted at mitochondrial, intracellular or extracellular ROS (Figure 1.5).^[16] Triphenylphosphonium-conjugated ceria nanoparticles were able to scavenge mitochondrial ROS and 300 nm sized ceria nanoparticle clusters were used to target extracellular ROS.

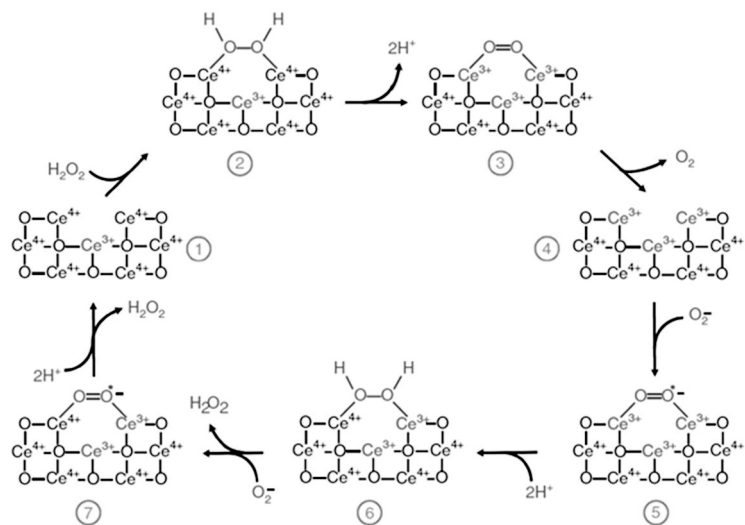


Figure 1.1. A model of the reaction mechanism for the dismutation of superoxide by cerium oxide nanoparticles.^[11]

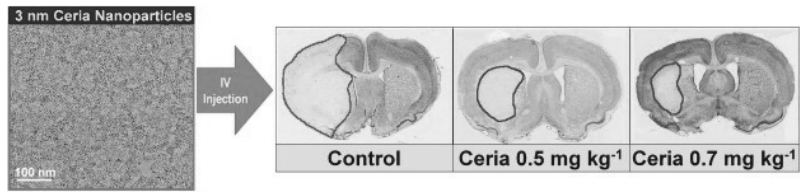


Figure 1.2. Optimal doses of ceria nanoparticles reduced infarct volumes and the rate of ischemic cell death in vivo.^[12]

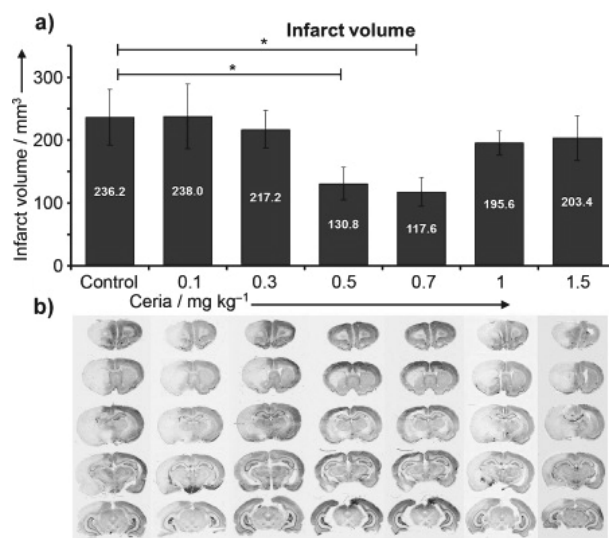


Figure 1.3. Infarct volume and ischemic cell death in vivo a) 0.5 and 0.7 mgkg⁻¹ ceria nanoparticles considerably reduce infarct volumes b) Brain slices from anterior (top) to posterior (bottom).^[12]

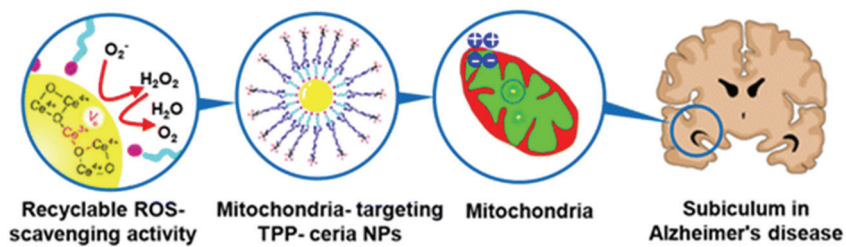


Figure 1.4. Triphenylphosphonium-conjugated ceria nanoparticles that localize to mitochondria and suppress neuronal death in a 5XFAD transgenic Alzheimer's disease mouse model.^[15]

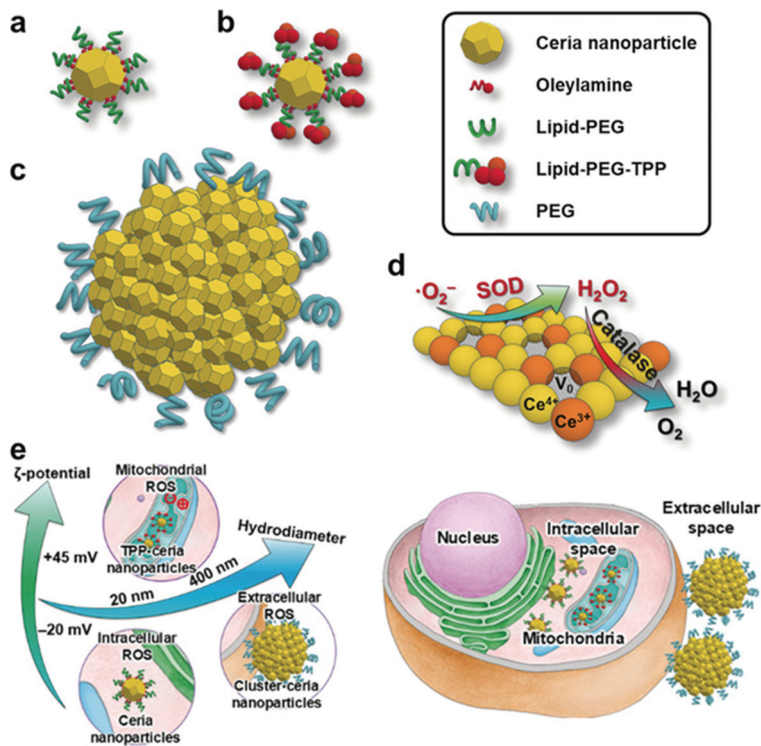


Figure 1.5. Schematic illustrations: a) Ceria NP. b) TPP-ceria NP. c) Cluster-ceria NP d) ROS scavenging reactions based on the SOD- and catalase-mimetic activities of ceria NPs. e) Cellular localization-dependent ROS scavenging activities of ceria, TPP-ceria, and cluster-ceria NPs.^[16]

1.2.2 Other nanomaterials for antioxidant nanoenzyme and their applications

Other than ceria nanoparticles, various kinds of nanomaterials are reported to mimic enzyme-like properties. For example, V_2O_5 nanowires mimic the antioxidant enzyme glutathione peroxidase by using cellular glutathione (Figure 1.6).^[17] During the excessive production of ROS, V_2O_5 nanowires are internalized into cells of various organs and reduce the ROS level through enzyme-like activity. These V_2O_5 nanowires have therapeutic potential to prevent diseases including cardiac disorders, neurological conditions and aging. Iron oxide nanoparticles show pH-dependent peroxidase-like, and catalase-like activities in intracellular environment (Figure 1.7).^[18] When iron oxide nanoparticles are taken up by the cells, their peroxidase-like activity could catalyze H_2O_2 to produce harmful hydroxyl radicals in acidic condition. However, no hydroxyl radicals were produced in neutral cytosol mimicking condition where H_2O_2 was decomposed into H_2O and O_2 through catalase-like activities of iron oxide nanoparticles. Mn_3O_4 can mimic three major enzymes, SOD, catalase and GPx (Figure 1.8).^[18] The multi-enzyme activity is size- and morphology-dependent.^[19] These Mn_3O_4 nanoparticles were able to protect cells from MPP⁺ (1-methyl-4-phenylpyridinium) induced

cytotoxicity, which indicates that the nanoparticles have therapeutic potential towards ROS-mediated neurological disorders.

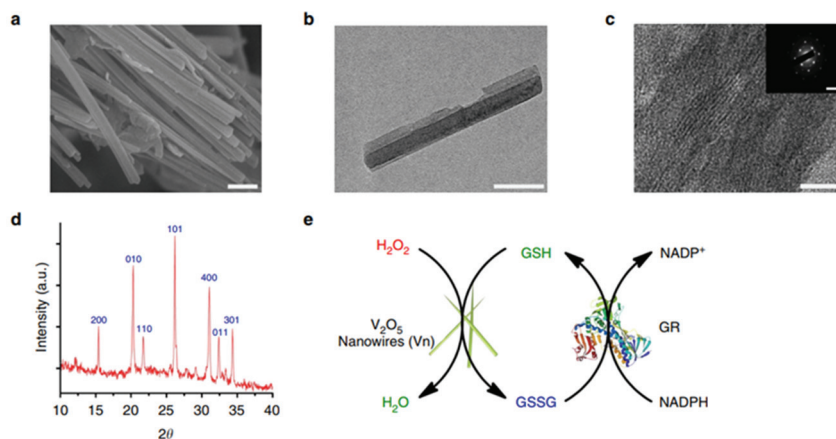


Figure 1.6. Characterization and GPx-like activity of Vn. a) A SEM image of Vn b) TEM image of Vn. c) High-resolution TEM (HRTEM) image of Vn d) Powder X-ray diffraction (XRD) of Vn e) Schematic diagram depicting the GPx-like antioxidant activity of Vn and GSH recycling by GR.^[17]

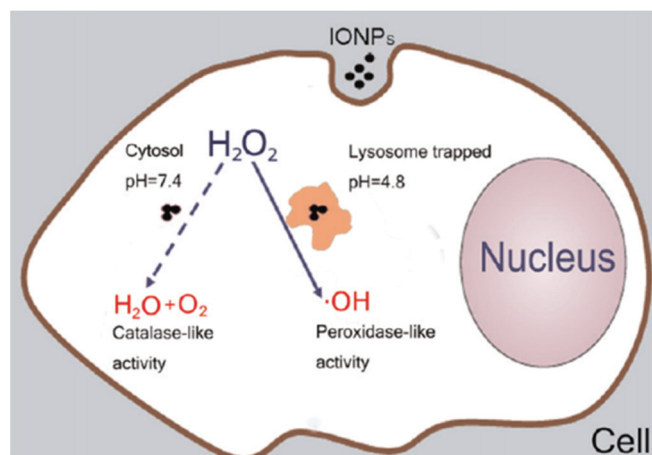


Figure 1.7. Schematic illustration of peroxidase-like activity induced cytotoxicity by IONPs.^[18]

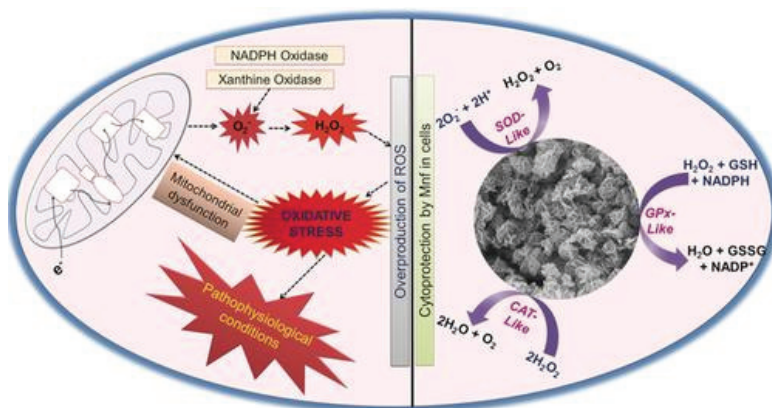


Figure 1.8. The Mn_3O_4 nanozyme (Mnf) shows a remarkable redox modulatory effect in human cells by mimicking the three major enzymes catalase (CAT), glutathione peroxidase (GPx) and superoxide dismutase (SOD).^[18]

1.2.3 Bimetallic nanomaterials for improving catalytic performance

For biomedical application of inorganic nanoparticles, toxicity is the major obstacle for clinical translation. An effective solution is to lower the therapeutic concentration by maximizing catalytic reactivity so that we can achieve maximum therapeutic efficacy with minimal dose. Recently many approaches were developed to boost catalytic performance of nanomaterials through combining two or more different elements. For example, Zr^{4+} ions are incorporated into ceria nanoparticles to improve SOD-like and catalase-like activities (Figure 1.9).^[20] Because ionic radius of Zr^{4+} is smaller than those of Ce^{4+} and Ce^{3+} ions (0.097 and 0.114 nm, respectively), lattice strain can be relieved where ionic radius has increased after conversion of Ce^{4+} to Ce^{3+} . As a result, Zr^{4+} incorporated ceria nanoparticles exhibit higher Ce^{3+}/Ce^{4+} ratio and faster regeneration of Ce^{3+} compared to pristine ceria nanoparticles. Another approach to tuning catalytic performance is to synthesize core-shell nanomaterials. Strasser et al. reported tuning catalytic performance of Pt-Cu bimetallic nanoparticles by modifying the surface strain (Figure 1.10).^[21] The platinum-rich shell exhibits compressive strain and the induced strain was able to tune the catalytic properties. Biaxial strain, in addition to the compressive strain, can

improve catalytic performance. Bu et al. demonstrated that platinum-lead/platinum core/shell nanoplate catalysts exhibit large biaxial strains and boost catalytic performance (Figure 1.11).^[22] Generally, tuning the surface oxygen adsorption energy through compressive lattice strain is an effective strategy to boost catalytic performance. In this report, large biaxial tensile strains of PtPb/Pt core-shell nanoplates were able to improve catalytic performance.

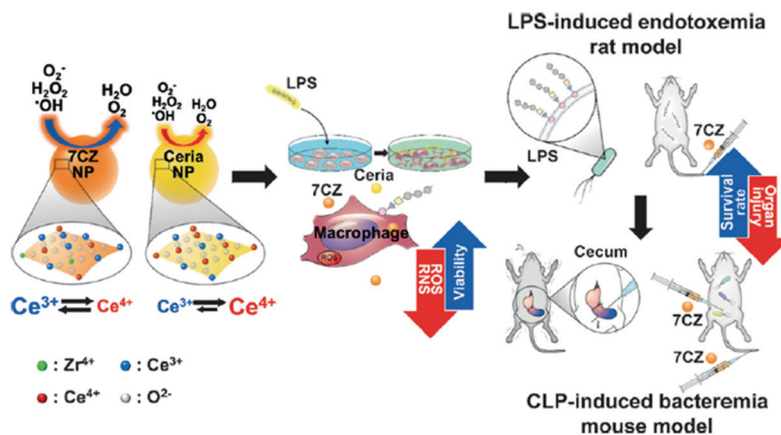


Figure 1.9. Ceria–zirconia (CZ) NPs utilized as therapeutic nanomedicine in models of in vitro inflammation and in vivo sepsis.^[20]

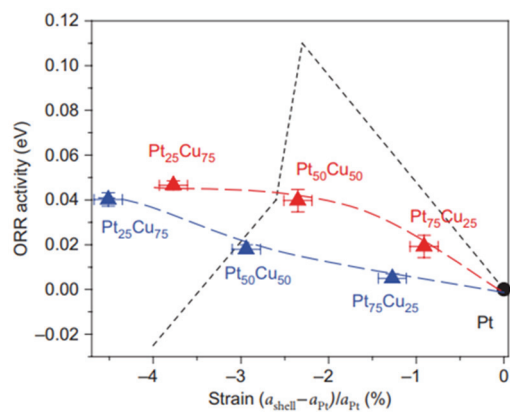
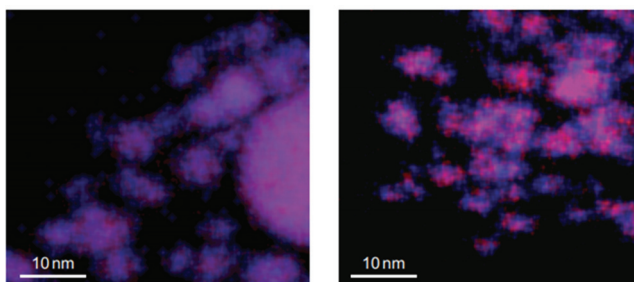


Figure 1.10. Elemental maps of Pt–Cu bimetallic nanoparticle precursors and relationships between electrocatalytic ORR activity and lattice strain.^[21]

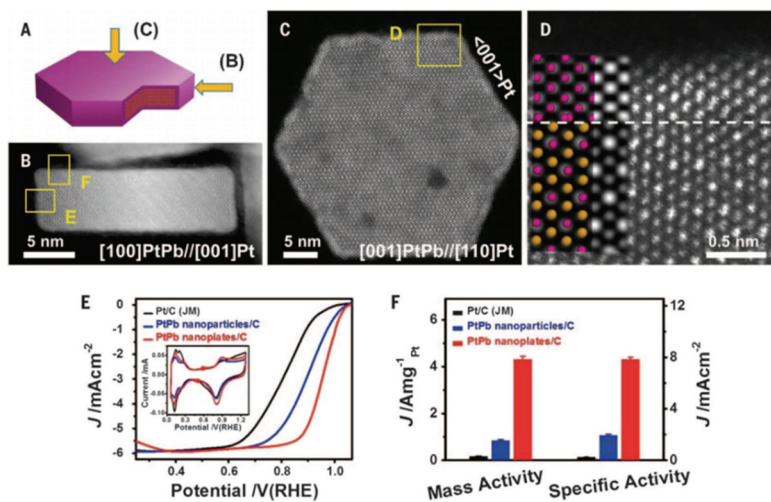


Figure 1.11. Structure analysis and electrocatalytic performance of PtPb nanoplates. a) A model of one single hexagonal nanoplate, b) HAADF-STEM image from in-plate view, c) HAADF-STEM image from out-of-plate view d) is a high-resolution HAADF image from the selected area in (c). e) ORR polarization curves and (f) specific and mass activities of different catalysts.^[22]

1.3 Nanomaterials for stretchable device application

Soft wearable electronic systems are opening up many new opportunities for novel consumer electronics, biomedical devices^[23, 24], and human-friendly electronics.^{25, 26]} Within these stretchable electronic systems, various components such as sensors,^[27] optoelectronic devices,^[28] and energy harvesters^[29] are interconnected via stretchable conductors. The quality of these stretchable interconnections is thus highly influential in determining the signal transfer speed, power consumption, and overall system performance of these products. Therefore, high performance stretchable conductors have attracted significant attention from researchers in the field of materials and device development.^[30] Examples of stretchable interconnections include conductive films such as gold,^[31, 32] aluminum, and indium tin oxide (ITO)^[33, 34] that have been patterned into special coil-like^[13] or serpentine-shaped designs^[35, 36] via top-down photolithography processes. Neutral mechanical plane designs^[37] and pre-strained wavy structures^[38] have also been applied to minimize fractures and mechanical failures of stretchable electrodes under external strains. Despite the outstanding stretchability and enhanced robustness under deformations that these strategies provide, the intrinsic rigidity of the aforementioned conducting materials may still

result in their mechanical failures such as microcracks under a large localized strain. Conductive fillers are essential components that determine both the electrical and mechanical performance of stretchable composites. Particular emphasis is given to the conductivity (measured in S/cm) of composites which strongly depends on the structural dimensions and intrinsic conductivity of the incorporated conducting filler materials (*e.g.*, carbon-, polymer-, and metal-based materials) (Figure 1.12). In this section, the electrical conductivity of various stretchable conductors fabricated with several types of conductive fillers are compared and discussed.

1.3.1 Carbon-based nanomaterials

The use of carbon-based conducting filler materials has been at the center of academic and industrial research in the field over the past decades. Some key benefits of carbon-based fillers include their relatively low cost of production and outstanding mechanical properties. Until now, carbon black, graphene flakes, and carbon nanotubes (CNTs) have been the most widely used carbon-based conductive filler materials in stretchable conductive nanocomposites.

Carbon black fillers have already been employed in commercial conductive composites.^[39] For example, carbon black particles mixed with polydimethylsiloxane (PDMS) have been used to yield a conductive rubber material.^[40] Nevertheless, the conductivity of such a rubber is not high because of the low intrinsic conductivity of the carbon black particles themselves (Figure 1.13a). These carbon black composites possess a high-resistivity which is strain-dependent and used in pressure sensor applications. It is because contacts of the conductive particles are reorganized when placed under such strains.^[41] However, higher conductivity is desired in many other applications such as electrodes and interconnections. Graphene flakes have thus gained popularity due to their better electrical and mechanical properties over carbon black fillers for these applications.^[42] 3D foam-like graphene macrostructures (graphene-foam) were synthesized by the template-directed chemical vapor deposition method.^[43] Composites of this graphene-foam and PDMS exhibited both reliable electrical performance and flexibility under strain^[44] (Figure 1.13b).

Amongst carbon-based materials, CNTs show the highest performance in terms of both conductivity and stretchability. As a representative example, 1D ultra-long single-walled carbon nanotubes (SWNTs) have

been dispersed in fluorinated copolymer rubbers with the incorporation of ionic liquids via jet-milling process.^[45] The resulting SWNT-based composites exhibit a maximum conductivity of 102 S/cm and a maximum stretchability of 118 % (Figure 1.13c). These properties allow stable electrical interconnections to be achieved between electronic devices on curved and deformable surfaces.

1.3.2 Metal-based nanomaterials

Despite the popularity of carbon- and polymer-based stretchable conductors, the low intrinsic conductivity of these materials is a major hurdle in many applications. Alternatively, metal-based materials including gold (Au) nanoparticles,^[46] silver (Ag) nanoparticles,^[47] Au nanosheets, Ag flakes,^[48] and Ag NWs^[49] are emerging as viable conductive fillers due to their inherently high electrical conductivity. For example, there have been attempts to use 0D Au nanoparticles as conductive fillers (Figure 1.14a).^[47] Au nanoparticles were used in tandem with positively-charged polyurethane (PU), which complemented the negatively charged citrate-capped Au nanoparticles, and enabled a successful deposition of Au nanoparticles via a layer-by-layer (LBL) assembly. Despite the difficulty of forming percolation

networks with 0D nanoparticles, the Au nanoparticles could yield their own electrical percolation networks through dynamic self-organization under stressed conditions. However, the LBL process only applies to charged polymers, limiting its wider applications. Furthermore, it is challenging to use these techniques in interconnection applications, such as electronic circuits, due to difficulties in the patterning process. Meanwhile, 2D Au nanosheets and rubber composites have been used in stretchable electrodes. In particular, multilayers of Au nanosheets transferred onto ecoplex exhibit a mechanical stability up to $\epsilon = 60\%$ and $\epsilon = 140\%$ in longitudinal and transverse directions, respectively (Figure 1.14b).^[50] Furthermore, the stretchability of the Au nanosheet electrodes can be enhanced through the use of SBS (styrene-butadiene-styrene) electrospun elastomer fibers as a substrate.^[51] Multiple layers of Au nanosheets on the SBS fiber mat maintained a higher degree of stability even after repetitive stretching when compared with similar silicone substrates. Although metal-based nanoparticles and nanosheets have been investigated for use as stretchable conductors due to their high intrinsic electrical conductivity, their low aspect ratio requires that many contact junctions be present. This in turn leads to an increase in contact resistance within the composite. In response to this, metallic nanowires,

specifically Ag NWs, have recently gained much attention thanks to their high intrinsic conductivity, aspect ratio, and ductility. As shown in Figure 1.14c,^[52] composites of Ag NWs and elastomeric block-copolymer exhibit significantly higher conductivity than other conductive filler materials, in the range of 10,000 S/cm or higher.

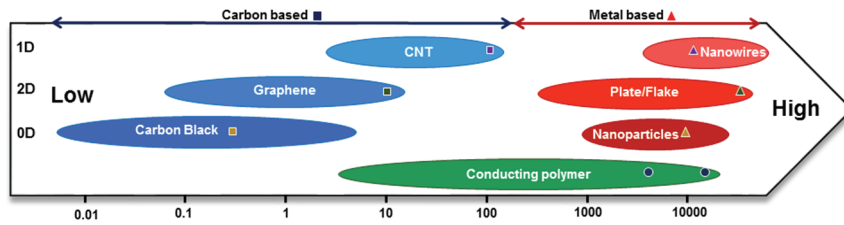


Figure 1.12. Conductivity flow chart of various types of conductive fillers based on their dimensions.

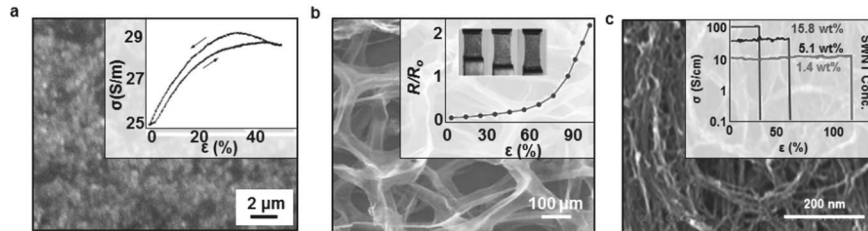


Figure 1.13. a) SEM image of carbon black powders. Inset presents the conductivity variation under stretching.^[40] b) SEM image of a graphene foam. Inset presents the resistance change of the composite as a function of a uniaxial tensile strain until fracture.^[44] c) SEM image of SWNTs uniformly dispersed in rubber. Inset depicts conductivity of printed elastic conductors as a function of stretchability.^[45]

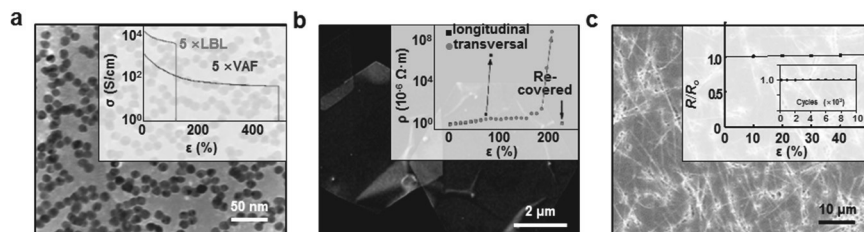


Figure 1.14. a) TEM image of Au nanoparticles. Inset presents the conductivity as a function of uniaxial strain of 5 x LBL and 5 x VAF.^[47] b) SEM image of the Au nanosheets. Inset presents the changes of electrical resistivity upon stretching the line patterned along transverse and longitudinal directions.^[50] c) SEM image of LE-Ag NW/SBS composites. Inset depicts the changes in relative resistance of an epicardial mesh with increasing tensile strains.^[52]

1.3.3 Bimetallic nanomaterials for improving device performance

Metallic conductive fillers with combination of two or more elements are used to overcome the drawbacks of monometallic nanomaterials alone such as oxidation, biocompatibility, and conductivity. In stretchable device application, the bimetallic nanomaterials that are most widely used have core-shell structure. For example, Catenacci et al. demonstrated Cu-Ag core-shell nanowire felt infiltrated with a silicone elastomer (Figure 1.15).^[53] Cu is 1000 times more abundant, 100 times less expensive, and has a carbon footprint 25 times lower than Ag.^[54] However, due to high tendency towards oxidation, Cu NW composites exhibit poor conductivity under strain. To improve stability and sustainability, Cu-Ag core shell nanowires are synthesized. The Cu-Ag NW composites exhibited high conductivity of $> 1000 \text{ Scm}^{-1}$ and stretched up to 300%. In another example, Ni is employed as shell material to reduce oxidation tendency. Chen et al. reported Cu-Ni core-shell nanowires with controllable thickness (Figure 1.16).^[55] Although capability of oxidation-resistance of Ni is high, its electrical conductivity is lower than copper.^[56] Therefore it is important to control the Ni shell thickness to retain the conductivity while oxidation-resistance is also retained. The nanowire shell of 10 nm thickness yielded an optimal

combination of conductivity and oxidation resistance where oxidation onset temperature increased from 180 °C to 270 °C after shell formation. Although silver is resistant to oxidation compared to copper, it is still oxidative compared to other noble metals. Silver ions can leak from silver nanomaterials, which can cause toxicity.

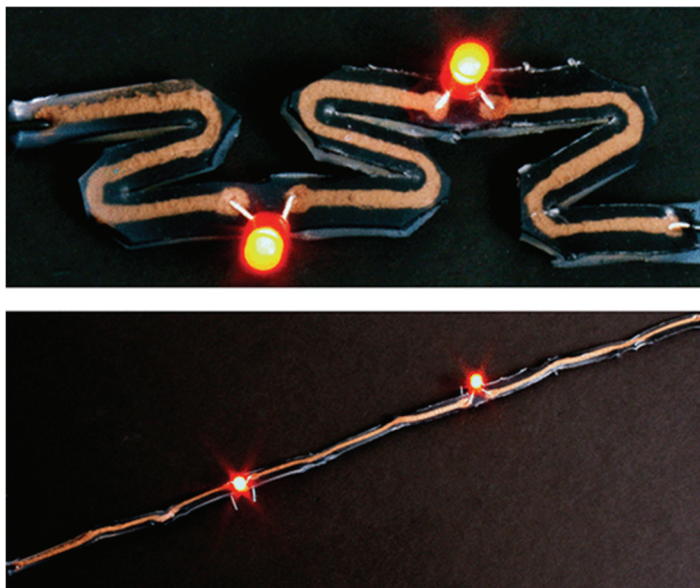


Figure 1.15. Stretchable Conductive Composites from Cu– Ag Nanowire Felt.^[53]

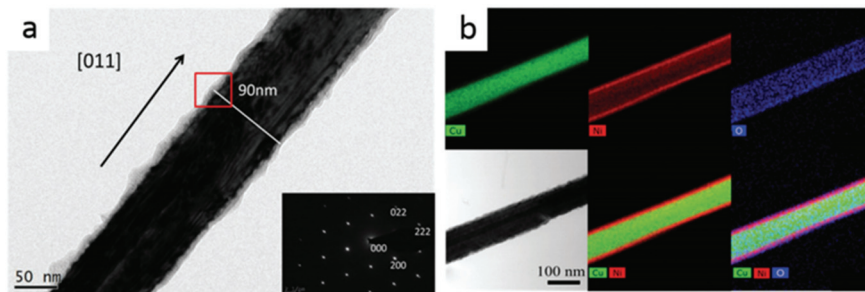


Figure 1.16. a) TEM image and SAED pattern of Cu–Ni NWs with a Cu/Ni molar ratio of 1 : 1; b) TEM image and elemental maps.^[56]

1.3.4 Application for stretchable devices

Owing to the excellent inherent conductivity and high aspect ratio of Ag NWs, Ag NW-based conductive rubbers can confer the high levels of conductivity and stretchability required in various soft electronic, optoelectronic, and energy device applications. Specific examples of device applications for use in stretchable displays, soft bioelectronics, and wearable energy harvesters are further discussed here.

In the case of optoelectronic device applications, conductive rubbers serve as electrodes connecting light emitting devices and photodetectors. For example, stretchable and transparent electrodes are made of thin Ag NW networks embedded on the surface of a poly(urethane acrylate) (PUA) matrix and integrated into an elastomeric polymer light-emitting device (ELED) (Figure 1.17a).^[57] The fabricated ELED maintains stable light-emitting performance even when it is stretched uniaxially up to 120%. Another stretchable photodetector with stable on/off behavior under mechanical distortion was developed using Ag NW electrodes and zinc oxide (ZnO) NW channel materials which were embedded and patterned into a PDMS substrate (Figure 1.17b).^[58]

The Ag NW-based conductive rubbers have also been widely used in

various wearable and implantable devices for biomedical applications. One example is the stretchable hybrid probe which used a polymer-coated Ag NW mesh and successfully achieved both optical stimulation and recordings of endogenous electrophysiological signals in the spinal cord (Figure 1.18a).^[59] The low optical transmission losses in the visible range and low impedance of the Ag NW electrodes are maintained under bending and stretching deformation, making the probe well suited to these types of measurements. An epicardial mesh has also been fabricated by blending ligand-exchanged Ag NWs with SBS rubber (Figure 1.18b).^[52] This mesh exhibits nearly identical elastic properties to those of the epicardial tissues, and its electrical conductivity is high enough to deliver a synchronized electrical stimulation over the ventricles of a rat with a myocardial infarction. Abnormal electrical activities such as ventricular tachycardia and ventricular fibrillation can also be detected via this epicardial mesh and subsequently terminated by the delivery of an electrical shock through the mesh.

Lastly, self-sustainable power configurations are key components in all wearable electronic systems. Due to advances in the stretchable energy harvester field, these components are expected to replace external power supplies for both wearable electronics and bioelectronic devices. Hyper-

stretchable energy harvesters have been developed using a piezoelectric elastic composite (PEC) and very long Ag NW electrodes (Figure 1.19a).^[60] While the PEC component generates electricity with the stretching deformation, the Ag NW electrodes integrated within the PEC component allow for a stable electrical output under large elongations, up to 200%. These stretchable energy harvesting systems are integrated into stockings to generate energy from knee flexion movements. The energy harvested from the stretchable generators can create another patchable self-powered wearable electronic strain sensor (Figure 1.19b).^[61] Multifunctional nanocomposites comprising of Ag NWs, PEDOT, and PU can be assembled to fabricate three individual components of a working device: a high-sensitivity strain sensor, a triboelectric generator (TENG), and a supercapacitor. The fabricated patchable strain sensor can operate without an external power source; the power is instead generated via a TENG, and it is subsequently stored in the supercapacitor and utilized by the strain sensor to monitor the various muscle movements of the human esophagus and trachea.

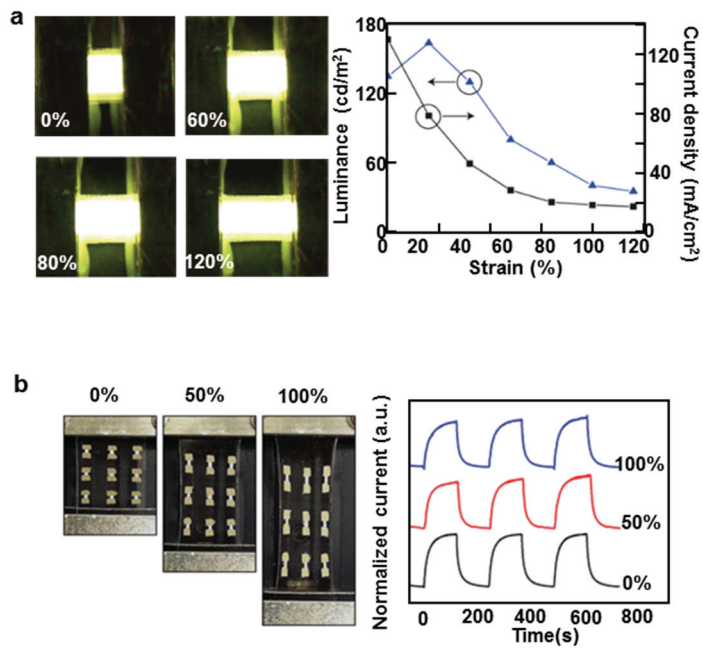


Figure 1.17. a) Elastomeric polymer light-emitting device using Ag NWs embedded in PU electrodes.^[57] b) Stretchable photodetector using ZnO NW channels and Ag NW electrodes on a PDMS substrate.^[58]

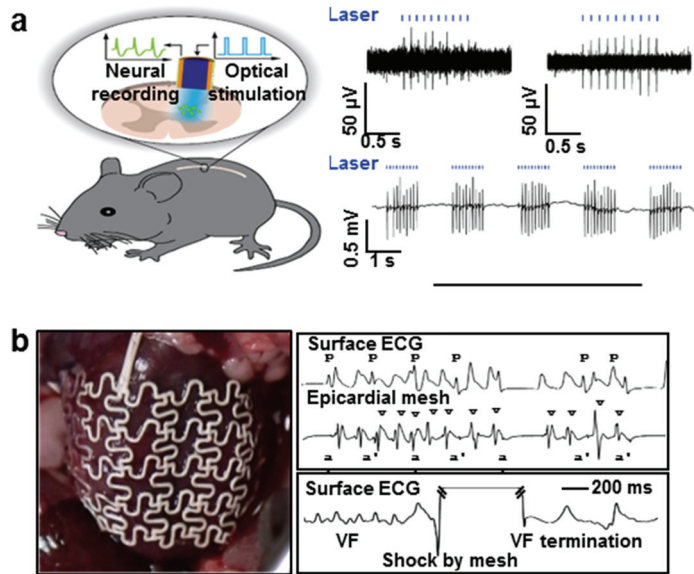


Figure 1.18. a) Stretchable optoelectrophysiological probe with integration of an Ag NW electrode for neural signal recording.^[59] b) Epicardial mesh consisting of Ag NWs and SBS composite used for recording cardiac signals and stimulating the heart.^[52]

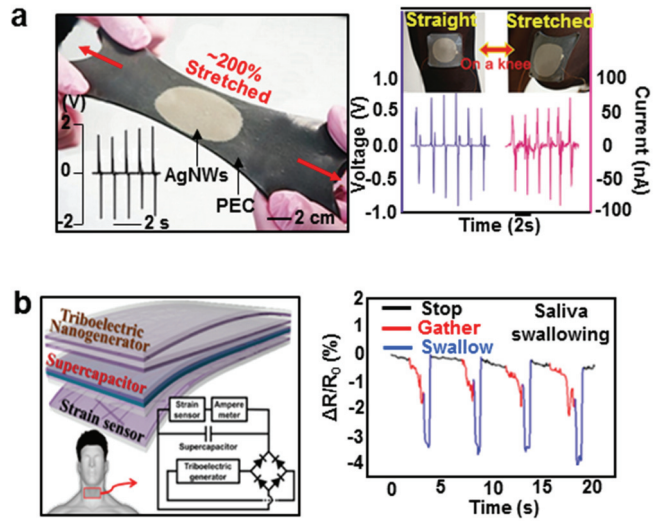


Figure 1.19. a) Hyper-stretchable elastic-composite energy harvester with integration of very long Ag NWs electrodes and the piezoelectric elastic composite.^[60] b) Stretchable self-powered patchable sensor with integration of a highly sensitive strain sensor, triboelectric generator, and supercapacitor.^[61]

1.4 Dissertation overview

Bimetallic nanomaterials gained much attention due to their improved performance or overcoming drawbacks of monometallic nanomaterials. For example in nanoenzyme application, combining two different metals can boost their catalytic performance due to increased oxygen vacancies, strain effect and so on. For stretchable device application, nanomaterials can be synthesized as bimetallic core-shell structure so that it can be resistant from oxidation.

In chapter 2, silver nanowires are encapsulated by inert gold atoms so that it is biocompatible and resistant to oxidation while maintaining high conductivity. Silver nanowires are widely used in stretchable device applications due to its high intrinsic conductivity and ease of production. However, toxic silver ions leaching from silver nanowires is very harmful especially in implantable device application. Meanwhile gold is known as inert materials with relatively high intrinsic conductivity. The surface of silver nanowires are evenly coated with gold without galvanic replacement reactions. The silver-gold nanowires exhibited high conductivity of $41,850 \text{ Scm}^{-1}$ and high stretchability of 266% while maintaining biocompatibility. The nanocomposite is successfully

incorporated into wearable and implantable soft bioelectronics that can be conformally integrated with human skin and swine heart.

In chapter 3, Mn_3O_4 nanoparticles are grown on the surface of ceria nanoparticle. The catalytic activity of Mn_3O_4 surface is tuned because of strain effect. At the same time, the surface of ceria nanoparticles exhibits a high number of oxygen vacancies. The synergistic effect can boost antioxidant performance of nanoparticles. The synthesized $\text{CeO}_2/\text{Mn}_3\text{O}_4$ are treated to human organoid model to see radioprotective efficacy. To examine protective mechanism in detail, next generation sequencing is performed using human organoid model. Furthermore, $\text{CeO}_2/\text{Mn}_3\text{O}_4$ are treated to mouse model to examine protective efficacy in vivo. The $\text{CeO}_2/\text{Mn}_3\text{O}_4$ were able to protect stem cells that resides in intestinal crypts by scavenging overly produced reactive oxygen species produced by irradiation.

1.5 References

- [1] G. Sharma, A. Jumar, S. Sharma, Mu. Naushad, R. P. Dwivedi, Z. A. Allothman, G. T. Mola, *J. King Saud Univ. – Sci.* **2017**, *31*, 257.
- [2] J. Wu, X. Wang, Q. Wang, Z. Lou, S. Lu, Y. Zhu, L. Qin, H. Wei, *Chem. Soc. Rev.* **2019**, *48*, 1004.
- [3] S. De, T. M. Higgins, P. E. Lyons, E. M. Doherty, P. N. Nirmalraj, W. J. Blau, J. J. Boland, J. N. Coleman, *ACS Nano* **2009**, *3*, 1767.
- [4] D. Mcshan, P. C. Ray, H. Yu, *J. Food Drug Anal.* **2014**, *22*, 116.
- [5] M. Yang, Z. D. Hood, X. Yang, M. Chi, Y. Xia, *Chem. Commun.* **2017**, *53*, 1965.
- [6] V. R. Stamenkovic, B. Fowler, B. S. Mun, G. Wang, P. N. Ross, C. A. Lucas, N. M. Markovic, *Science* **2007**, *315*, 493.
- [7] A. M. Pisoschi, A. Pop, *Eur. J. Med. Chem.* **2015**, *97*, 55.
- [8] J. Imlay, S. Linn, *Science* **1988**, *240*, 1302.
- [9] L. Gao, J. Zhuang, L. Nie, J. Zhang, Y. Zhang, N. Gu, T. Wang, J. Feng, D. Yang, S. Perrett, X. Yan, *Nat. Nanotechnol.* **2007**, *2*, 577.
- [10] I. Celardo, J. Z. Pedersen, E. Traversa, L. Ghibelli, *Nanoscale* **2011**, *3*, 1411.

- [11] C. Xu, X. Qu, *NPG Asia Materials* **2014**, *6*, e90.
- [12] C. K. Kim, T. Kim, I-Y. Choi, M. Soh, D. Kim, Y-J. Kim, H. Jang, H-S. Yang, J. Y. Kim, H-K. Park, S. P. Park, S. Park, T. Yu, B-W. Yoon, S-H. Lee, T. Hyeon, *Angew. Chem. Int. Ed.* **2012**, *51*, 11039.
- [13] P. H. Chan, *Blood Flow Metab.* **2001**, *21*, 2.
- [14] M. G. Bartley, K. Marquardt, D. Kirchhof, H. M. Wilkins, D. Patterson, D. A. Linseman, *J. Alzheimer's Dis.* **2012**, *28*, 855.
- [15] H. J. Kwon, M-Y. Cha, D. Kim, D. K. Kim, M. Soh, K. Shin, T. Hyeon, I. M. Jung, *ACS Nano* **2016**, *10*, 2860.
- [16] H. J. Kwon, D. Kim, K. Seo, Y. G. Kim, S. I. Han, T. Kang, M. Soh, T. Hyeon, *Angew. Chem. Int. Ed.* **2018**, *130*, 9552.
- [17] A. A. Vernekar, D. Sinha, S. Srivastava, P. U. paramasivam, P. D'Silva, G. Muges, *Nat. Commun.* **2014**, *5*, 5301.
- [18] Z. Chen, J-J. Yin, Y-T, Zhou, Y. Zhang, L. Song, M. Song, S. Hu, N, Gu, *ACS Nano* **2012**, *5*, 4001.
- [19] N. Singh, M. A. Savanur, S. Srivastava, P. D'Silva, G. Muges, *Angew. Chem. Int. Ed.* **2017**, *56*, 14267.
- [20] M. Soh, D-W. Kang, H-G. Jeong, D. Kim, D. Y. Kim, W. Yang, C. Song, S. Baik, I-Y. Choi, S-K. Ki, H. J. Kwon, T. Kim, C. K.,

Angew. Chem. Int. Ed. **2017**, *56*, 11399.

- [21] P. Strasser, S. Koh, T. Anniyev, J. Greeley, K. More, C. Yu, Z. Liu, S. Kaya, D. Nordlund, H. Ogasawara, M. F. Toney, A. Nilsson, *Nat. Chem.* **2010**, *2*, 454
- [22] L. Bu, N. Zhang, S. Guo, X. Zhang, J. Li, J. Yao, T. Wu, G. Lu, J-Y. Ma, D. Su, X. Huang, *Science* **2016**, *354*, 1410.
- [23] S. Choi, H. Lee, R. Ghaffari, T. Hyeon, D-H. Kim, *Adv. Mater.* **2016**, *28*, 4203.
- [24] I. R. Mineev, P. Musienko, A. Hirsch, Q. Barraud, N. Wenger, E. M. Moraud, J. Gandar, M. Capogrosso, T. Milekovic, L. Asboth, R. F. Torres, N. Vachicouras, Q. Liu, N. Pavlova, S. Duis, A. Larmagnac, J. Voros, S. micera, Z. Suo, G. Courtine, S. P. Lacour, *Science* **2015**, *347*, 159.
- [25] K-I. Jance, H. U. Chung, S. Xu, C. H. Lee, H. Luan, J. Jeong, H. Cheng, G-T. Kim, S. Y. Han, J. W. Lee, J. Kim, M. Cho, F. Miao, Y. Yang, H. N. Jung, M. Flavin, H. Liu, G. W. Kong, K. J. Yu, S. I. Rhee, J. Chung, B. Kim, J. W. Kwak, M. H. Yun, J. Y. Kim, Y. M. Song, U. Paik, Y. Zhang, Y. Huang, J. A. Rogers, *Nat. Commun.* **2015**, *6*, 6566.
- [26] S. Lin, H. Yuk, T. Zhang, G. A. Parada, H. Koo, C. Yu, X. Zhao,

Adv. Mater. **2016**, *28*, 4497.

- [27] Z. Liu, D. Qi, P. Guo, Y. Liu, B. Zhu, H. Yang, Y. Liu, B. Li, C. Zhang, J. Yu, B. Liedber, X. Chen, *Adv. Mater.* **2015**, *27*, 6230.
- [28] J. Kim, H. J. Shim, J. Yang, M. K. Choi, D. C. Kim, J. Kim, T. Hyeon, D-H. Kim, *Adv. Mater.* **2017**, *29*.
- [29] S. Jung, J. Lee, T. Hyeon, M. Lee, D-H. Kim, *Adv. Mater.* **2014**, *26*, 6329
- [30] J. Yang, M. K. Choi, D-H. Kim, T. Hyeon, *Adv. Mater.* **2016**, *28*, 1176.
- [31] J. Kim, D. Son, M. Lee, C. Song, J-K. Song, J. H. Koo, D. J. Lee, H. J. Shim, J. H. Kim, M. Lee, T. Hyeon, D-H. Kim, *Sci. Adv.* **2016**, *2*, e1501101.
- [32] H. Lee, C. Song, Y. S. Hong, M. S. Kim, H. R. Cho, T. Kang, K. Shin, S. H. Choi, T. Hyeon, D-H. Kim, *Sci. Adv.* **2017**, *3*, e1601314.
- [33] J-K. Song, D. Son, J. Kim, Y. J. Yoo, G. J. Lee, L. Wang, M. K. Choi, J. Yang, M. Lee, K. Do, J. H. Koo, N. Lu, J. H. Kim, T. Hyeon, Y. M. Song, D-H. Kim, *Adv. Funct. Mater.* **2017**, *27*, 1605286.
- [34] J. Lee, B. Yoo, H. Lee, G. D. Cha, H. S. Lee, Y. Cho, S. Y. Kim,

- H. Seo, W. Lee, D. Son, M. Kang, H. M. Kim, Y. I. Park, T. Hyeon, D. H. Kim, *Adv. Mater.* **2017**, *29*.
- [35] J. Kim, M. Lee, H. J. Shim, R. Ghaffari, H. R. Cho, D. Son, Y. H. Jung, M. Soh, C. Choi, S. Jung, K. Chu, D. Jeon, S-T. Lee, J. H. Kim, S. H. Choi, T. Hyeon, D-H. Kim, *Nat. Commun.* **2014**, *5*, 5747.
- [36] D. Son, S. I. Chae, M. Kim, M. K. Choi, J. Yang, K. Park, V. S. Kale, J. H. Koo, C. Choi, M. Lee, J. H. Kim, T. Hyeon, D-H. Kim, *Adv. Mater.* **2016**, *28*, 9326.
- [37] D-H. Kim, J-H, Ahan, W. M. Choi, H-S. Kim, T-H. Kim, J. Song, Y. Y. Huang, Z. Liu, C. Lu, J. A. Rogers, *Science* **2008**, *320*, 507.
- [38] M. Kaltenbrunner, T. Sekitani, J. Reeder, T. Yokota, K. Kuribara, T. Tokuhara, M. Drack, R. Schwodiauer, I. Graz, S. B. Gogonea, S. Bauer, T. Someya, *Nature* **2013**, *499*, 458.
- [39] J. T. Muth, D. M. Vogt, R. L. Truby, Y. Menguc, D. B. Kolesky, R. J. Wood, J. A. Lewis, *Adv. Mater.* **2014**, *26*, 6307.
- [40] X. Z. Niu, S. L. Peng, L. Y. Liu, W. J. Wen, P. Sheng, *Adv. Mater.* **2007**, *19*, 2682.
- [41] N. Lu, C. Lu, S. Yang, J. Rogers, *Adv. Funct. Mater.* **2012**, *22*, 4044.

- [42] C. S. Boland, U. Khan, G. Ryan, S. Barwich, R. Charifou, A. Harvey, C. Backes, Z. Li, M. S. Ferreira, M. E. Mobius, R. J. Young, J. N. Coleman, *Science* **2016**, *354*, 1257.
- [43] Z. Chen, W. Ren, L. Gao, B. Liu, S. Pei, H-M. Cheng, *Nat. Mater.* **2011**, *10*, 424.
- [44] S. Ata, K. Kobashi, M. Yumura, K. Hata, *Nano Lett.* **2012**, *12*, 2710.
- [45] T. Sekitani, H. Nakajima, H. Maeda, T. Fukushima, T. Aida, J. Hata, T. Someya, *Nat. Mater.* **2009**, *8*, 494.
- [46] Y. Kim, J. Zhu, B. Yeon, M. D. Prima, X. Su, J-G. Kim, S. J. Yoo, C. Uher, N. A. Kotov, *Nature* **2013**, *500*, 59.
- [47] R. Ma, J. Lee, D. Choi, H. Moon, S. Baik, *Nano Lett.* **2014**, *14*, 1944.
- [48] N. Matsuhisa, M. Kaltenbrunner, T. Yokota, H. Jinno, K. Juribara, T. Sekitani, T. Someya, *Nat. Commun.* **2015**, *6*, 7461.
- [49] S. De, T. M. Higgins, P. E. Lyons, E. M. Doherty, P. N. Nirmalraj, W. J. Blau, J. J. Boland, J. N. Coleman, *ACS Nano* **2009**, *3*, 1767.
- [50] G. D. Moon, G-H. Lim, J. H. Song, M. Shin, T. Yu, B. Lim, U. Jeong, *Adv. Mater.* **2013**, *25*, 2707.
- [51] M. Shin, J. H. Song, G-H. Lim, B. Lim, J-J. Park, U. Jeong, *Adv.*

- Mater.* **2014**, *26*, 3706.
- [52] J. Park, S. Choi, A. H. Janardhan, S-Y. Lee, S. Raut, J. Soares, K. Shin, S. Yang, C. Lee, Ki-W. Kang, H. R. Cho, S. J. Kim, P. Seo, W. Hyun, S. Jung, H-J. Lee, N. Lee, S. H. Choi, M. Sacks, N. Lu, M. E. Josephson, T. Hyeon, D-H. Kim, H. J. Hwang, *Sci. Transl. Med.* **2016**, *8*, 344ra86.
- [53] M. J. Catenacci, C. Reyes, M. A. Cruz, B. J. Wiley, *ACS Nano* **2018**, *12*, 3689.
- [54] T. G. Gutowski, S. Sahni, J. M. Allwood, M. F. Ashby, E. Worrell, *Philos. Trans. R. Soc.* **2013**, *371*, 20120003.
- [55] J. Chen, J. Chen, Y. Li, W. Zhou, X. Feng, Q. Huang, J-G. Zheng, R. Liu, Y. Ma, W. Huang, *Nanoscale* **2015**, *7*, 16874.
- [56] A. R. Rathmell, M. Nguyen, M. Chi, B. J. Wiley, *Nano Lett.* **2012**, *12*, 3193.
- [57] J. Liang, L. Li, X. Niu, Z. Yu, Q. Pei, *Nat. Photonics* **2013**, *7*, 817.
- [58] C. Yan, J. Wang, X. Wang, W. Kang, M. Cui, C. Y. Foo, P. S. Lee, *Adv. Mater.* **2014**, *26*, 943.
- [59] C. Lu, S. Park, T. J. Richner, A. Derry, I. Brown, C. Hou, S. Rao, J. Kang, C. T. Moritz, Y. Fink, P. Anikeeva, *Sci. Adv.* **2017**, *3*, e1600955.

- [60] C. K. Jeong, J. Lee, S. Han, J. Ryu, G-T. Hwang, D. Y. Park, J. H. Park, S. S. Lee, M. Byun, S. H. Ko, K. J. Lee, *Adv. Mater.* **2015**, *27*, 2866.
- [61] B-U. Hwang, J-H. Lee, T. Q. Trung, E. Roh, D-I. Kim, S-W. Kim, N-E. Lee, *ACS Nano* **2015**, *9*, 8801.

Chapter 2. Highly conductive, stretchable and biocompatible nanocomposite using Ag-Au core sheath nanowire for bioelectronics

2.1 Introduction

Conductive and stretchable nanocomposites based on the percolation network of conductive nanomaterials in elastomeric media¹⁻³ offer a viable alternative to rigid and brittle conventional metallic materials such as gold^{4,5} and indium tin oxide⁶. These soft conductive nanocomposites have been applied in e-skin^{7,8}, wearable bioelectronics^{9,10}, and implantable biomedical devices^{11,12}. Ultralong one-dimensional (1D) metal nanowires are favorable filler materials for these conductive nanocomposites because their high aspect ratio lowers the percolation threshold of filler materials, resulting in higher conductivity¹³. Silver nanowires (Ag NWs) are particularly popular because they are highly conductive and can be easily produced in large scale^{13,14}. However, direct exposure of human tissues to Ag ions that leach out from Ag NWs can have potential adverse health effects¹⁵. Due to the high oxidation

tendency of silver, Ag NWs are highly corrosive in biological environments, limiting their applications in bioelectronics¹⁶. Furthermore, obtaining nanocomposites that are both stretchable and highly conductive is challenging. For example, while increasing the content of filler materials may improve conductivity, this often causes the composite to lose softness and stretchability^{17,18}. Plasticizers may be introduced to improve stretchability, but this in turn lowers the conductivity^{19,20}.

Here, we present the highly conductive, biocompatible, and soft Ag-Au nanocomposites consisting of ultralong gold-coated silver nanowires dispersed in poly(styrene-butadiene-styrene) (SBS) elastomer. The high aspect ratio of Ag NWs confers high conductivity while the inert gold shell ensures that the NWs are biocompatible and resistant to oxidation. The phase separation during the low temperature drying process induces microstructures in the nanocomposite, which increases the softness of the material. Cytotoxicity tests and histological analysis confirm that the Au sheath effectively improves biocompatibility by preventing silver ion leaching and protecting Ag NWs from oxidation. Using the highly conductive, biocompatible, and soft nanocomposites, we successfully fabricated wearable and implantable bioelectronic

devices for biosensing and stimulation on the human skin and swine heart.

2.2 Experimental Section

2.2.1 Synthesis of ultralong silver nanowires

Ultra-long silver nanowire was synthesized by polyol-mediated process, modified from previous study to produce longer Ag NWs¹. 0.034 M of poly-vinylpyrrolidone (PVP, MW 360k, Sigma Aldrich) in 130 ml of ethylene glycol was pre-heated at 175 °C with 260 rpm stirring in an oil bath. After the temperature was saturated, 800 µl of 4 mM copper chloride (CuCl₂·2H₂O; Sigma Aldrich) solution was added. After 10 minutes, 30 ml of 0.095 M silver nitrate (AgNO₃, Strem Chemical Inc., USA) in ethylene glycol is injected with rate of 180 ml/hr. When the injection is finished, we stop the stirring and keep the synthesis reaction for 20 minutes. As synthesized Ag NWs is diluted with water (1:4) and washed multiple times using centrifuged to remove excess PVP. Finally, Ag NWs are redispersed in water in concentration of 5 mg/ml.

2.2.2 Synthesis of Ag-Au NWs

Growth solution (gold-sulfite complex) is prepared by mixing 1.4 ml of 0.25 M hydrogen tetrachloroaurate(III) hydrate (HAuCl₄·xH₂O, Strem Chemical Inc., USA), 8.4 ml of 0.2 M sodium hydroxide (NaOH, Sigma

Aldrich), 105 ml of 0.01 M sodium sulfite (Na_2SO_3 , Sigma Aldrich), and 165 ml of H_2O , and left undisturbed for 12 hrs. A separate solution is prepared by mixing 320 ml of H_2O , 20 ml of Ag NWs (5 mg/ml), 70 ml of 5 wt% poly-vinylpyrrolidone (PVP, M_w 40,000, Sigma Aldrich), 14 ml of 0.5 M sodium hydroxide (NaOH, Sigma Aldrich), 14 ml of 0.5 M L-ascorbic acid (L-AA, Sigma Aldrich), and 3.5 ml of 0.1 M Na_2SO_3 . Subsequently, the prepared growth solution was added into the Ag NW solution to initiate the reaction and left undisturbed for 2 hrs at the room temperature. Finally, the resulting Ag-Au NWs were washed multiple times with ethanol and redispersed in dimethylformamide (DMF, Samchun Chemical). For characterization, the SEM image and cross-sectional backscattered electron image of Ag-Au NWs were obtained by Focused Ion Beam SEM (FIB-SEM, AURIGA, Carl Zeiss, Germany). HRTEM images and energy-dispersive X-ray spectroscopy (EDS) data were obtained by Cs corrected transmission electron microscope (Cs-TEM, JEM-ARM200F, JEOL, Japan).

2.2.3 Ligand exchange of Ag-Au NWs

200 mg of Ag-Au NWs is dispersed in 38 ml of N,N-Dimethylformamide (DMF, Samchun, Korea). 2 ml of 0.1 M nitrosyl tetrafluoroborate (NOBF₄, Sigma Aldrich) is added to the Ag-Au NWs solution. Subsequently, 40 ml of hexane is added to the solution. After shaking the reaction for 2 minutes, 0.6 ml of hexylamine (Sigma Aldrich) is added to the reaction solution. The ligand exchanged Ag-Au NWs are purified by ethanol and centrifuged and finally redispersed in toluene with a concentration of 30 mg/ml.

2.2.4 Preparation of the Ag-Au nanocomposite

The nanocomposite solution is prepared by mixing the SBS polymer solution (10 wt% in toluene), Ag-Au NWs (30 mg/ml in toluene), and hexylamine with the desired amounts. All weight fraction means (each component weight) / (sum of Ag-Au NWs, SBS, and hexylamine weight). The solution is dried in a glass mold under desired temperatures. After drying the solution, the Ag-Au nanocomposite is heated under 140 °C for 5 mins on a hotplate to completely evaporate the remaining solvent. Microscopy images were taken by the field emission scanning electron

microscope (FE-SEM, JSM-6701F, JEOL, Japan) and the time of flight secondary ion mass spectrometer (ToF-SIMS, TOF.SIMS-5, ION-TOF, Germany).

2.2.5 Oxidation method

Oxidation of Ag NWs and Ag-Au NWs is analyzed under condition of 1.5 M of hydrogen peroxide (H_2O_2 , Junsei Chemical Co. Ltd) in cuvette. The suspension is gently shaken for 10 s to ensure homogeneous mixing and incubated at room temperature for 3 hrs. After incubation, absorbances are taken with UV-VIS spectrophotometer (V-550, Jasco, USA) and microscopic images are taken by HRTEM (JEM-2100f, JEOL, Japan). To analyze conductivity variations of Ag-Au nanocomposite and Ag nanocomposite under oxidation condition, UV/ O_3 treatment was applied to both nanocomposites using UV/ O_3 exposure system (UV ozone cleaner, Yuiluv. co. Ltd., Korea) for 2 hrs.

2.2.6 Silver ion leaching test

For Ag ions leaching test, Ag NWs, Ag-Au NW and Ag-Au nanocomposite (1 mg/ml based on Ag concentration from inductively coupled plasma atomic emission spectrometer (ICP-AES, ICPS-1000IV, Shimadzu, Japan)) are incubated in DMEM for 3 days at 37 °C. Each solution is centrifuged and supernatant is filtered with 0.22 µm pore filters and analyzed by inductively coupled plasma mass spectrometry (ICP-MS, NexION 350D, Perkin-Elmer, USA).

2.2.7 Cell viability test

H9C2, CCD-986sk, and L929 are seeded in the 96-well plate with 10,000 cells per well and cultured for 24 hrs. Subsequently, the original DMEM is replaced by extract of samples (control; original DMEM, Ag NW, Ag-Au NW, and Ag-Au nanocomposite incubated at 37 °C in DMEM for 10 days) and incubated for another 24 hrs. 20 µl (5 mg/ml) 3-[4,5-dimethylthiazol-2-yl]-2,5-diphenyltetrazolium bromide (MTT) was added to each well and incubated at 37 °C for 4 hrs. Finally, the medium is removed and 200 µl dimethylsulfoxide is added to each well. The

absorbance was measured at 540 nm using a 96-well plate reader (Victor X4, Perkin-Elmer, USA).

2.2.8 Cell morphology analysis

H9C2 and CCD-986sk were seeded in the 35 mm glass bottom dish with ~70% confluency and cultured for 24 hrs. Subsequently, the original DMEM was replaced by extract of samples and incubated for another 24 hrs. The cells were fixed with 4 % paraformaldehyde in 1x PBS for 15-20 min and permeabilized with 0.1 % Triton X-100 in 1x PBS for 5 mins. After washing thoroughly with the PBS buffer, cells were incubated with TRITC-conjugated Phalloidin (1:100; Millipore, Billerica, MA, USA) for 50 mins. After washing thoroughly with the PBS buffer, the cells were incubated with DAPI (1:1000; Millipore, Billerica, MA, USA) for 5mins. The morphology of cells was visualized by the confocal microscopy (LSM 780, Carl Zeiss, Oberkochen, Germany).

2.2.9 Histology Analysis

Harvested organs were fixed with 4% paraformaldehyde in the PBS for 2 days and embedded in paraffin. Each paraffin was sectioned (2 μm) and stained with hematoxylin and eosin (H&E) by following the standard protocol. To visualize collagen fiber deposition in tissues, trichrome staining was performed by using Masson Trichrome Staining Kit (Sigma Aldrich).

2.2.10 Computer simulation

The coarse-grain model, which includes multi-components, was simulated using molecular dynamics (MD). The MD simulation was done using popular MD package LAMMPS² and we used dimensionless Lennard-Jones unit. Simulated system contained three components mimicking Ag-Au NWs, SBS, and hexylamine. The Ag-Au NWs was modeled as a linear chain of 10 particles. The SBS was modeled as block-copolymer including two polystyrene terminal-block composed of 5 particles each and polybutadiene center-block composed of 20 particles (i.e. linear chain of 30 particles). The hexylamine was modeled as a dimer. The system with additional hexylamine composed of 500 Ag-Au

NWs, 1,500 SBS, and 50,000 hexylamine molecules (weight ratio of NWs:SBS:hexylamine = 0.26:0.23:0.51) while the system without hexylamine composed of 500 Ag-Au NWs and 1,500 SBS (weight ratio of NWs:SBS:hexylamine = 0.5:0.5:0). Mass and diameter of constituent particles of Ag-Au NWs are higher than other particles to simulate its low mobility. The simulation was divided into two stages: The equilibration and the tensile test. Before the subsequent tensile test, the system was allowed to reach equilibrium at desired temperature and pressure. The tensile test was conducted at a temperature ($T = 0.2 \epsilon/k_B$) and zero pressure where ϵ is the unit of energy and k_B is the Boltzmann constant. The timestep is 0.01τ where τ is the unit of time, which can be reduced to $\tau = \sigma (m/\epsilon)^{1/2}$. We used 12-6 Lennard-Jones potential, properly adjusting their parameters to represent size and chemical character of the species. Especially, the parameters were set so that π - π interaction between polystyrene blocks and the hydrogen bonding interaction between amine groups became strong. The incompressibility and stiffness of Ag-Au NWs were implemented using harmonic bond and angle potential with high modulus. The finitely extensible nonlinear elastic (FENE) bond potential³ was applied to both hexylamine and SBS. The stiffness of the SBS block-copolymer chain was treated as harmonic

angle potential where the stiffness parameter was calculated from Flory's characteristic ratio⁴. The tensile behavior was investigated using the method in the work done by Hossain *et al*⁵. Two lateral boundaries perpendicular to the tensile direction were under NVT condition (constant number (N), volume (V), and temperature (T)). The snapshots of before and after tensile test are shown, which were rendered with Visual Molecular Dynamics (VMD)⁶.

2.2.11 Measurement of electrical performance of Ag-Au nanocomposite

All the electrical performances were measured using double-layered Ag-Au nanocomposite (15 mm × 3 mm) which was laminated by the heat rolling-press. Conductivity is calculated by the equation, conductivity (σ) = 1 / resistivity (ρ_0) ; ρ_0 = thickness × sheet resistance³⁹, where the sheet resistance was measured with a custom-made 4-point probe (probe: LS system, Korea; instrument: Keithley 2400, Tektronix, USA), and the thickness was measured by using SEM. For the stretching test, each end of the nanocomposite was connected to a copper wire using the silver paste and stretched after encapsulation with VHB films (VHBTM Tape 4910 Clear, 3M, USA). Stretchability and conductivity under strain were

measured using two-point-resistance and four-point resistance change respectively.

2.2.12 Heat rolling-press of Ag-Au nanocomposite

Two layers of nanocomposite were put in between ketone films and heat rolling-press was applied using a heat roll press (ETK16-486-1, Wellcos Corporation, Korea). Temperature of the rollers was set at 105 °C. For soft nanocomposite, heat rolling-press was performed until the average thickness was unchanged compared to thickness of the original nanocomposite, while for highly stretchable nanocomposite, the heat rolling-press is performed until the average thickness decrease by 15% compared to thickness of the original nanocomposite. After the process, double-layered nanocomposite was detached from the ketone film. Conductivity and stretchability were measured in the same method as above.

2.2.13 Wearable device fabrication

Metal molds with desired patterns are fabricated (iNEX JK Co., Ltd., Korea) and treated with vapor phase of trichloro(1H,1H,2H,2H-perfluorooctyl)silane (FOTS) for 1 hrs. Then, polyurethane acrylate (PUA) is poured on the metal mold and subsequently cured under UV irradiation to make a rigid PUA film. PDMS is poured on the patterned PUA film and cured. Finally, the PDMS mold with the pattern same as the metal mold is prepared. Prepared nanocomposite solution is poured onto the PDMS mold and the residual solution remaining outside the pattern is removed. Then, the solution is dried under the ambient condition, and the patterned Ag-Au nanocomposite is prepared after solvent is fully evaporated. To encapsulate the nanocomposite, two SBS layers of patterns are prepared in the same way. The electrode parts of a SBS layer are open. The nanocomposite layer is sandwiched between SBS layers and welded under heat of 140 °C for 20 min⁷. Fabricated wearable device is connected to FPCB using silver paste, and the FPCB is connected to ZIF connector on a customized PCB board to facilitate control of recording and stimulation functions.

2.2.14 Wearable skin-like bioelectronics using the Ag-Au nanocomposite

The wearable skin-like device was attached to the forearm using Tegaderm (3M, USA), and an Ag/AgCl electrode was placed on the ankle and elbow for ground. The ECG and EMG signals were measured using a data acquisition equipment (DAQ; National Instruments) with the LabVIEW software (encoded with 60 Hz notch filter). The signals were acquired with the sampling rate of 1000 Hz. 3 Hz high-pass filter, 300 Hz low-pass filter, and 59-61 band block filter were applied on the raw data to remove motion artifacts and non-physiological noises. Electrical stimulation was applied through stimulation electrodes. While applying the electrical stimulation, stimulation pulses were measured using EMG electrodes adjacent to the stimulation electrodes. Thermal stimulation was conducted by joule heating. Voltage was applied on the heating element of the wearable skin-like device by the voltage supplier (Agilent, USA). Infrared (IR) camera (Thermovision A320, FLIR system, Sweden) was used for temperature measurement. All human experiments were conducted under approval by the Institutional Review Board of the Seoul National University (approval number SNU 17-12-006).

2.2.15 Fabrication of the cardiac mesh

Metal molds with each layer pattern were fabricated. PDMS replicated molds were prepared using a previously-reported fabrication procedure of PDMS mold^{13,18}. Prepared nanocomposite solution and SBS solution were patterned on the PDMS mold for electrode layers and encapsulation layers, respectively. Then, the solution is dried under the ambient condition, and the patterned Ag-Au nanocomposite is prepared after solvent is fully evaporated. Each layer is transferred in sequence using PDMS stamp coated with 1:40 (weight ratio of curing agent to prepolymer) ratio of PDMS. For each transfer, the layers were welded under heat of 140 °C for 20 min. The multi-channel electrodes of the cardiac mesh were connected to a customized flexible printed circuit board using silver paste, which are, in turn, connected to a ZIF connector on a customized printed circuit board to record signals from each channel and control stimulation sites.

2.2.16 *In vivo* swine experiment

The research protocol was approved by the Institutional Animal Care and Use Committee and conformed to the Position of the American Heart Association on Research Animal Use. The research was performed at the Beth Israel Deaconess Medical Center, Experimental Electrophysiology

Laboratory in Boston, MA. Sedation was initiated with 1.4 mg/kg intramuscular injection of Telazol (tiletamine/zolazepam hydrochloride). Endotracheal intubation was then performed, and general anesthesia was maintained with isoflurane inhalation (1.5% – 2.5%). Ventilation was maintained between 10 and 16 breaths/min and hemodynamic assessment including heart rate, oxygen saturation, and blood pressure were continuously monitored. After median sternotomy to expose the hearts, the 3D cardiac sock mesh was implanted. Myocardial ischemia was induced by ligation of the mid-left anterior descending artery.

2.2.17 Electrophysiology study

The LabSystem Pro EP Recording System (Bard, Boston Scientific, Lowell, MA) was used for surface ECG and intracardiac electrogram (EGM) recordings. A surface 6-lead electrocardiography was used to monitor heart condition, such as heart rhythm, rate, and electrocardiogram alteration. The sampling rate was 1 kHz. Intracardiac electrograms were obtained from the multichannel electrodes of cardiac mesh. Electrical stimulation was performed at twice the pacing threshold of rectangular stimulus pulses with duration of 2 ms by a programmable

digital stimulator (Bloom DTU 215, Fisher Medical Technologies). Bipolar EGMs were filtered at 30 – 250 Hz and displayed at a sweep speed of 200 mm/s. All recordings were stored in a digital format for off-line annotation and analysis. Bipolar voltage in all EGMs was automatically measured and a voltage map was created off-line.

2.2.18 CMR imaging

In-vivo cardiac magnetic resonance (CMR) imaging was performed using a 1.5T MRI scanner (Phillips Achieva, Best, NL) with a 32-element cardiac phased-array receiver coil. During imaging, each animal was sedated, intubated, and mechanically ventilated. We acquired a 3D whole heart anatomical image using 3D steady-state free precession sequence and isotropic spatial resolution of 1.5 mm³. A T2 magnetization preparation sequence was used to improve blood-myocardium contrast. Image analysis was performed off-line. To design the implantable cardiac device, 3D rendering model of CMR imaging was created (3D slicer software v 4.7.0). For merging with intra-cardiac electrogram recordings, 3D contour segmentation was implemented manually based on consecutive slices of CMR images (ITK-snap 3.6, Penn Image

Computing and Science Laboratory, USA)⁸ and the points cloud of reconstruction image was converted 3D mesh with Poisson reconstruction (MeshLab, Visual Computing Lab, USA). The coordinates of electrode position were determined on the 3D mesh image of swine heart.

2.2.19 Construction of voltage map

The intracardiac electrograms were recorded from 35 channel of bipolar electrodes. Voltage amplitude of QRS complexes was obtained from the intracardiac electrogram one-hour following the LAD occlusion. The locations of each electrode were projected onto the epicardial surface which was reconstructed using a MRI image of the heart. Epicardial isochronal map was constructed using the voltage amplitude data interpolated from the data measured at electrode locations. For interpolating three dimensionally scattered data, the scatteredInterpolant class was used and natural neighbor interpolation algorithm was applied. Interpolation and mapping processes were performed with custom software in MATLAB (R2016b, Mathworks, Natick, MA).

2.2.20 Statistical analysis

Statistical analyses were carried out using Origin 9.0 software. One-way ANOVA analysis with Tukey's post hoc test was used for Ag ion release, cell viability and biodistribution studies. The Shapiro–Wilk test ($\alpha = 0.05$; $n \geq 3$ replicates per group) showed that there was no significant deviation from normality. Levene's test ($\alpha = 0.05$) was performed to all datasets with $n \geq 3$ replicates to test the homogeneity of variances. Sample size was selected to ensure an adequate power of 90% for Ag ion release and cell viability studies, and 75% for biodistribution studies. For the analysis of the percentage of fibrotic area, the P value was calculated by the Mann–Whitney U -test. Investigators were not blinded to the experiments and analyses, and no randomization method was used.

2.3 Result and Discussion

2.3.1 Fabrication and characterization of the Ag-Au nanocomposite

The fabrication of the microstructured Ag-Au nanocomposite requires a mixture of Ag-Au NWs decorated with hexylamine ligands, SBS elastomer, and an additional hexylamine in toluene (Figure 2.1). To obtain Ag-Au NWs, we firstly synthesized ultralong Ag NWs ($\sim 100 \mu\text{m}$) using the previous method with slight modifications (Figure 2.2)^{21,22}. For galvanic-free deposition of Au on the Ag NWs, we used sodium sulfite (Na_2SO_3) to selectively bind Au cations and consequently lower the reduction potential of Au ($E^0 = 0.111 \text{ V}$ vs. standard hydrogen electrode)²³. Because the resulting gold(I) sulfite complex ($\text{Na}_2\text{Au}(\text{SO}_3)_2$) is relatively benign to the Ag surface, ligand-assisted oxidative etching does not occur, instead Au coating is boosted. The galvanic replacement reaction is also prevented by keeping the reaction solution at pH 9. At $\text{pH} < 9$, galvanic replacement reactions occur, whereas at $\text{pH} > 9$ the Au sheath is formed without galvanic replacement reactions but irreversible aggregation occurs (Figure 2.3)²⁴. After the gold coating, the surface of Ag-Au NWs is modified with hexylamine using the previously-reported ligand exchange procedure²⁵.

To obtain the microstructured Ag-Au nanocomposite, hexylamine-decorated Ag-Au NWs, a SBS solution, and additional hexylamine in toluene are combined and casted on a glass mold under ambient conditions (Figure 2.4a). During the dry-casting and solvent-drying process, the initially homogeneous solution (Figure 2.4b left) is separated into two phases, a hexylamine-rich region containing Ag-Au NWs and a toluene-rich region containing SBS (Figure 2.4b middle). Subsequent solvent evaporation results in a microstructured Ag-Au nanocomposite composed of a Ag-Au NW-rich region and a SBS-rich region (Figure 2.4b right). When the microstructured Ag-Au nanocomposite is stretched, the Ag-Au NW rich region acts as a highly conductive electrical pathway and the SBS-rich region forms an elastic microstructured strut (Figure 2.4c). Despite the high concentration of the nanowire filler added to the nanocomposite for improved conductivity (Figure 2.5), the cushy microstructure ensures softness and stretchability (Figure 2.6). Stretchability can be further improved by heat rolling-press (Figure 2.7). These soft, highly conductive characteristics, and stable electrical performance under deformation are crucial for high performance bioelectronics^{26,27}.

We confirmed the Ag-Au NW core-sheath structure using various

electron microscopy and spectroscopy methods. Scanning electron microscopy (SEM) image in Figure 2.8a shows the nanowires are long ($\sim 100 \mu\text{m}$) and connected each other. A backscattered electron image in the inset illustrates the Ag NW core and Au sheath (highlighted in yellow) of the Ag-Au NW (before surface modification). High-resolution transmission electron microscopy (HRTEM) image of the Ag-Au NW shows a clear boundary between the heavy atomic shell (Au) and the light core (Ag) (Figure 2.8b). The lattice parameter of the outer shell confirms the crystalline structure of Au in the [111] direction (Figure 2.8b inset). Mapping the spatial distribution of Ag and Au using high-angle annular dark field scanning transmission electron microscopy (HAADF-STEM) and energy-dispersive X-ray spectroscopy (EDS) further confirmed the core-sheath structure of the Ag-Au NWs (Figure 2.8c). The smooth morphology indicates that silver etching by galvanic replacement reaction does not occur. The atomic intensity profile in a line scan of the Ag-Au NW (Figure 2.8d top) shows that the mean diameter of the NW and thickness of the Au shell are 140 nm and 35 nm, respectively (Figure 2.8d bottom).

Because oxidation and/or corrosion can increase contact resistance between nanowires and Ag NWs are vulnerable to these processes when

exposed to biofluids such as sweat²⁸, interstitial fluid²⁹, and blood¹¹, we examined the oxidation resistance of our Ag-Au NW using hydrogen peroxide (H_2O_2) as the oxidant. TEM images show that the Ag NW is heavily oxidized and corroded, while the Ag-Au NW with the protective Au shell remains intact (Figure 2.9a). The resistance against oxidation is further confirmed by UV-Vis spectra, which shows a significantly diminished extinction spectrum for Ag NWs that have undergone oxidation and an unchanged spectrum for Ag-Au NWs (Figure 2.9b).

We characterized the conductivity of the Ag-Au nanocomposite (prepared at a 60:40 weight ratio of NW:SBS;). Nanocomposites with longer NWs ($\sim 100 \mu m$) have a higher conductivity ($\sim 41,850 S/cm$) than those with shorter NWs ($25 \mu m$) (Figure 2.10a). Conductivity can be increased up to around $72,600 S/cm$ by increasing the content of Ag-Au NWs in the composite (75:25 weight ratio of NWs:SBS; Figure 2.10b). However, at such a high nanowire content, stretchability decreases. Under ultra violet and ozone (UV/O₃) treatment ($40 mW/cm^2$, 2 hours; ozone as an oxidant), the conductivity of Ag-Au nanocomposite remained unchanged, whereas the conductivity of control Ag nanocomposites (made of Ag NWs and SBS) deteriorated significantly due to oxidation (Figure 2.11a). SEM images confirm severe oxidation

of the Ag nanocomposite by UV/O₃ (Figure 2.11b top) and the inertness of the Ag-Au nanocomposite (Figure 2.11b bottom).

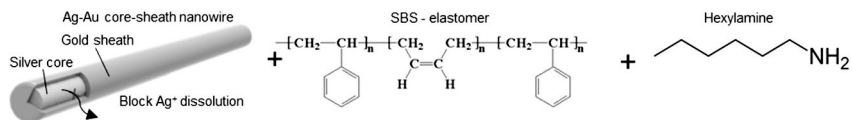


Figure 2.1. Ag-Au nanocomposite is made by combining a mixture of Ag-Au NWs decorated with hexylamine ligands, SBS elastomer, and an additional hexylamine in toluene.

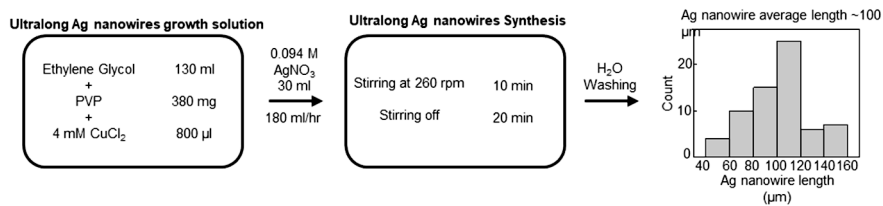


Figure 2.2. Synthesis of ultra-long Ag nanowires.

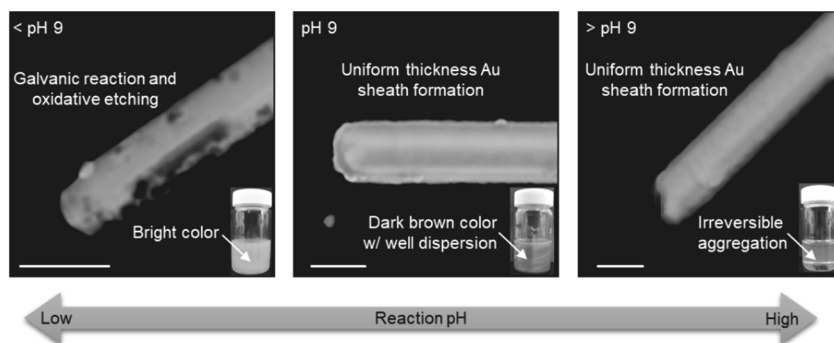


Figure 2.3. HAADF-STEM image of the Ag-Au NWs with reaction solution at low pH (< pH 9) (left), optimal pH (= pH 9) (middle), and high pH (> pH 9) (right). Each inset shows photograph image of Ag-Au NWs dispersed in DMF.

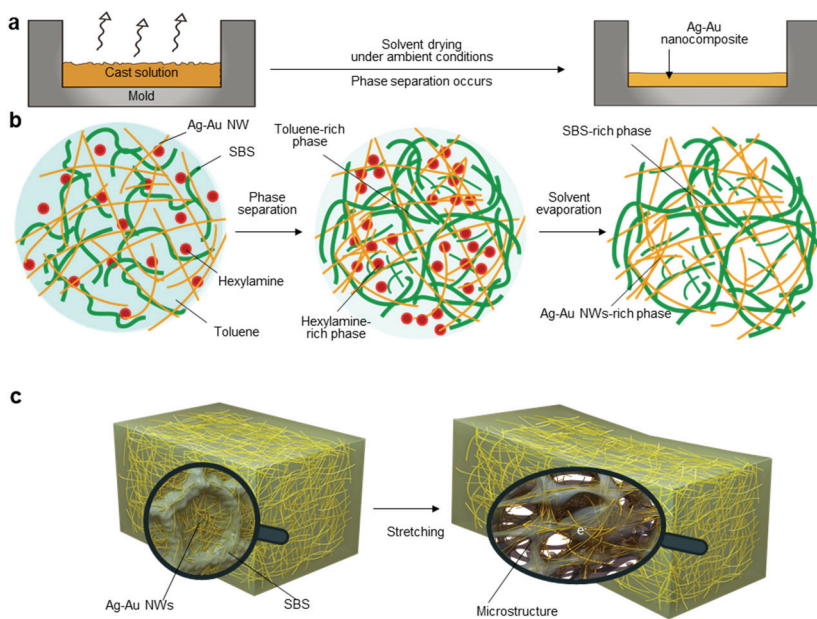


Figure 2.4. a) Illustration of the solvent drying process under ambient conditions. b) Schematic showing that the initial solution (left) is separated into a Ag-Au NW-rich phase and a SBS-rich phase during dry-casting (middle). Subsequent solvent evaporation (right) forms the microstructured Ag-Au NW nanocomposite. c) Schematic illustration of the microstructured Ag-Au nanocomposite before and after stretching.

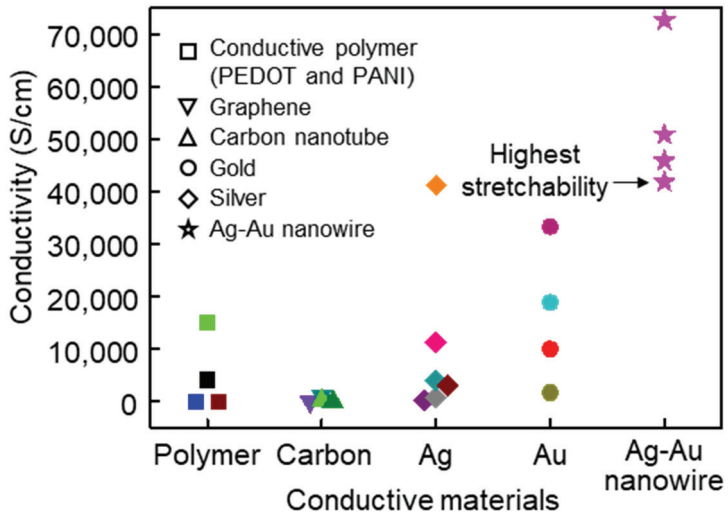


Figure 2.5. Conductivity plot with material categorization.

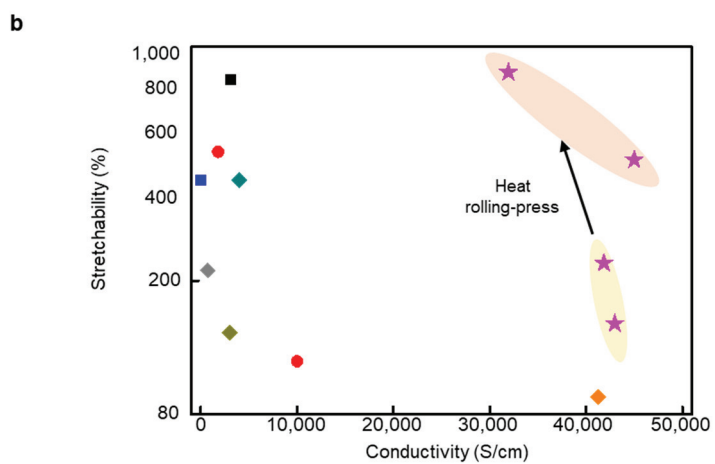


Figure 2.7. a) Optical camera image of the Ag-Au nanocomposite after the heat rolling-pressed Ag-Au nanocomposite sandwiched between the elastomeric substrates (VHB film). b) Plot of stretchability and conductivity.

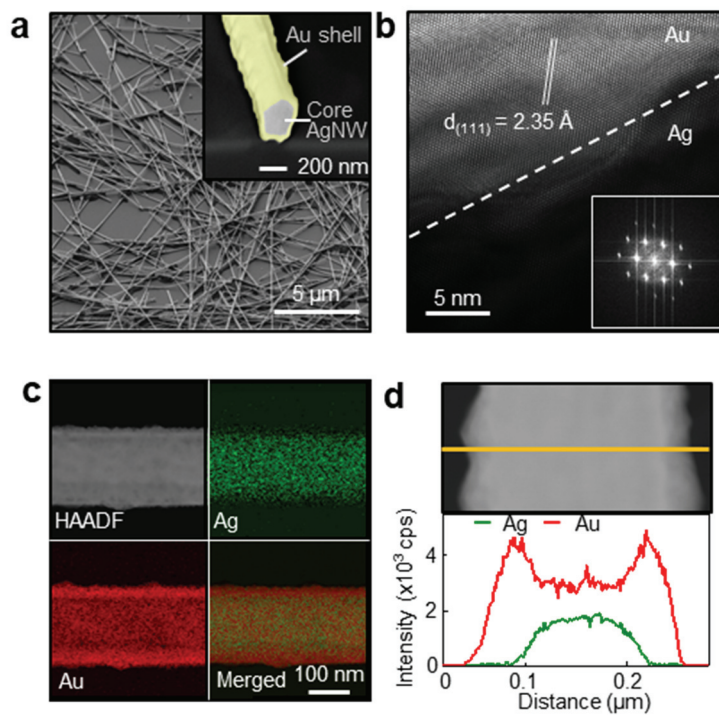


Figure 2.8. a) SEM image and inset back-scattered electron (BSE) image of Ag-Au NWs (before surface modification; Au sheath is in yellow). b) HRTEM image of the Ag-Au NW. Dash line indicates the boundary between Ag core and Au sheath. Inset: an electron diffraction pattern at the Ag-Au boundary showing the crystalline structure of Au in the [111] direction. c) EDS elemental mapping of Ag and Au in the bare Ag-Au NW, and their merged image confirm the core-sheath structure. d) EDS cross-section line scan of the Ag-Au NW shows the mean diameter of NW is 140 nm and thickness of Au shell is 35 nm.

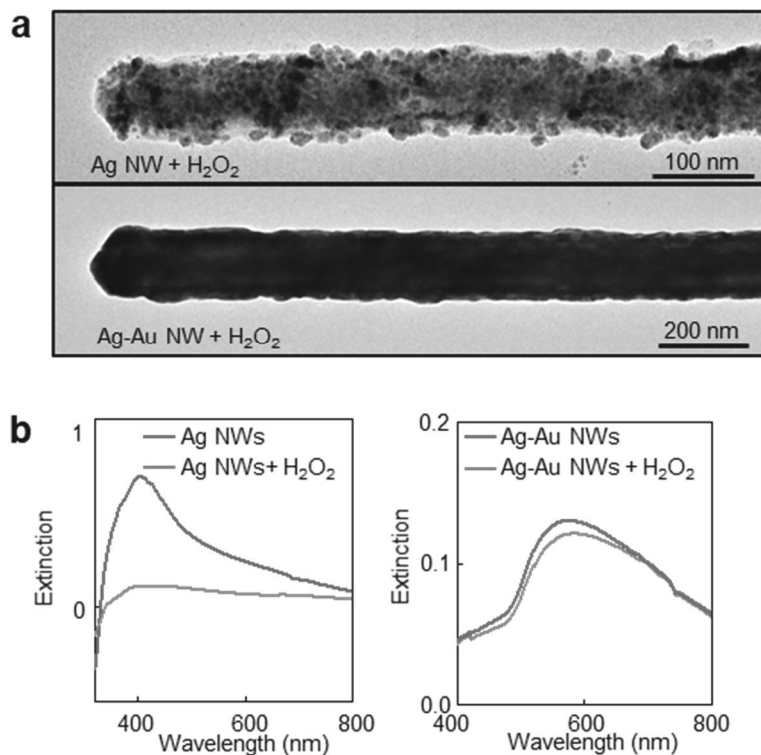


Figure 2.9. a) TEM image of the Ag NW (top) and the Ag-Au NW (bottom) treated with 1.5 M of H₂O₂. Ag-Au NW is protected against oxidation. b) UV-Vis spectra of Ag NWs (left) and Ag-Au NWs (right) after H₂O₂ treatment confirm protection of Ag-Au NWs against oxidation.

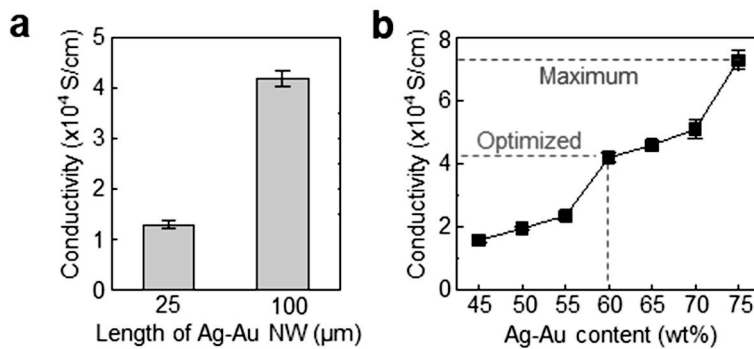


Figure 2.10. a) Graph shows that nanocomposites with longer Ag-Au NWs have higher conductivity than those with shorter NWs. b) Graph shows that the nanocomposites with higher Ag-Au NW content are more conductive than those with lower Ag-Au NW content. Maximum conductivity is 72,700 S/cm at the weight ratio of NW:SBS of 75:25 and optimized conductivity where the nanocomposite exhibits highest stretchability is 41,850 S/cm at the weight ratio of NW:SBS of 60:40.

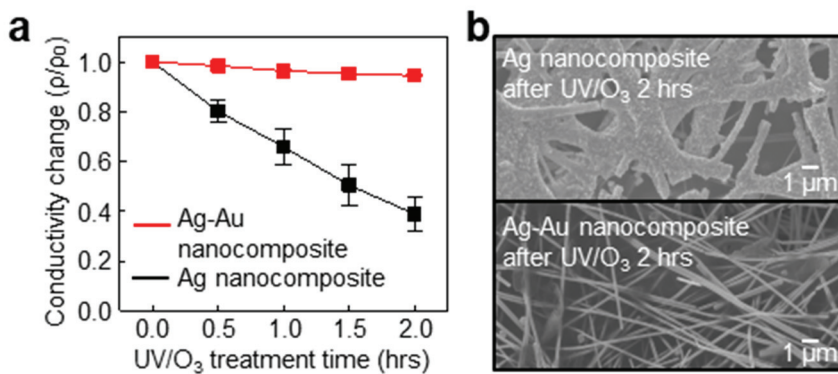


Figure 2.11. a) At the same weight ratio of NW:SBS of 80:20, conductivity of Ag-Au nanocomposite remains unchanged whereas that of Ag nanocomposite shows a decrease. All error bars represent s.e.m. b) SEM image of Ag nanocomposite (top) and Ag-Au nanocomposite (bottom) after 2 hours UV/O₃ treatment. Oxidation is prevented in Ag-Au NWs.

2.3.2 Phase separation affects the properties of the nanocomposite

The conductivity, softness, and stretchability of the Ag-Au nanocomposite are affected by phase separation, which is determined by solvent drying temperature and hexylamine concentration. We found that the room temperature solvent drying process leads to a thinner nanocomposite film with a higher density of the percolated NW network, and a more conductive nanocomposite than higher temperature processes. Room temperature drying facilitates the separation of Ag-Au NWs into hexylamine-rich regions and promotes the stabilization of SBS in toluene-rich regions. This phase separation results in the formation of microstructures and regions showing different elasticity (Figure 2.12a left). Upon stretching, a porous microstructure is observed (Figure 2.12a right). This cushion-like microstructure lowers Young's modulus and increases softness (Figure 2.12b). Computer simulation shows that local stress is distributed in the elastic SBS-rich region under stretching, while the mesh-like Ag-Au NW-rich region maintains the original percolation network (Figure 2.13). For experimental confirmation, we prepared the double-layered Ag-Au nanocomposite encapsulated in elastic substrates (VHB film), and the resistance was measured under stretching. Consequently, the microstructured Ag-Au nanocomposite (0.36:0.24:0.4;

weight fraction of Ag-Au NWs:SBS:hexylamine) fabricated at room temperature shows a conductivity of 41,850 S/cm (at 0% strain) and a stretchability of ~266%, both of which are higher than composites obtained through high temperature processes (Figure 2.14).

Another key factor that affects phase separation is the amount of hexylamine. Without hexylamine (*i.e.*, 0 wt% hexylamine), phase separation is limited and no microstructure is formed, leading to low stretchability. However, higher weight fraction of hexylamine tends to promote phase separation, and therefore, boosts softness (Figure 2.15a) and stretchability (Figure 2.15b). When the weight fraction of hexylamine is increased up to 0.4 at fixed weight ratio of 60:40 for Ag-Au NWs:SBS, Young's modulus decreases significantly while softness and stretchability increases. Based on our experimental results (22 conditions; $n = 3$) using different weight fractions of Ag-Au NWs, SBS, and hexylamine for nanocomposites made under room temperature, we made maps of conductivity and stretchability (Figure 2.16). The optimum composition to maximize stretchability, while maintaining a high conductivity of 41,850 S/cm is 0.36:0.24:0.4 weight fraction of Ag-Au NWs:SBS:hexylamine (mapped as red dotted lines in Figure 2.16 right). Applying heat rolling-press could further boost stretchability

without altering the phase-separated structure. The stretchability of the Ag-Au nanocomposite (fixed weight ratio of 60:40 for Ag-Au NWs:SBS) can be increased up to ~840%, when the weight fraction of hexylamine is increased up to 0.3 and the heat rolling-press is applied (Figure 2.17). Although the Young's modulus increases after the heat rolling-press, the stretchability is increased with increased toughness³⁰. Conductivity slightly decreases after the heat rolling-press treatment. When the weight fraction of hexylamine is 0.3, the roll-pressed Ag-Au nanocomposites exhibit stretchability of 840%, 520%, 300%, and 180% with initial conductivity of 30,000 S/cm, 38,800 S/cm, 50,600 S/cm, and 69,400 S/cm depending on the weight ratio of Ag-Au NW:SBS (60:40, 65:35, 70:30, and 75:25), respectively (Figure 2.18 and inset).

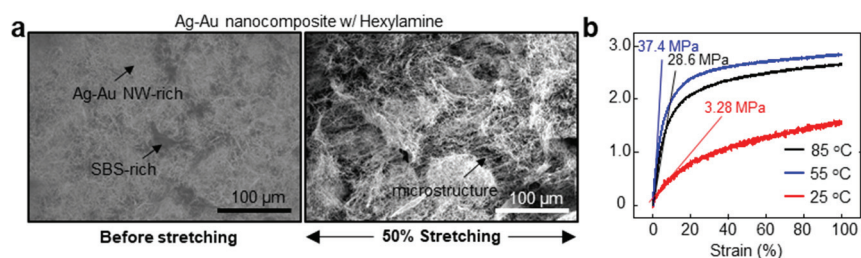


Figure 2.12. a) SEM images of the Ag-Au nanocomposite with hexylamine before (left) and after (right) stretching. Room temperature drying process promotes phase separation and formation of microstructures with unequal elasticity between the phase separated regions, allowing materials to be stretched. b) Stress-strain curve of the Ag-Au nanocomposite with hexylamine for three different solvent drying temperatures. Room temperature (25 °C) drying lowers Young's modulus and forms a softer composite.

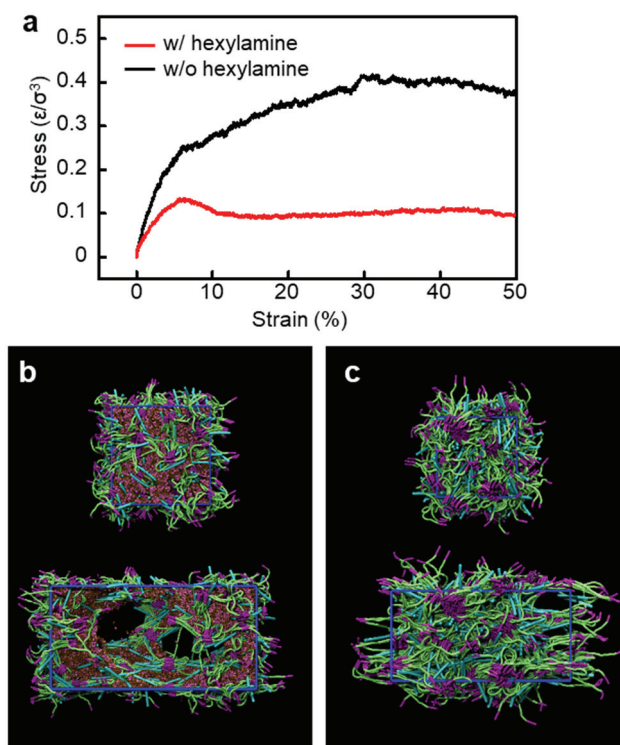


Figure 2.13. Calculated stress strain curve for Ag-Au nanocomposite with and without hexylamine. Incorporation of additional hexylamine significantly reduces the modulus. b,c, The initial configuration (top) and the deformed configuration (bottom) of nanocomposites with (b) and without hexylamine (c) under 100% tensile strain (cyan: Ag-Au nanowires, purple: polystyrene block, green: polybutadiene block, pink: amine group of hexylamine, brown: carbon chain of hexylamine, and dark blue frame: periodic box boundary).

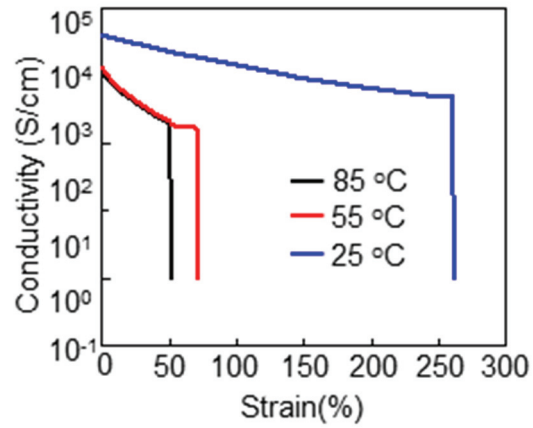


Figure 2.14. Conductivity change of the Ag-Au nanocomposite under tensile strain for three different drying temperatures. Nanocomposite obtained through room temperature drying is highly conductive and stretchable.

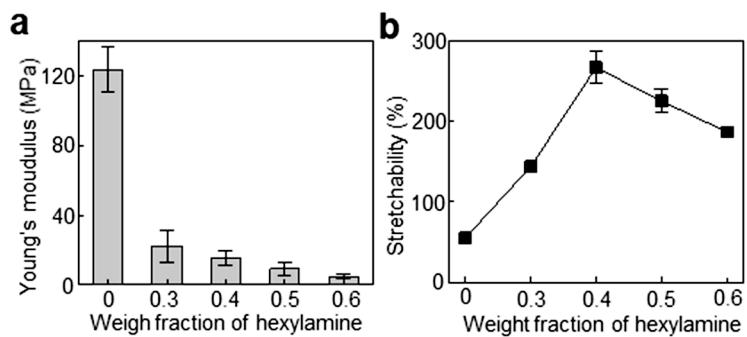


Figure 2.15. Changes of Young's modulus (**a**) and stretchability (**b**) of the Ag-Au nanocomposite film according to the fraction of hexylamine.

Weight ratio of Ag-Au NW:SBS is 60:40.

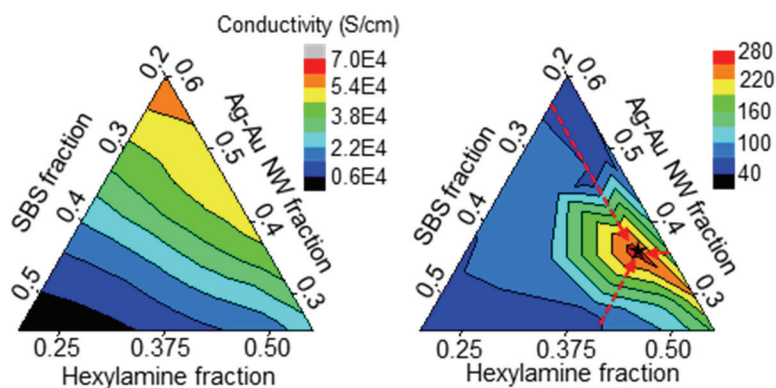


Figure 2.16. Map showing stretchability (left) and conductivity (right) of the nanocomposite at different weight fractions of Ag-Au NWs, SBS, and hexylamine. The point (0.36:0.24:0.4 weight fraction of Ag-Au NWs:SBS:hexylamine) indicated by three red dotted lines represents the optimum composition for the highest stretchability.

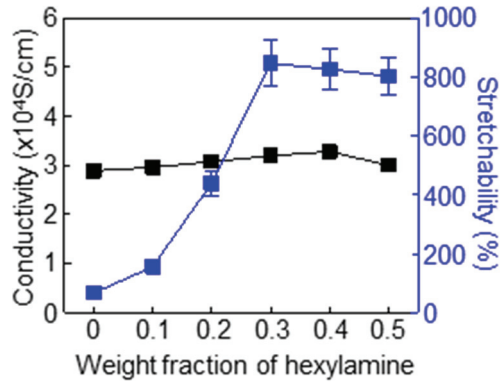


Figure 2.17. Graphs showing conductivity (left) and stretchability (right) of the Ag-Au nanocomposite at different weigh fractions of hexylamine after the heat rolling-press. The Ag-Au nanocomposite can be stretched up to ~840% when the weight fraction of hexylamine is 0.3. All weight fraction means (each component weight) / (sum of Ag-Au NWs, SBS, and hexylamine weight).

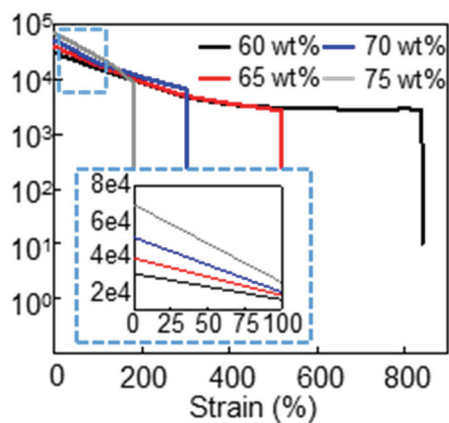


Figure 2.18. Graph showing conductivity change of the Ag-Au nanocomposites under tensile strain for the different weight ratios of Ag-Au NW and SBS at a fixed weight fraction of hexylamine of 0.3. Inset graph shows the initial conductivity and the conductivity change up to 100% applied strain.

2.3.3 Ag-Au NW composite is biocompatible

For bioelectronic applications, biocompatibility is crucial and preventing direct exposure of Ag NWs to tissues is important. We examined the effect of the Au sheath on the biocompatibility *in vitro* and *in vivo*. To test the leaching of Ag ions, Ag NWs, Ag-Au NWs, and Ag-Au nanocomposite were incubated in Dulbecco modified eagle medium (DMEM) for 3 days and the dissolution of Ag ions was analyzed using inductively coupled plasma mass spectrometry (ICP-MS). DMEM extract for Ag NWs has 5,349 ppb Ag ions. Very low concentration of Ag ions (311 ppb) was detected in the DMEM extract for Ag-Au NWs and only trace levels (65 ppb) were detected for the Ag-Au nanocomposite, indicating that the Au sheath effectively inhibits the dissolution of Ag ions (Figure 2.19). Heart myoblast (H9C2) and human skin fibroblast (CCD-986sk) cells exposed to DMEM extract from Ag NWs showed damaged actin skeleton and DNA while those exposed to extract from Ag-Au NWs and Ag-Au nanocomposite remained healthy (Figure 2.20). Furthermore, H9C2, CCD-986sk, and mouse connective tissue (L929) cells exposed to DMEM extracts from Ag NWs exhibit significantly decreased viability (Figure 2.21a). These results confirm that the Au sheath effectively protects the Ag NWs from leaching

potentially lethal Ag ions.

We further implanted the Ag nanocomposite and Ag-Au nanocomposite on the rat's heart for 3 weeks and measured the biodistribution of Ag ions in the liver, spleen, lung, and kidney using ICP-MS (Figure 2.21b). The Au sheath effectively reduces accumulation of Ag ions in all the organs. Histology analysis (Masson's trichrome staining, Hematoxylin and Eosin staining) of the cardiac muscle after 3 weeks of implantation reveals significantly less fibrotic reaction and inflammatory responses with the Ag-Au nanocomposite than the Ag nanocomposite (Figure 2.22).

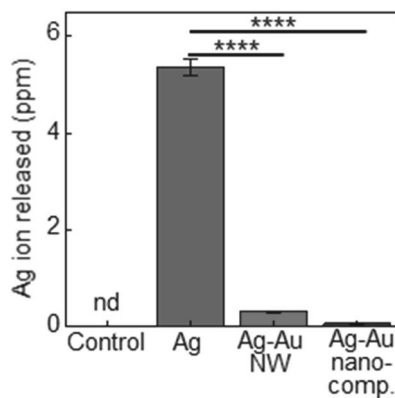


Figure 2.19. ICP-MS analysis of Ag ions released from Ag NWs, Ag-Au NWs, and the Ag-Au nanocomposite after incubating each in DMEM for 3 days. Low levels of Ag ions for Ag-Au NWs and Ag-Au nanocomposite show that the Au sheath effectively protects Ag NWs from dissolution. Data are analyzed using one-way ANOVA and are expressed as averages \pm s.e.m. ($n = 3$). Significance is set at **** $P < 0.0001$ versus the Ag NWs.

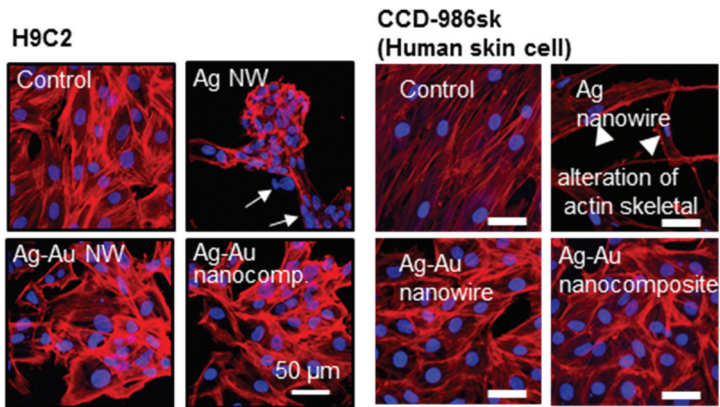


Figure 2.20. Confocal microscope image of H9C2 cells (left) and CCD-986sk cells (right) after exposure to original DMEM (control) or DMEM extracts of Ag NWs, Ag-Au NWs, and the Ag-Au nanocomposite for 24 hrs. Cells exposed to Ag NW extracts exhibit damaged (arrows) actin cytoskeleton (red) and DNA (blue).

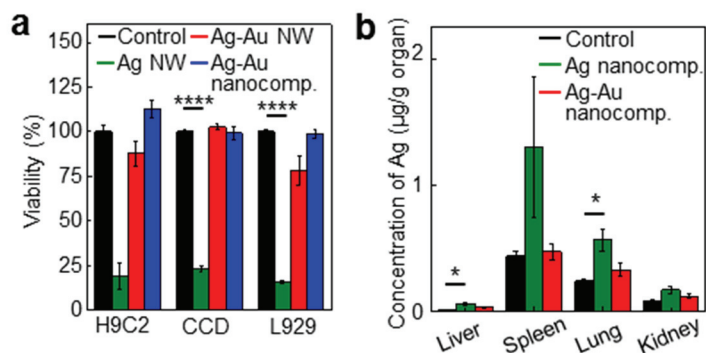


Figure 2.21. a) MTT assay shows H9C2, CCD-986sk, and L929 cells exposed to DMEM extracts of Ag NWs have significantly decreased viability compared to those exposed to original DMEM (control) or extracts of Ag-Au NWs and Ag-Au nanocomposite. Data are analyzed using one-way ANOVA and are expressed as averages \pm s.e.m. ($n = 3$). Significance is set at **** $P < 0.0001$ versus the control. b) ICP-MS analysis of Ag ions accumulated in liver, spleen, lung, and kidney after sham surgery (control) or implantation of the Ag nanocomposite and the Ag-Au nanocomposite for 3 weeks. Au sheath effectively reduces Ag ion accumulation in all organs. Data are analyzed using one-way ANOVA and are expressed as averages \pm s.e.m. ($n = 3$). Significance is set at * $P < 0.05$ versus the control.

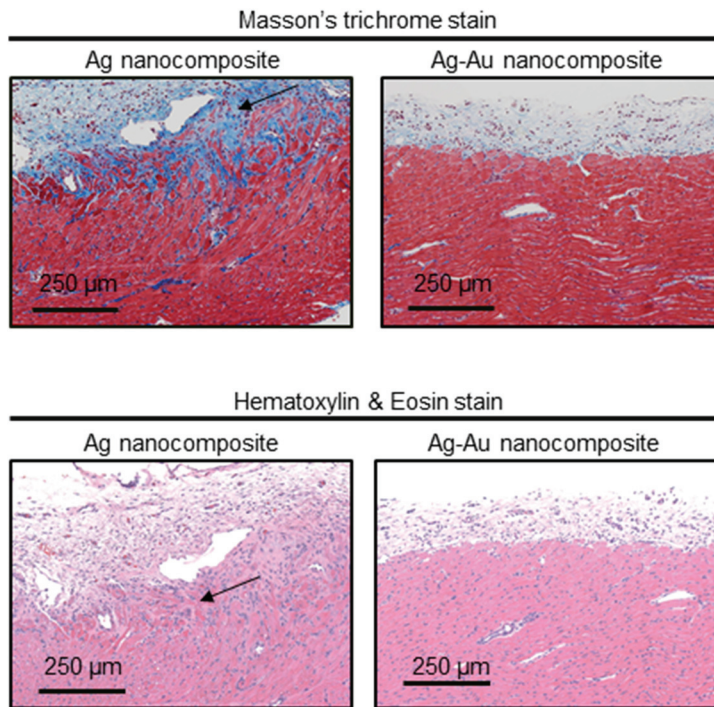


Figure 2.22. Masson's trichrome staining (top) and hematoxylin & eosin staining (bottom) of cardiac muscles after 3 weeks implantation of the Ag-Au nanocomposite shows less fibrotic reaction and inflammatory response than those implanted with Ag nanocomposite. Arrows in the first and the third panels indicate fibrosis and inflammatory cells, respectively.

2.3.4 Ag-Au nanocomposite for wearable bioelectronics

Due to its high stretchability and conductivity, we used the Ag-Au nanocomposite to develop wearable bioelectronics for measuring electrophysiological signals and applying electrical/thermal stimulations on the human skin. The Ag-Au nanocomposite and SBS are patterned by using polydimethylsilane (PDMS) molds and assembled into a multifunctional wearable electronic patch consisting of recording electrodes to measure electrophysiological signals, bipolar stimulation electrodes, and a heating element to apply electrical and thermal stimulations (Figure 2.23). Because the device is soft and stretchable (Figure 2.24a), it can follow the contour of flexible joints such as the wrist (Figure 2.24b). The electrodes, which are made of the Ag-Au nanocomposites, have low impedance (Figure 2.25a) and are therefore capable of obtaining electrocardiogram (ECG; from the right forearm with ankle ground) and electromyogram (EMG; from the right forearm) from the human skin with a high signal-to-noise ratio (Figure 2.25b).

While electrophysiological signals (*e.g.*, ECG, EMG) provide information on muscle and/or cardiac dysfunction, electrical stimulation is useful for pain relief³¹, rehabilitation³², and prosthetic motor control^{33,34}. Therefore, in addition to recording electrophysiological

signals, the wearable bioelectronics can be used to concurrently administer therapies through the skin. We applied constant-current monophasic square pulses to the skin through the wearable device using a computer-controlled stimulus generator (STG-4008, Multichannel system, Germany). Due to lower impedances, the stimulation electrodes made of the Ag-Au nanocomposite have lower threshold current than commercial electrodes, allowing stimulation with high power efficiency³⁵. The Ag-Au nanocomposite wearable device can simultaneously record EMG signals and deliver electrical stimulations (Figure 2.26). It is well-known that thermal stimulations in conjunction with electrical stimulations can bring synergetic effect in therapy^{14,32}. The stretchable heating element at the center of the wearable device is used for joule heating. Figure 2.27a shows the temperature-time profiles with various input voltages. Since the heater shows little resistance change under stretching, heating performance is stable under deformation (Figure 2.27b). The softness of the patch ensures firm contact with the skin, allowing reliable heat transfer even when the wrist is flexed or extended (Figure 2.28).

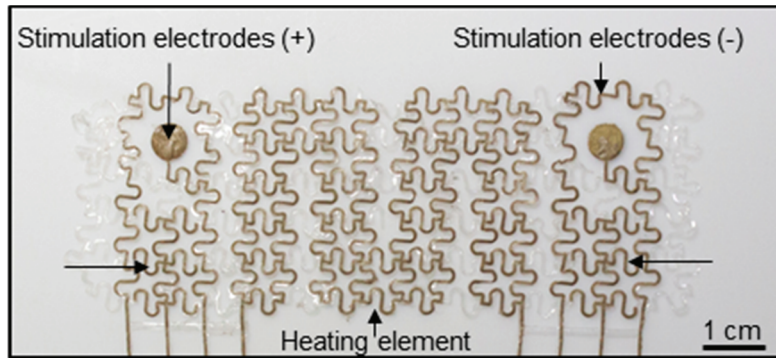


Figure 2.23. Optical camera image of a multifunctional wearable electronic patch consisting of bipolar stimulation electrodes, electrophysiological signal recording electrodes, and a heating element.

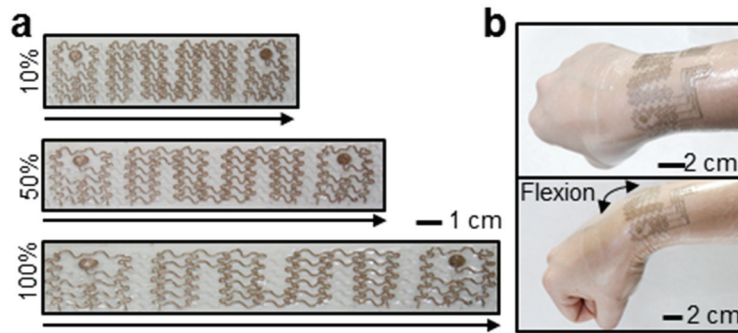


Figure 2.24. a-b), Optical camera images show the wearable device can be stretched 10%, 50%, and 100% (a), making them suitable for flexible joints such as the wrist (b).

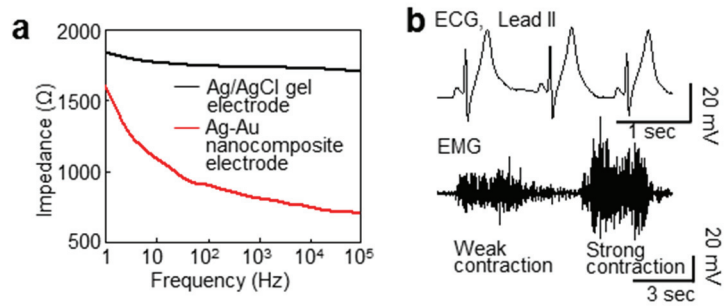


Figure 2.25. a) Impedance of the Ag-Au nanocomposite electrode at the skin/electrode interface is lower than Ag/AgCl gel electrodes. b) Electrocardiogram (ECG) and electromyogram (EMG) measurements obtained through the wearable device on the skin.

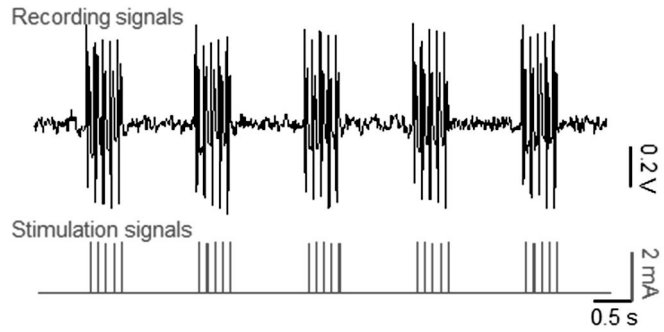


Figure 2.26. EMG signals measured during electrical stimulation. Temperature profiles of the heating element in the wearable device with applied voltages of 1, 2, and 3 V show reliable heating performance.

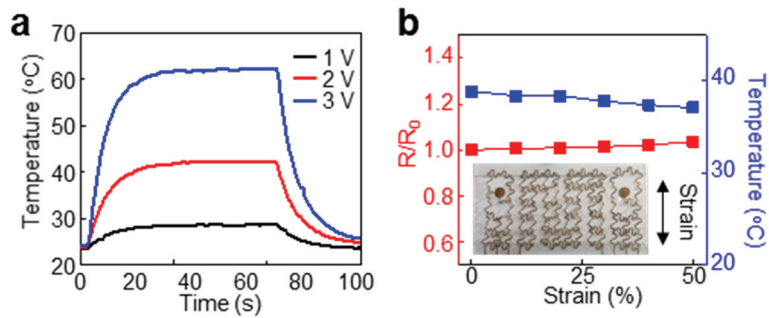


Figure 2.27. a) Temperature profiles of the heating element in the wearable device with applied voltages of 1, 2, and 3 V show reliable heating performance. b) Resistance (left axis) and temperature (right axis) change of the heating element under applied strain in longitudinal direction. Inset shows an optical camera image of multifunctional wearable electronic patch stretched in longitudinal direction.

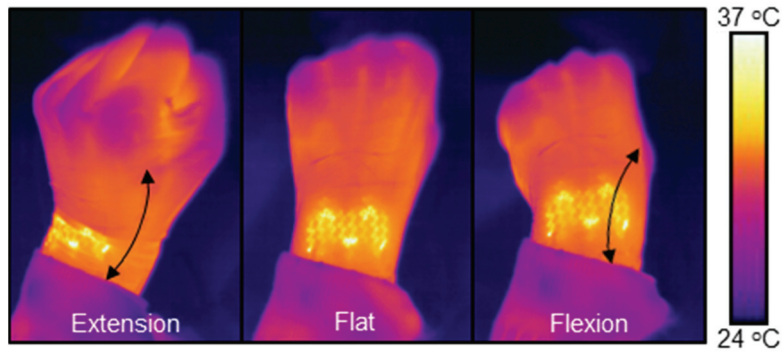


Figure 2.28. Infrared (IR) camera images show reliable heating performance of the wearable device on a wrist.

2.3.5 Implantable cardiac bioelectronics using Ag-Au nanocomposite

The Ag-Au nanocomposite is highly conductive, biocompatible, and soft, making them suitable as implantable devices. Various soft cardiac devices (*e.g.*, mesh¹¹, film³⁶, and sleeve³⁷, etc.) have been reported previously. However, the large area soft cardiac mesh for recording and stimulating at multiple locations of the swine heart has not been reported yet. Using the Ag-Au nanocomposite, we fabricated a customized large-area cardiac mesh, whose design is based on the detailed shape of the swine heart obtained using magnetic resonance imaging (Figure 2.29). The mesh is designed to cover the entire surface of the ventricles, and it contains multi-channel electrodes for recording and stimulation (Figure 2.30).

We simplified the shape of the cardiac silhouette into a conical frustum (Figure 2.30a top), which is subsequently unfolded to form a two-dimensional (2D) fan shape (Figure 2.30b). The cardiac mesh is designed based on this fan shape, which consists of 7 repetitive segments, each containing six pairs of electrodes. Each segment is made up of 5 layers: two electrode layers made of the Ag-Au nanocomposite and three insulation layers made of SBS (Figure 2.30a bottom). This

multi-layer format enables the multi-channel electrodes to cover from apex to base of the ventricles. The 7 segments are welded each other to form a 2D fan-shaped cardiac mesh.

The stretchability of the nanocomposite allows the mesh to fit the curvilinear-shaped heart. We show that resistance change under mechanical strain is negligible, and the 30% cyclic stretching (considering maximum heart movement¹¹) does not change the performance of the cardiac mesh, indicating the implanted mesh is stable during repetitive heart movements. Furthermore, because the modulus of each segment of the cardiac mesh is much lower than porcine myocardium³⁸, the mesh does not interfere with the heart's pumping activity^{11,37}.

We implanted the cardiac mesh on the porcine heart to record myocardial electrophysiology and stimulate the ventricles *in vivo* (Figure 2.31). Figure 2.32a shows intracardiac electrograms recorded by the multi-channel cardiac mesh that wraps around the ventricles in a healthy swine model. The left anterior descending coronary artery (LAD) was occluded with a balloon catheter to induce acute ischemia mimicking a heart attack in the clinical setting. On the voltage map constructed from the multi-channel mesh recording data, high voltage change in local

intracardiac electrograms was observed during ischemia at the anterior wall of the mid-apex left ventricle (Figure 2.32b). The surface electrocardiogram and intracardiac electrogram were continuously recorded by limb-leads and the cardiac mesh, respectively. Reliable recording was performed at baseline and during myocardial ischemia, which exhibited clearly differentiated patterns (Figure 2.33). In Figure 2.34, continuous electrical stimulation (*i.e.*, pacing) at different sites produced different QRS configurations in surface ECG with the pacing output of $< 1\text{ mA}$ at 2 ms, suggesting adequate compartmentalization of individual electrodes in the cardiac mesh without current leakage or uneven current flow.

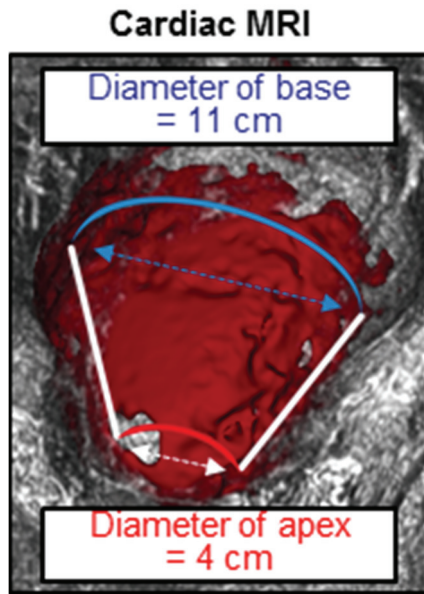


Figure 2.29. 3D cardiac MRI image of a swine heart (red).

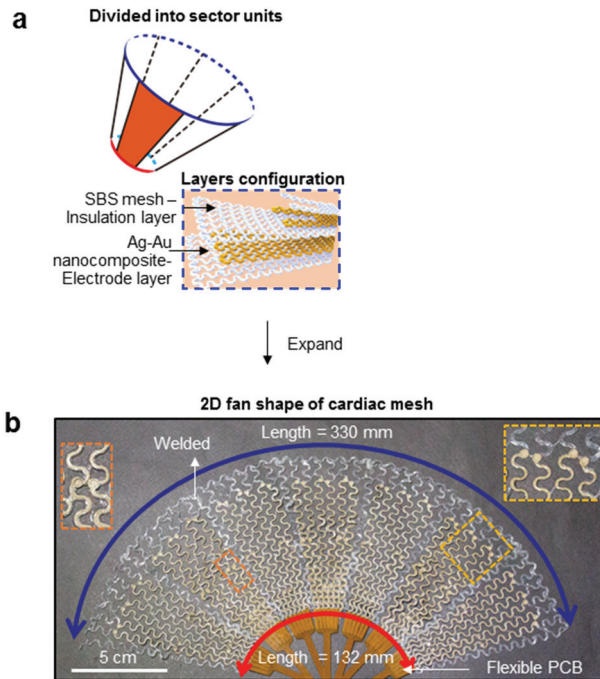


Figure 2.30. a-b) Schematic illustrating the design process for the cardiac mesh. The shape of the heart is simplified as a cone frustum (a), which is unfolded into a two-dimensional fan shape (b) consisting of 7 repetitive segments welded together. Lower inset in (a) shows the cardiac mesh consists of 2 electrode layers (Ag-Au nanocomposite) and three insulation layers (SBS)

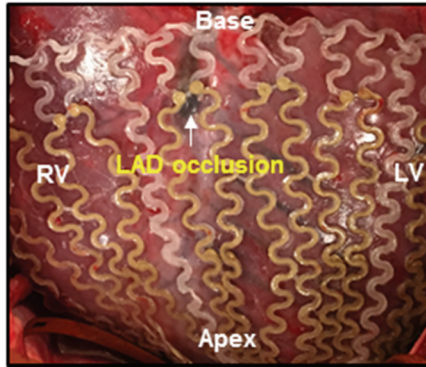


Figure 2.31. Optical camera image of implanted cardiac mesh on a swine heart

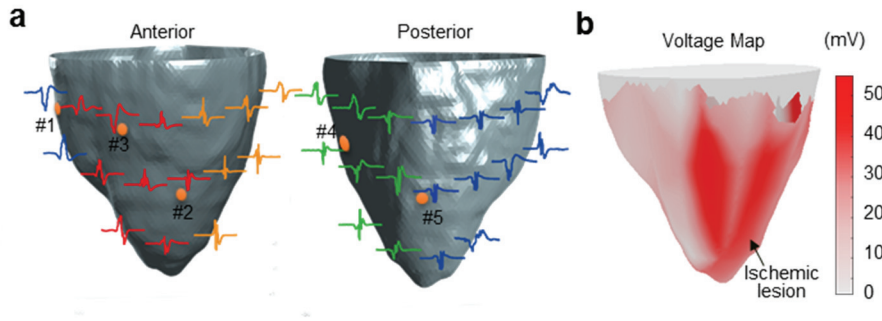


Figure 2.32. a) Representative intracardiac electrograms in a healthy swine model ($n = 2$) recorded by the cardiac mesh, displayed on a 3D reconstructed image of the heart (Red = LV anterior, Orange = LV lateral, Green = LV posterior, and Blue = RV, signals were recorded from 34 electrodes while the other electrodes were connected to the stimulator). b) Voltage map is constructed from local intracardiac electrograms recorded by the cardiac mesh during acute ischemia and the anterior wall of the left ventricle shows high voltage change. Acute ischemia is induced by occluding the left anterior descending coronary artery (LAD) using a balloon catheter.

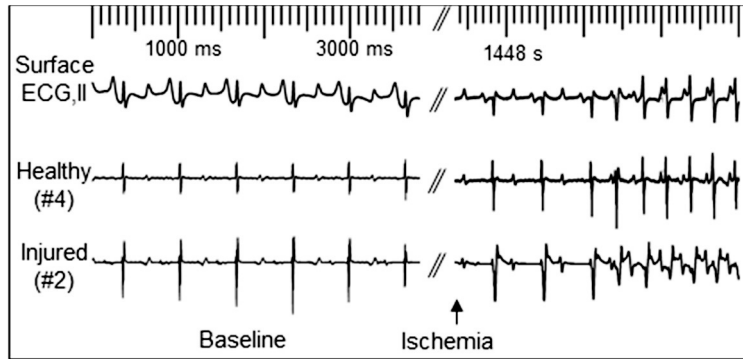


Figure 2.33. Surface ECG and intracardiac electrograms recorded from healthy and injured regions of the ischemic heart. Arrow indicates ST elevation due to ischemic change. Following prolonged myocardial ischemia of one hour, ventricular tachycardia occurred.

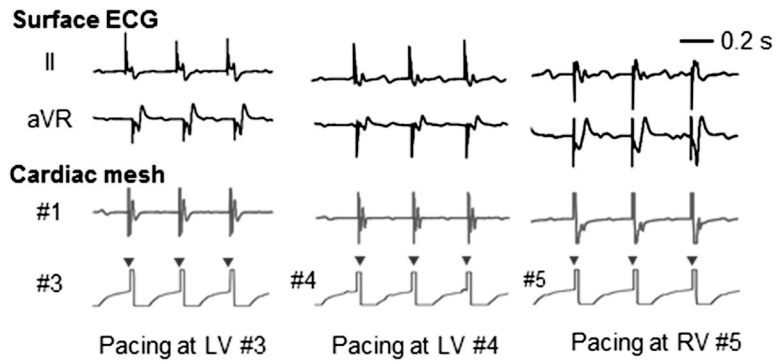


Figure 2.34. Representative surface ECG presents different QRS configurations depending on the pacing sites ($n = 1$). Electrode positions are numbered in Figure 2.32.

2.4 Conclusion

In conclusion, we report a new class of highly conductive, biocompatible, and soft nanocomposite using ultralong Ag-Au NWs and SBS elastomer. Epitaxial deposition of the Au sheath on ultralong Ag NWs without the galvanic replacement reaction effectively improves biocompatibility by preventing silver ion leaching and silver oxidation. High conductivity is attained using ultralong nanowires that formed a high density percolated network in the composite. The ambient solvent drying process during composite formation along with an optimized content of hexylamine promotes phase separation and formation of a cushy microstructure, generating the soft and highly stretchable nanocomposite. The additional heat rolling-press treatment increases stretchability of the Ag-Au nanocomposite by increasing toughness. When fabricated into a wearable skin-like device and implantable cardiac mesh, the highly conductive Ag-Au nanocomposite follows the contours of a curvilinear human wrist and a pulsating porcine heart, allowing electrophysiological signals including surface EMG, surface ECG, and intracardiac electrogram to be monitored, and thermal and electrical stimulations to be administered effectively. These advanced nanocomposite technologies are poised to create new possibilities for

next-generation soft bioelectronics.

Most of the contents of this chapter were published in the article, “Highly conductive, stretchable, and biocompatible nanocomposite using ultralong Ag-Au core-sheath nanowires for wearable and implantable bioelectronics.” (*Nature Nanotechnology* **2018, *13*, 1048)

2.5 References

- [1] Y. Kim, J. Zhu, B. Yeom, M. Di Prima, X. Su, J. G. Kim, S. J. Yoo, C. Uher, N. A. Kotov, *Nature* 2013, 500, 59.
- [2] M. Park, J. Im, M. Shin, Y. Min, J. Park, H. Cho, S. Park, M. B. Shim, S. Jeon, D. Y. Chung, J. Bae, J. Park, U. Jeong, K. Kim, *Nat Nanotechnol* 2012, 7, 803.
- [3] N. Matsuhisa, D. Inoue, P. Zalar, H. Jin, Y. Matsuba, A. Itoh, T. Yokota, D. Hashizume, T. Someya, *Nat Mater* 2017, 16, 834.
- [4] D. H. Kim, N. Lu, R. Ma, Y. S. Kim, R. H. Kim, S. Wang, J. Wu, S. M. Won, H. Tao, A. Islam, K. J. Yu, T. I. Kim, R. Chowdhury, M. Ying, L. Xu, M. Li, H. J. Chung, H. Keum, M. McCormick, P. Liu, Y. W. Zhang, F. G. Omenetto, Y. Huang, T. Coleman, J. A. Rogers, *Science* 2011, 333, 838.
- [5] D. Son, J. Lee, S. Qiao, R. Ghaffari, J. Kim, J. E. Lee, C. Song, S. J. Kim, D. J. Lee, S. W. Jun, S. Yang, M. Park, J. Shin, K. Do, M. Lee, K. Kang, C. S. Hwang, N. Lu, T. Hyeon, D. H. Kim, *Nat Nanotechnol* 2014, 9, 397.
- [6] M. K. Choi, J. Yang, K. Kang, D. C. Kim, C. Choi, C. Park, S. J. Kim, S. I. Chae, T. H. Kim, J. H. Kim, T. Hyeon, D. H. Kim,

- Nature Communications 2015, 6, 7149.
- [7] D. J. Lipomi, M. Vosgueritchian, B. C. Tee, S. L. Hellstrom, J. A. Lee, C. H. Fox, Z. Bao, *Nat Nanotechnol* 2011, 6, 788.
- [8] A. Miyamoto, S. Lee, N. F. Cooray, S. Lee, M. Mori, N. Matsuhisa, H. Jin, L. Yoda, T. Yokota, A. Itoh, M. Sekino, H. Kawasaki, T. Ebihara, M. Amagai, T. Someya, *Nature Nanotechnology* 2017, 12, 907.
- [9] I. You, B. Kim, J. Park, K. Koh, S. Shin, S. Jung, U. Jeong, *Adv Mater* 2016, 28, 6359.
- [10] S. Gong, D. T. H. Lai, B. Su, K. J. Si, Z. Ma, L. W. Yap, P. Guo, W. Cheng, *Advanced Electronic Materials* 2015, 1, 1400063.
- [11] J. Park, S. Choi, A. H. Janardhan, S. Y. Lee, S. Raut, J. Soares, K. Shin, S. Yang, C. Lee, K. W. Kang, H. R. Cho, S. J. Kim, P. Seo, W. Hyun, S. Jung, H. J. Lee, N. Lee, S. H. Choi, M. Sacks, N. Lu, M. E. Josephson, T. Hyeon, D. H. Kim, H. J. Hwang, *Science Translational Medicine* 2016, 8, 344ra86.
- [12] C. Lu, S. Park, T. J. Richner, A. Derry, I. Brown, C. Hou, S. Rao, J. Kang, C. T. Mortiz, Y. Fink, P. Anikeeva, *Sci Adv* 2017, 3, e1600955.
- [13] P. Lee, J. Lee, H. Lee, J. Yeo, S. Hong, K. H. Nam, D. Lee, S. S.

- Lee, S. H. Ko, *Adv Mater* 2012, 24, 3326.
- [14] S. Choi, J. Park, W. Hyun, J. Kim, J. Kim, Y. B. Lee, C. Song, H. J. Hwang, J. H. Kim, T. Hyeon, D. H. Kim, *ACS Nano* 2015, 9, 6626.
- [15] D. McShan, P. C. Ray, H. Yu, *J Food Drug Anal* 2014, 22, 116.
- [16] M. Yang, Z. D. Hood, X. Yang, M. Chi, Y. Xia, *Chemical Communications* 2017, 53, 1965.
- [17] R. S. Jianfen J. Cai, *JOURNAL OF MATERIALS SCIENCE* 1999, 34, 4719.
- [18] R. Ma, B. Kang, S. Cho, M. Choi, S. Baik, *ACS Nano* 2015, 9, 10876.
- [19] Y. Wang, C. Zhu, R. Pfattner, H. Yan, L. Jin, S. Chen, F. Molina-Lopez, F. Lissel, J. Liu, N. I. Rabiah, Z. Chen, J. W. Chung, C. Linder, M. F. Toney, B. Murmann, Z. Bao, *Sci Adv* 2017, 3, e1602076.
- [20] N. Matsuhisa, M. Kaltenbrunner, T. Yokota, H. Jinno, K. Kuribara, T. Sekitani, T. Someya, *Nature Communications* 2015, 6, 7461.
- [21] L. Jose Andres, M. Fe Menendez, D. Gomez, A. Luisa Martinez, N. Bristow, J. Paul Kettle, A. Menendez, B. Ruiz,

- Nanotechnology 2015, 26, 265201.
- [22] Y. Sun, Y. Yin, B. T. Mayers, T. Herricks, Y. Xia, *Chemistry of Materials* 2002, 14, 4736.
- [23] H. Liu, T. Liu, L. Zhang, L. Han, C. Gao, Y. Yin, *Advanced Functional Materials* 2015, 25, 5435.
- [24] Y. Yang, J. Liu, Z. W. Fu, D. Qin, *J Am Chem Soc* 2014, 136, 8153.
- [25] A. Dong, X. Ye, J. Chen, Y. Kang, T. Gordon, J. M. Kikkawa, C. B. Murray, *J Am Chem Soc* 2011, 133, 998.
- [26] I. R. Mineev, P. Musienko, A. Hirsch, Q. Barraud, N. Wenger, E. M. Moraud, J. Gandar, M. Capogrosso, T. Milekovic, L. Asboth, R. F. Torres, N. Vachicouras, Q. Liu, N. Pavlova, S. Duis, A. Larmagnac, J. Voros, S. Micera, Z. Suo, G. Courtine, S. P. Lacour, *Science* 2015, 347, 159.
- [27] S. Lin, H. Yuk, T. Zhang, G. A. Parada, H. Koo, C. Yu, X. Zhao, *Adv Mater* 2016, 28, 4497.
- [28] H. Lee, T. K. Choi, Y. B. Lee, H. R. Cho, R. Ghaffari, L. Wang, H. J. Choi, T. D. Chung, N. Lu, T. Hyeon, S. H. Choi, D. H. Kim, *Nat Nanotechnol* 2016, 11, 566.
- [29] H. Lee, Y. J. Hong, S. Baik, T. Hyeon, D. H. Kim, *Adv. Healthc.*

Mater. 2018.

- [30] J. Y. Sun, X. Zhao, W. R. Illeperuma, O. Chaudhuri, K. H. Oh, D. J. Mooney, J. J. Vlassak, Z. Suo, *Nature* 2012, 489, 133.
- [31] M. V. Hurley, L. M. Bearne, *Best Pract Res Clin Rheumatol* 2008, 22, 419.
- [32] P. Sarzi-Puttini, M. A. Cimmino, R. Scarpa, R. Caporali, F. Parazzini, A. Zaninelli, F. Atzeni, B. Canesi, *Semin Arthritis Rheum* 2005, 35, 1.
- [33] B. Xu, A. Akhtar, Y. Liu, H. Chen, W. H. Yeo, S. I. Park, B. Boyce, H. Kim, J. Yu, H. Y. Lai, S. Jung, Y. Zhou, J. Kim, S. Cho, Y. Huang, T. Bretl, J. A. Rogers, *Adv Mater* 2016, 28, 4462.
- [34] S. Lim, D. Son, J. Kim, Y. B. Lee, J.-K. Song, S. Choi, D. J. Lee, J. H. Kim, M. Lee, T. Hyeon, D.-H. Kim, *Advanced Functional Materials* 2015, 25, 375.
- [35] T. A. Kuiken, P. D. Marasco, B. A. Lock, R. N. Harden, J. P. Dewald, *Proc Natl Acad Sci U S A* 2007, 104, 20061.
- [36] S. Lee, Y. Inoue, D. Kim, A. Reuveny, K. Kuribara, T. Yokota, J. Reeder, M. Sekino, T. Sekitani, Y. Abe, T. Someya, *Nat Commun* 2014, 5, 5898.
- [37] L. Xu, S. R. Gutbrod, A. P. Bonifas, Y. Su, M. S. Sulkin, N. Lu,

H. J. Chung, K. I. Jang, Z. Liu, M. Ying, C. Lu, R. C. Webb, J. S. Kim, J. I. Laughner, H. Cheng, Y. Liu, A. Ameen, J. W. Jeong, G. T. Kim, Y. Huang, I. R. Efimov, J. A. Rogers, *Nature Communications* 2014, 5, 3329.

[38] T. Pham, W. Sun, *J. Mech. Behav. Biomed. Mater.* 2012, 6, 21.

[39] F. M. Smits, *Bell System Technical Journal* 1958, 37, 711.

Chapter 3. Heterostructured Ceria-Manganese Oxide nanocrystals as an Antioxidant for mitigation of Acute Radiation Syndrome

3.1 Introduction

Growing utilization of radioactive irradiation in medical and industrial fields has raised the risk of accidental total body irradiation (TBI) that causes life-threatening consequences such as acute radiation syndrome (ARS).^[1] Clinical manifestations of ARS are categorized into hematopoietic (H-ARS, 1.5-4Gy),^[2] gastrointestinal (GI-ARS, 6-15Gy),^[3] and neurovascular syndromes (NV-ARS, 15Gy).^[4] Microscopically when tissues are exposed to irradiation (IR), ROS is rapidly generated within a millisecond via radiolysis of water.^[5] These ROS reacts with nucleic acids and cellular components, leading to the disruption of biological functions and even cellular apoptosis.^[6] Although many ROS scavenging and regenerative medicines have been

developed as radio-protectants only one of them has been approved by FDA; Amifostine (Ethyol).^[7] However, due to its short half-life and limiting capability to scavenging ROS, the radio-protectant with long-lasting and stable activity and low active dose with highest performance is highly desired to protect body from the irradiation. In recent years, catalytic nanomaterials with antioxidant property gained much attention due to their therapeutic potential to treat ROS-related diseases.^[8] Nanomaterials of ceria,^[9-11] manganese oxide,^[12, 13] iron oxide,^[14] vanadium oxide,^[15] platinum^[16] are reported to exhibit superoxide dismutase (SOD)- and catalase-mimetic enzymatic activity, which are highly responsible for removing ROS. Especially, ceria nanoparticles are spotlighted as the antioxidant for treating various diseases due to their redox cycles between Ce^{3+} and Ce^{4+} that allow ceria to catalytically remove ROS such as superoxide (O_2^-), hydrogen peroxide (H_2O_2), and $\cdot OH$.^[17] However, increasing concerns on the potential intrinsic toxicity of inorganic nanomaterials remain challenge. The ultimate goal is to lower the therapeutic concentration by maximizing catalytic reactivity so that we can achieve maximum therapeutic efficacy with minimal dose. Recent studies focus on catalysts consist of two metals which can greatly enhance catalytic performance through ensemble, ligand or strain

effect.^[18-20] Especially, tuning the oxygen adsorption energy by modifying surface strains of metallic core/shell nanomaterial is generally known as an effective approach to boost surface catalytic activity. However, these studies are limited to systems of metal pairs with mild lattice mismatch.^[21] Herein, we demonstrate the effect of strain in oxide nanocrystals on antioxidant catalytic activity by using heterostructured CeO₂/Mn₃O₄ nanocrystals with highly strained Mn₃O₄ surface. Manganese ions deposited on the surface of ceria nanocrystals increase O-vacancies in ceria and the strained layers of Mn₃O₄ islands grown on ceria facilitate redox property of Mn₃O₄ surface. These synergistic effects boost antioxidant catalytic activity of CeO₂/Mn₃O₄. The CeO₂/Mn₃O₄ are able to be delivered systemically to protect tissues from TBI with significantly lower dose and high efficacy.

3.2 Experimental Section

3.2.1 Synthesis of CeO₂ nanocrystals

A mixture of 0.23 g of cerium (III) nitrate (Acros), 3.5 g of oleylamine (Acros), and 0.01 g of oleic acid (Aldrich) in 30 mL of 1-dodecanol (Aldrich) was heated to 110 °C under air. The solution was aged for several minutes until it changed to yellow. During heating process, 0.03 mL of distilled water was added around 90 °C. After the reaction, an excess amount of acetone, ethanol, and acetonitrile was added to purify the ceria nanocrystals. The nanocrystals were collected by centrifugation.

3.2.2 Synthesis of CeO₂/Mn₃O₄ nanocrystals

A mixture of as-synthesized CeO₂ nanocrystals (0.03 g), 0.8 g of oleylamine (Acros), 0.12 g of oleic acid (Aldrich), 0.26 mL of hydrochloric acid (Aldrich), and 15 mL of xylenes (Aldrich) were heated to 90 °C. Then, aqueous solution of 0.8 mL of 0.18 M manganese (II) chloride was rapidly injected into the heated solution. After 2 h aging of the solution, the CeO₂/Mn₃O₄ nanocrystals were washed with hexane

and ethanol, and retrieved by centrifugation. As-prepared heterostructured $\text{CeO}_2/\text{Mn}_3\text{O}_4$ nanocrystals are well dispersed in chloroform.

3.2.3 Structural and chemical analysis

The transmission electron microscopy (TEM) and the energy-filtered TEM images were obtained using JEOL JEM-2100F. High-angle annular dark-field scanning TEM (HAADF-STEM) images were obtained using JEOL JEM-ARM200F in National Center for Inter-university Research Facilities, Seoul National University. X-ray diffraction (XRD) patterns were obtained using a Rigaku D/max 2500 diffractometer with $\text{Cu K}\alpha$ radiation in Seoul National University. Experiments at PLS-II were supported in part by MSIP and POSTECH. Raman spectra and X-ray photoelectron spectroscopy were obtained using HORIBA LabRAM HV Evolution and KRATOS AXIS-HSi, respectively, in Research Institute of Advanced Materials, Seoul National University.

3.2.4 Electrochemical measurements

Before conducting electrochemical measurement, ligands on the nanocrystal surface were exchanged using nitrosonium tetrafluoroborate (NOBF₄). The solution of 0.01 g of NOBF₄ and 0.4 mL of dimethylformamide (DMF) was prepared in Ar atmosphere. The solution was added into the 10 mL THF solution containing as-prepared nanoparticles. And then, the nanoparticles were collected by adding hexane. Electrochemical reduction of hydrogen peroxide and oxygen was measured at 293 K in a three-electrode system with Autolab 302 potentiostat. For working electrode, nanocrystals dispersed in solution were drop-casted on glassy carbon (diameter of 3 mm) with the loading of 0.2 mg/cm². Graphite rod and saturated calomel electrode (SCE) were used as a counter and a reference electrode, respectively. For electrochemical reduction reaction, nanocrystals were polarized between 0.0 V and -0.8 V (vs. SCE) at scan rate of 50 mV/s in Ar-saturated 5.00 mM H₂O₂ PBS solution (pH 7.4) and O₂-saturated PBS solution (pH 7.4).

Synthesis of phospholipid-polyethylene glycol-capped CeO₂/Mn₃O₄ nanocrystals

Phospholipid-polyethylene glycol (PEG) were encapsulated on surface of CeO₂/Mn₃O₄ nanocrystals to synthesize water dispersible CeO₂/Mn₃O₄ nanocrystals. First, 3 ml of the CeO₂/Mn₃O₄ nanocrystals in chloroform (10 mg/ml) was mixed with 10 ml of 1,2-distearoyl-*sn*-glycero-3-phosphoethanolamine-N-[methoxy(polyethylene glycol)-2000] (mPEG(2000)-PE, Avanti Polar Lipids Inc., Alabaster, Alabama, USA) in chloroform (10 mg/ml) and sonicated for 5 min. Chloroform was then removed by a rotary evaporator, and further dried completely in vacuum oven at 70 °C for 2 hrs. Next, 3 ml of deionized water was added to the sample and sonicated to obtain a transparent colloidal suspension. The excess mPEG(2000)-PE was removed using ultracentrifugation and the CeO₂/Mn₃O₄ nanocrystals were filtered using 0.4 μm filter. Finally, the CeO₂/Mn₃O₄ nanocrystals were dispersed in PBS solution for the further applications.

Cell viability test

HeLa are seeded in the 96-well plate with 10,000 cells per well and

cultured for 24 hrs. Subsequently, CeO₂/Mn₃O₄ nanocrystals were treated with various concentrations and incubated for another 24 hrs. 20 µl (5 mg/ml) 3-[4,5-dimethylthiazol-2-yl]-2,5-diphenyltetrazolium bromide (MTT) was added to each well and incubated at 37 °C for 4 hrs. Finally, the medium is removed and 200 µl dimethylsulfoxide is added to each well. The absorbance was measured at 540 nm using a 96-well plate reader (Victor X4, Perkin-Elmer, USA).

Immunofluorescence staining and imaging procedures for human intestinal organoids (hIO)

hIOs in Matrigel dome were fixed with ice-cold 4% paraformaldehyde for 30 min. After removing paraformaldehyde, hIOs were washed with PBS for three times (5 min per wash). 0.2% Triton X-100 PBS (PBST) was added and incubated for 5 min. After the removal of PBST, hIOs were washed twice with PBS (5 min per wash). And then, hIOs were blocked by PBS containing 5% normal donkey serum (NDS, Sigma-Aldrich, D9663) for 2 hrs at room temperature. hIOs were then incubated overnight with primary antibodies (1:100) diluted in PBS containing 1% NDS at 4 °C. The primary antibodies were washed three times with PBS

(5 min per wash), and treated with secondary antibodies (1:250) and DAPI (1:1000) diluted in PBS containing 1% NDS. After 2 hr incubation, hIOs were washed three times with PBS (5 min per wash). Stained hIOs were mounted with Fluoro-Gel (17985-10, Electron Microscopy Science) and then stored at 4 °C. Immunofluorescence staining images were obtained on a confocal laser scanning microscope (Carl Zeiss, LSM700) equipped with 20X and 40X plan-apochromat lens (Carl Zeiss), and 405, 488, 555, and 647nm excitation lasers were used. More than four Z-sections were obtained and the sections were merged via maximum intensity projection using a Zen Blue software (Carl Zeiss).

mRNA isolation from hIOs

Entire Matrigel dome containing hIOs was dissolved by Trizol solution (ThermoFisher Scientific, 15596018). mRNAs in Trizol were extracted by Direct-zol RNA Miniprep Plus (Zymo Research, R2070S) and stored at -80 °C for mRNA sequencing.

Organoid formation assay

8-week ICR mice were intraperitoneally injected with PBS or CeO₂/Mn₃O₄ nanocrystal (0.55mg/kg body weight) 2 hrs before the total body irradiation. Within 30 min after 13 Gy TBI, mice were sacrificed, and small intestines were isolated and washed by flushing PBS to the lumen. The small intestines were longitudinally cut, and villi were scrapped off by using a cover glass. After the villi removal, duodenum part was cut into several sections, and they were vigorously washed three times in PBS. Next, crypts were isolated from the duodenum sections by Gentle Cell Dissociation Reagent (GCDR, Stem cell Technologies, 07174) treatment for 15 min. After several vigorous shaking with GCDR, supernatant was filtered through 70 μ m cell strainer. The filtered supernatant was centrifuged and washed three times. And then, intestinal crypt pellet was mixed with liquid state Matrigel. 20 μ l of Matrigel drop containing 100 intestinal crypts was placed at the center of a 24 well plate and solidified for 15 min at 37 °C. And then, 700 μ l of pre-warmed InstiCult Organoid Growth Medium for Mouse (Stem cell Technologies, 06005) was slowly added to the well. Three days after the seeding, formation of intestinal organoid was observed by bright field microscope (Nikon Ti digital inverted fluorescence microscope). Number of

transparent cystic form intestinal organoids per visual field was manually counted.

Blood cytokine analysis

8-week ICR mice subjected to the experiment were anesthetized by Alfaxan and Rumpun (Bayer Korea, KR07050) mixture and 1 to 1.5 ml blood was drawn from ventricle of heart. Collected blood samples were immediately placed in BD vacutainer blood collection tubes (BD Biosciences, 367874) and centrifuged at 2000g at room temperature. And then, plasma layer was carefully drawn and placed in cryovial. The obtained plasma samples were stored at -80 °C for the further analysis.

Intracellular ROS and viability assay for bone marrow cells (BMCs)

8-week ICR mice subjected to the experiment were sacrificed and their femurs were collected. After removing all the soft tissues attached to the femurs, metaphysis was exposed by cutting off condyles and epiphysis. Prepared femurs were placed in a 5 ml pipet tip, nested in a DMEM media-containing 15 ml tube. Nested tip in tube was centrifuged at 8000g

for 30 sec to collect BMC pellets. For ROS assay, collected BMCs were incubated with 10 μ M CellRox Green (C10444, Thermofisher Scientific) reagent for 30 min and then washed 3 times with HBSS. Then ROS dye-loaded BMCs were analyzed using a FACS (BD bioscience). For viability assay, the number of freshly isolated viable BMCs per femur was counted by Cellometer Mini (Nexelom Bioscience).

MDA assay for plasma and internal organs

Internal organs and blood plasma were collected from 8-week ICR mice subjected to the experiment. For internal organs, they were bead-homogenized by a Superfast prep 2 (MP biomedical, SKU116012500) for 15 seconds in 1X RIPA Lysis buffer (EMD Millipore, 20-188). After that, sample tubes were centrifuged at 3500 rpm for 15 min at 4 °C. Supernatant was collected and protein concentration was measured by BCA assay. After the preparation, MDA assay for both plasma and internal organs was performed using an OxiSelect TBARS Assay Kit (CELL BIOLABS, STA-330), following the manufacturer's instruction.

mRNA-sequencing

In order to construct cDNA libraries with the TruSeq RNA library kit, 1 μ g of total RNA was used. The protocol consisted of polyA-selected RNA extraction, RNA fragmentation, random hexamer primed reverse transcription, and 100 nt paired-end sequencing by an Illumina HiSeq2500. The libraries were quantified using qPCR according to the qPCR quantification protocol guide and qualified using an Agilent Technologies 2100 Bioanalyzer.

We processed reads from the sequencer and aligned them to the *Mus musculus* (mm10) using Tophat v2.0.13(1). Tophat incorporates the Bowtie v2.2.3(2) algorithm to perform the alignment. Tophat initially removes a portion of the reads based on the quality information accompanying each read before it maps reads to the reference genome. The reference genome sequence of *Mus musculus* (mm10) and annotation data were downloaded from the UCSC table browser (<http://genome.uscs.edu>). Gene annotation information was also used for running Tophat with “-G” option. In the case of other parameters for Tophat, default options were used. Tophat allows multiple alignments per read (up to 20 by default) and the maximum of 2 mismatches when

mapping the reads to the reference. Transcript assembly and abundance estimation was performed using the Cufflinks (3). After aligning reads to genome Cufflinks v2.2.1 were used to assemble aligned reads into transcripts and to estimate their abundance. To correct sequence expression count bias, ‘--max-bundle-frags 50000000’ options were used. We also used the ‘-G’ option for making the best use of known gene annotation information. In case of other parameters, default options were used. The transcript counts in isoform level were calculated, and the relative transcript abundances were measured in FPKM (Fragments Per Kilobase of exon per Million fragments mapped) from Cufflinks. And gene level expression values were also calculated from the transcript counts. These values were used for DEG analysis later.

Statistical analysis of gene expression level

The transcript-level relative transcript abundances were measured in FPKM (Fragments Per Kilobase of exon per Million fragments mapped) using Cufflinks. Gene-level relative abundances were calculated as the sum of FPKMs of transcripts in the gene. We performed the statistical analysis to find differentially expressed genes. Genes with one more than

zeroed FPKM values in the samples were excluded. To facilitate log₂ transformation, 1 was added to each FPKM value of filtered genes. Filtered data were log₂-transformed and subjected to quantile normalization. Statistical significance of the differential expression data was determined using independent t-test and fold change in which the null hypothesis was that no difference exists among groups. False discovery rate (FDR) was controlled by adjusting p value using Benjamini-Hochberg algorithm. For DEG set, Hierarchical clustering analysis was performed using complete linkage and Euclidean distance as a measure of similarity. Gene-enrichment and functional annotation analysis for significant gene list was performed using Gene Ontology (www.geneontology.org/) and pathway analysis for the DEG was done based on KEGG pathway (<http://www.genome.jp/kegg/pathway.html>).

Volume Plot

Expression volume is defined as the geometric mean of two groups' expression levels. In order to confirm the genes that show higher expression difference compared to the control according to expression volume, volume plots were drawn (x-axis: volume, y-axis: log₂ fold

change). For example, even though the fold change might be different by two-fold, the gene with higher volume may be more credible.

Multidimensional scaling

We used multidimensional scaling (MDS) method to visualize the similarities among samples. MDS is one of the methods that converts the structure in a similarity matrix to a simple geometrical picture as scatter plots. The larger the dissimilarity between 2 samples, the further apart the points representing the experiments in the picture should be. We applied the Euclidean distance as the measure of the dissimilarity.

Hierarchical clustering

Hierarchical clustering analysis was performed using complete linkage and Euclidean distance as a measure of similarity to display the expression patterns of differentially expressed transcripts which are satisfied with $|\text{fold change}| \geq 2$ and independent t-test raw $p < 0.05$. All data analysis and visualization of differentially expressed genes was conducted using R v3.1.2 (www.r-project.org).

3.3 Result and Discussion

3.3.1 Synthesis and characterization of CeO₂/Mn₃O₄

Heterostructured CeO₂/Mn₃O₄ were prepared by the seed-mediated growth process. To use CeO₂ as seeds, 4 nm-sized truncated octahedral CeO₂ nanocrystals dominantly enclosed by {100} and {111} planes were first synthesized in 1-dodecanol solution (Figure 3.1a). As-prepared CeO₂ nanocrystals were then reacted with Mn(NO₃)₂ to produce heterostructured ceria/manganese oxide nanocrystals (Figure 3.1b). High-angle annular dark-field scanning transmission electron microscopy (HAADF-STEM) images in Figure 3.1b show that the morphology of ceria nanocrystals is well preserved after the heterogeneous precipitation of manganese oxide. The crystal phases of CeO₂ and heterostructured CeO₂/Mn₃O₄ were characterized by using X-ray diffraction (XRD). The CeO₂ nanocrystals have fluorite-structure with an estimated (111) plane lattice spacing of 3.14 Å (Figure 3.2). The fast Fourier transform (FFT) of the STEM image and XRD pattern of CeO₂/Mn₃O₄ were nearly the same as those of CeO₂ nanocrystals, demonstrating that manganese oxide is epitaxially grown on the ceria nanocrystals without a separation homogeneous precipitation process

(Figure 3.1b). When less than 15 mol% of Mn is deposited on the CeO₂ nanocrystals, the oxidation state of Mn was mostly Mn²⁺, generating Ce⁴⁺-O-Mn²⁺ polar interface (Figure 3.3). However, when 30 mol% of Mn is deposited, both Mn²⁺ and Mn³⁺ were observed. Combining the XPS, XAS data, known lattice parameters and atomic arrangements of Mn₃O₄ (JCPDS #80-0382), our heterostructured CeO₂/Mn₃O₄ are composed of CeO₂, Ce⁴⁺-O-Mn²⁺ at the heterointerface, and 3 atomic layers of Mn₃O₄. X-ray photoelectron spectroscopy (XPS) and X-ray absorption spectra (XAS) data show that the Ce³⁺ ions are well preserved after the deposition of island-like Mn₃O₄ shell (Figure 3.4). The result was further supported by the visible Raman spectra (532 nm) of CeO₂/Mn₃O₄ that show both first-order F_{2g} symmetry mode of CeO₂ at 452 cm⁻¹ and A_{1g} symmetric stretching Mn-O bond peak of Mn₃O₄ at 645 cm⁻¹ (Figure 3.5). Asymmetric peak broadening of F_{2g} peak indicates defects, structural distortions induced by heteroepitaxial strain. The broadened A_{1g} peak is originated from the epitaxial strain in Mn₃O₄ shell induced by lattice mismatch. The Mn₃O₄ shell grows in the [112] direction parallel to the CeO₂ (111) plane because the lattice mismatch between the CeO₂ (111) plane and Mn₃O₄ (112) plane is the smallest, ~1.2%. The mismatches along the CeO₂ {200} and {220} are 6.3% and

4.2%, and thus the shell is biaxially strained (Figure 3.1b). The UV Raman spectra (325 nm) were used to compare the surface defects between CeO₂ nanocrystals and CeO₂/Mn₃O₄ (Figure 3.6). The intensity ratio of defect-induced (D mode) peak at 598 cm⁻¹ and F_{2g} peak (I_D/I_{F2g}) was increased after the Mn₃O₄ deposition, showing the increased O-vacancies on the CeO₂ surface. The CeO₂/Mn₃O₄ with abundant O-vacancies were expected to exhibit high activity for ROS scavenging. Defective oxide surfaces can also be detected by O 1s XPS spectra (Figure 3.7). Binding energies of ~529.2 eV, ~531.5 eV, and 533.2 eV could be assigned to lattice oxygen (O_{latt}), surface adsorbed oxygen (O_{ads}), and chemisorbed species such as water (O_{surf}), respectively. Since the range of 531~532 eV represents the defective sites having electrophilic O₂²⁻, O₂⁻, and O⁻ on the surface, the oxygen defect concentration can be estimated from O_{ads}/O_{latt} ratios. The higher ratio of CeO₂/Mn₃O₄ (2.16) than that of CeO₂ (1.04) reveals the higher oxygen vacancy level in CeO₂/Mn₃O₄, in good agreement with the Raman results. To study the surface reducibility, we measured H₂ temperature-programmed reduction (TPR) (Figure 3.8). Both surface oxygen reduction peak at 507 °C for CeO₂ and the peak of Mn₃O₄ reduction to Mn²⁺ at 498 °C were shifted to a lower temperature (382 °C), indicating

the enhancement of surface reducibility for CeO₂/Mn₃O₄. By combining TEM, XPS, XAS, Raman, and H₂-TPR results, we can conclude that a few strained layers of Mn₃O₄ produced by the heteroepitaxy process are necessary to generate the high redox-active surface of CeO₂/Mn₃O₄. The ability of eliminating ROS is compared by measuring catalytic activities of CeO₂, CeO₂/Mn₃O₄, and Mn₃O₄ toward the reduction of H₂O₂ and oxygen. Figure 3.9a and Figure 3.9b show cyclic voltammetric (CV) scans of three samples supported on glassy carbon electrodes (GCE) in Ar-saturated phosphate-buffered saline (PBS, 0.01 M) in the presence of 5.00 mM H₂O₂ and in O₂-saturated PBS, respectively. The sharp increase of reduction current under -0.4 V compared to monometallic CeO₂ and Mn₃O₄ was observed in CeO₂/Mn₃O₄ curve showing improved catalytic activities. As-synthesized CeO₂/Mn₃O₄ are transferred into water-dispersible hydrophilic nanoparticles using PEGylation method (Supplementary xx). The PEGylated CeO₂/Mn₃O₄ exhibited hydrodynamic diameter ranging from 9 to 15 nm in phosphate-buffered saline (PBS) (Figure 3.10).

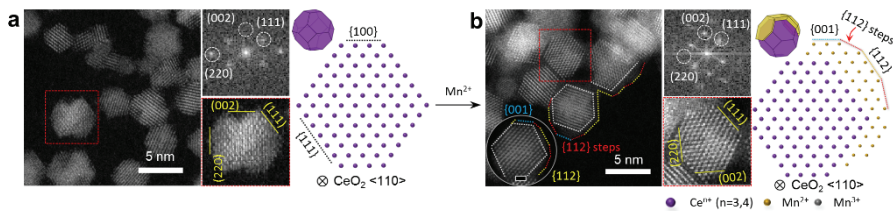


Figure 3.1. a-b, STEM images, corresponding FFT patterns, and two-dimensional illustrations of atomic arrangement viewed along CeO_2 $\langle 110 \rangle$ direction of CeO_2 nanocrystals (a) and $\text{CeO}_2/\text{Mn}_3\text{O}_4$ (b). The morphology of $\text{CeO}_2/\text{Mn}_3\text{O}_4$ in STEM image shows the exposed facets of Mn_3O_4 shells are $\{112\}$ (yellow), $\{112\}$ steps (red), and $\{001\}$ (b).

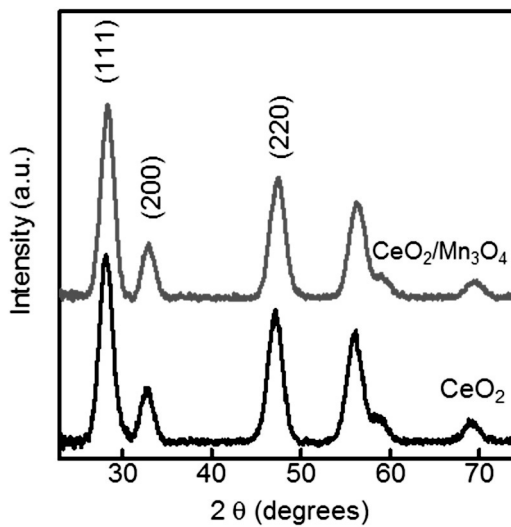


Figure 3.2. XRD patterns of CeO₂ and CeO₂/Mn₃O₄. XRD patterns reveal that the Mn₃O₄ shells were epitaxially grown on CeO₂ nanocrystals.

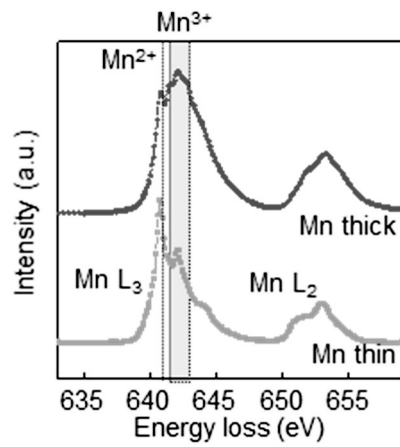


Figure 3.3. XAS analysis showing the formation of $\text{Ce}^{4+}\text{-O-Mn}^{2+}$ polar interface and Mn_3O_4 shells.

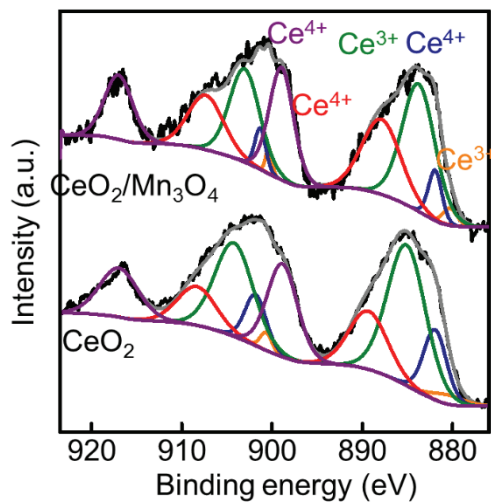


Figure 3.4. Ce 3d XPS spectra showing the oxidation state of Ce. The as-synthesized CeO₂ nanocrystals with 45.8% Ce³⁺ were slightly oxidized to have 41.3% of Ce³⁺ after the reaction with Mn²⁺.

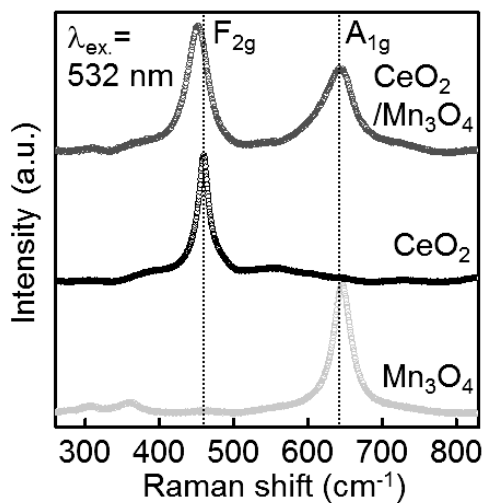


Figure 3.5. Visible Raman spectra show the heterostructure of defective CeO₂ and strained Mn₃O₄, and the presence of higher degree of O-vacancies in CeO₂/Mn₃O₄ than in CeO₂.

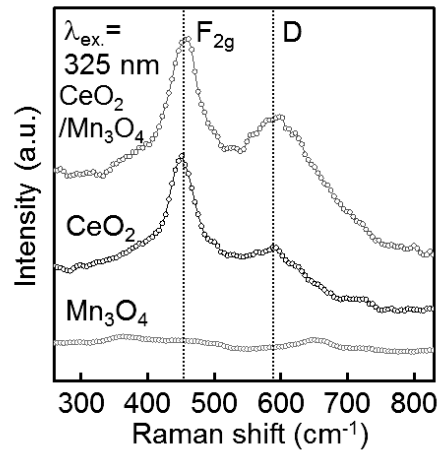


Figure 3.6. UV Raman spectra show the presence of higher degree of O-vacancies in CeO₂/Mn₃O₄ than in CeO₂.

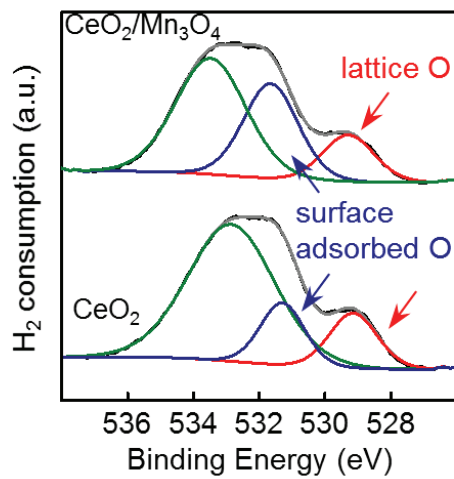


Figure 3.7. O 1s XPS spectra were fitted with O_{latt} (~529.2 eV, red line), O_{ads} (~531.5 eV, blue line), and O_{surf} (533.2 eV, green line).

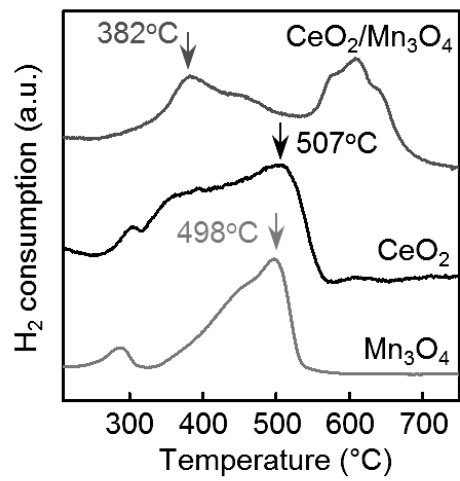


Figure 3.8. H₂-TPR curves comparing CeO₂, CeO₂/Mn₃O₄, and Mn₃O₄.

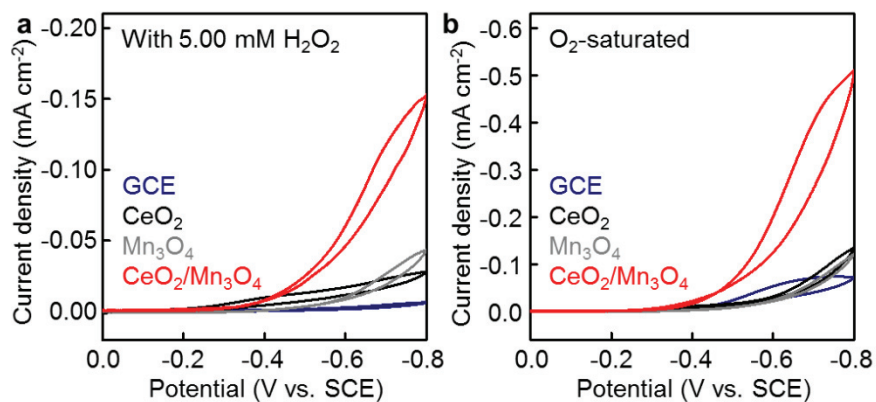


Figure 3.9. a-b), CVs at a scan rate of 50 mV s⁻¹ for H₂O₂ reduction (a), and oxygen reduction (b) in Ar-saturated and O₂-saturated PBS solution (pH=7.4), respectively.

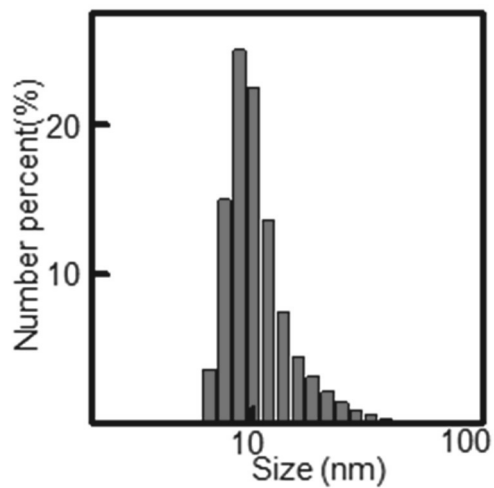


Figure 3.10. Hydrodynamic size of CeO₂/Mn₃O₄ in PBS measured by DLS.

3.3.2 Radioprotective efficacy of CeO₂/Mn₃O₄ on human intestinal organoids

Among the three types of ARS, GI-ARS generally manifests at dose exceeding 6 Gy, and it is highly probable that the patients die within 2~3 weeks.^[22] Clinical manifestations of GI-ARS include destruction of villus and stem cell-containing crypts, leading to the loss of regeneration capacity and epithelial barriers of intestine.^[23] We utilized human intestinal organoid (hIO) model, known to remarkably resemble human intestinal anatomy and physiology, to test the protective capacity of CeO₂/Mn₃O₄ for human GI-ARS.

We cultured hIO dissociates with CeO₂/Mn₃O₄, and then irradiated with 13 Gy. Radical elevation of ROS level in both villus and crypt area of hIO was observed within 6 hrs, but CeO₂/Mn₃O₄ significantly reduced it (Figure 3.11). 12 hrs after the irradiation, apoptotic activity was measured by labeling caspase 3/7. Irradiated hIOs showed significantly increased apoptotic activity but CeO₂/Mn₃O₄-treated hIOs showed dramatically reduced apoptotic area limited to a few peripheral crypts (Figure 3.12). 1 week after the radiation, severe fibrotic changes with decreased E-cadherin expression was observed and no additionally budded crypt

was found in the survived hIOs. (Figure 3.13). This result indicates that the radiation not only damaged regenerative stem cells in crypts but also induced transcriptional modulations and phenotypic changes such as fibrosis. However, IR+CM+ (CM denotes CeO₂/Mn₃O₄) groups showed newly formed crypts and intact epithelial morphology, indicating that CeO₂/Mn₃O₄ prevent stem cell death and radiation-induced gene expression changes (Figure 3.13). To scrutinize these phenotypic changes in genetic levels, we performed mRNA sequencing at 12 hrs post-IR. In total, expression levels of 261 genes (116 genes upregulated, 145 genes downregulated) were significantly altered after the IR, but only 66 genes (50 genes upregulated, 16 genes downregulated) showed significant expressional changes in IR+CM+ groups (Figure 3.14). Hierarchical clustering dendrogram also indicated that the global gene expression pattern of IR+/CM+ was more similar to that of IR-/CM- groups (Figure 3.15). To compare the gene expression patterns between CeO₂/Mn₃O₄-treated and non-treated irradiated groups, transcriptional expression data of IR+/CM+ over IR+/CM- was plotted against log₂ fold change and volume (Figure 3.16). Considering fold change and volume, five most significantly changed genes were e

xtracted (4 genes upregulated, 1 gene downregulated), and interestingly, we found that MT1G and MT2A genes were highly upregulated in the IR+CM+ groups (Figure 3.16). They are belonging to the metallothionein (MT) gene superfamily, which are known to have strong anti-oxidant function that protects various cell types such as embryo, macrophage, and myocardial cells from wide variety of ROS including superoxide, hydroxyl radicals, and hydrogen peroxides. We assume that antioxidant response elements of MT genes might be activated by CeO₂/Mn₃O₄, which possibly had mildly altered intracellular redox status without harming cells. We analyzed the radiation-induced transcriptional modulation based on functions of genes expected to be critical for damage repairing and proper proliferation of hIO. Among the gene ontology (GO) terms showing p-value less than 0.05, GO terms related to GI-ARS including “oxidative stress” (p=0.00429), “canonical Wnt pathway” (p=0.00469), “cell division” (p=1.3E-45), and “apoptotic process” (p=2.6E-19) (Figure 17a, b, c, d) were selected. Then, we further isolated genes showing more than 2 fold change in IR+/CM+ over IR+/CM- comparison. In oxidative stress GO, DUOX2, known as a hydrogen peroxide generator making cells more prone to radi

ation, was 8 folds upregulated in IR+/CM- groups, but only 3.4 folds upregulated in IR+/CM+ groups (Figure 3.17a). In canonical Wnt pathway, LGR5 is a marker for intestinal stem cell residing in crypts. LGR5+ stem cells are highly radio-sensitive, but are indispensable for regenerating radiation-induced intestinal damage. Expression level of LGR5 was 5.1 folds downregulated in IR+/CM- groups, but only 1.34 folds downregulated in IR+/CM+ groups (Figure 3.17b). Since stem cells in intestine should undergo active mitosis to replace radiation-damaged epithelial cells, genes related to cell division and apoptotic process were also examined to assess the regenerative capacity of hIO. Numerous cell cycle-promoting genes such as CDC20, CDC25C, CCNB1, and CCNB2 were downregulated (> 2 folds) in IR+/CM- groups but significantly less downregulated in IR+/CM+ groups when compared to IR-/CM- groups (< 2folds) (Figure 3.17c). Transcriptional levels of death receptors such as TNFRSF9, and pro-apoptotic proteins such as TP53, INP1, RRM2B, and PLK3 were more than 2 folds upregulated, but anti-apoptotic proteins including PLK1, BUB1, BIRC5, and AURKB were more than 2 folds downregulated in IR+/CM- groups when compared to IR-/CM- groups. In contrast, none of those ge

nes were up- or down-regulated more than 2 folds in IR+/CM+ groups when compared to IR-/CM- (Figure 3.17d). Based on these results, CeO₂/Mn₃O₄ successfully protected various cell populations in hIOs from radiation damages by directly scavenging radiation-generated ROS. By doing so, CeO₂/Mn₃O₄ minimized radiation-induced transcriptional modulations which might have caused long-term damages or cellular alternations. We also confirmed that the stem cells protected by CeO₂/Mn₃O₄ maintained their functions and thus capable of restore damaged intestinal epithelia.

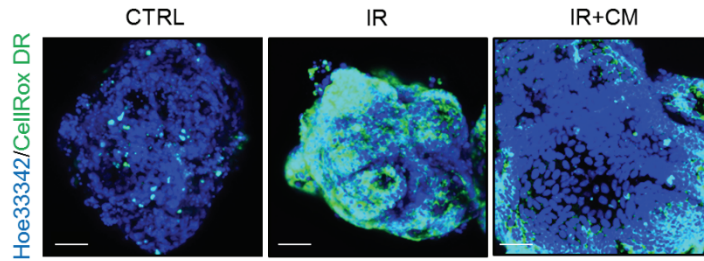


Figure 3.11. a) Cystic stage hIOs are irradiated with 13 Gy IR, and ROS levels are visualized by loading CellRox Deep Red (n=4).

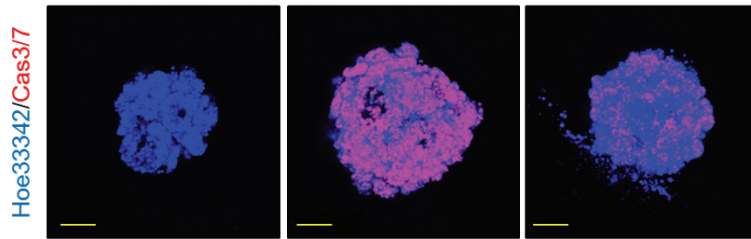


Figure 3.12. 12 hrs after IR, apoptotic rates are measured by CellEvent Caspase 3/7 assay (n=4).

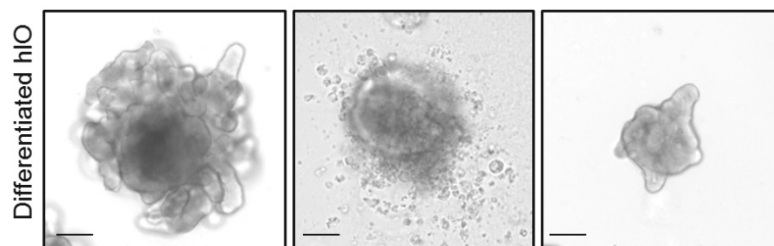


Figure 3.13. 144 hrs after IR, morphology of hIOs is assessed. Red triangles indicate area showing fibrotic change and black triangles indicate crypt budding (n=4).

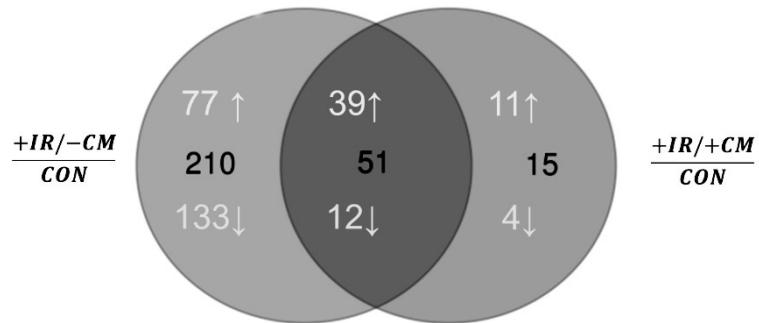


Figure 3.14. 12hrs after IR hIOs are subjected to mRNA sequencing. Number of genes transcriptionally up- or down-regulated compared to control group is counted and expressed as a venn diagram (n=3).

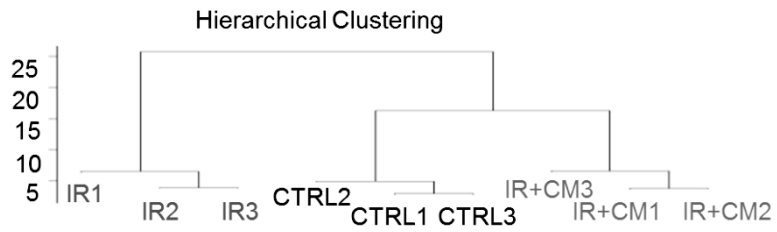


Figure 3.15. Hierarchical clustering based on expressional similarity is expressed as a dendrogram (n=3).

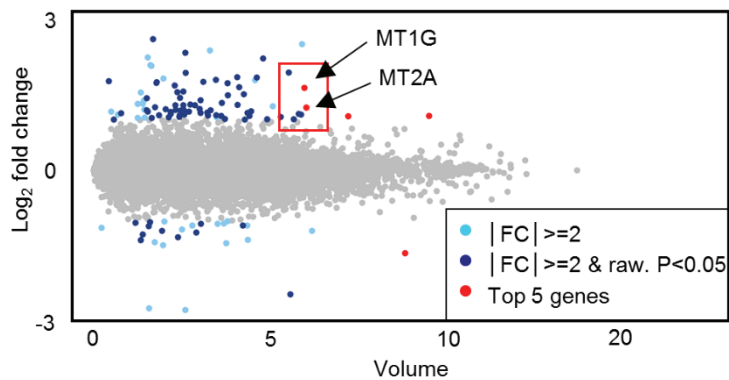


Figure 3.16. log₂ fold transcriptional changes of total mRNAs are scatter plotted against expressional volume. Red dots are top 5 most significantly altered genes in transcriptional level. MT1G and MT2A are categorized as an antioxidant enzyme and SULT2A1 and CYP3A4 are categorized as a drug metabolism-related genes (n=3).

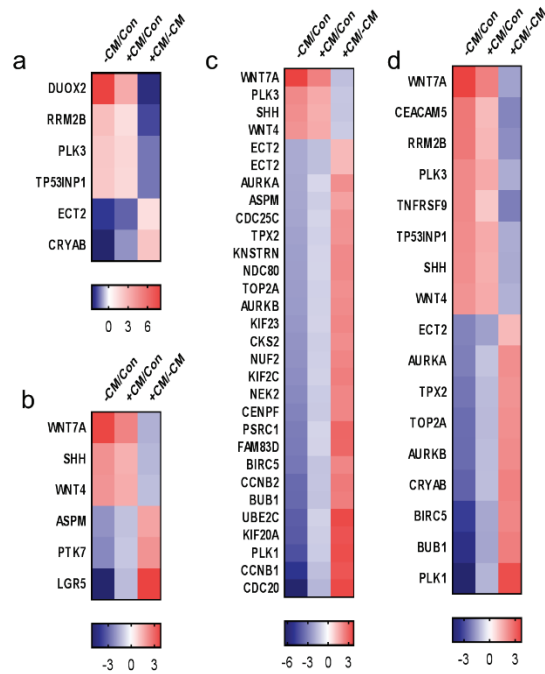


Figure 3.17. a-d) Genes showing more than two-fold transcriptional change in +CM+IR/-CM+IR are selected and re-analyzed according to the transcriptional fold changes of -CM+IR/Con and +CM+IR/Con. Fold changes are expressed as heatmaps and the selected genes are clustered based on GO terms (a: Response to oxidative stress, b: Canonical Wnt pathway, c: Cell division, d: Apoptotic process. (n=3). Images in each corresponding group were equally enhanced in PowerPoint to provide visual clarity.

3.3.2 Mitigation of radiation-induced multi-organ damages by CeO₂/Mn₃O₄ *in vivo*

We further examined the systemic radio-protection capacity of CeO₂/Mn₃O₄ *in vivo*. First systemic biocompatibility of CeO₂/Mn₃O₄ was assayed. No abnormal histological alternations in organs (intestine, kidney, spleen, liver, heart, lung, and bladder) or body weight loss are observed up to 30 days after the injection of high dose CeO₂/Mn₃O₄ (50 mg/kg), indicating that CeO₂/Mn₃O₄ do not have notable systemic toxicity (Figure 3.18). We then tested the systemic radio-protection ability of CeO₂/Mn₃O₄ under 0.55mg/kg concentration, which is 1/100 of CeO₂/Mn₃O₄ concentration used in the toxicity test. Mice are subjected to TBI with 13 Gy after the injection of CeO₂/Mn₃O₄ (Figure 3.19). Survival rate of mice in IR+/CM- group is drastically decreased to 50% at 12 days post-TBI and at the point of 15 days after TBI, all mice are dead. However 10 mice are survived in IR+/CM+ group at the 150 days after TBI (Figure 3.20). To figure out the factors that contributed to the increased survival of CeO₂/Mn₃O₄-pretreated group, we mainly focus on the mitigation of total body inflammatory cytokine and ROS levels, H-ARS, and GI-ARS.

It has been known that acute ROS production by TBI spontaneously

induces macrophage-dependent cytokine release, which may cause fatigue and other inflammatory cascades. As expected, significant acute increase of serum cytokines including interleukin-1beta (IL-1b), interleukin 6 (IL6), and tumor necrosis factor-alpha (TNF-a) was observed 2hrs after TBI. However, in IR+CM+ groups, none of three cytokines was significantly increased compared to IR-CM- groups (Figure 3.21). Total body ROS levels were measured by quantifying malondialdehyde (MDA), a toxic substance produced by lipid peroxidation, of plasma and five critical organs. One day after TBI, in plasma, IR+CM- groups showed 55% lower MDA level than IR+CM- groups (Figure 3.22). Four days after TBI, MDA levels of 5 organs including small intestine, liver, kidney, spleen, and lung are measured. Except for liver, all other organs show significantly increased MDA level after the TBI in IR+CM- groups. However no statistically significant increase in tissue MDA level was observed in IR+CM+ groups (Figure 3.23).

To assess hematopoietic damages, we first measured ROS levels of BMC 30 min after TBI. Compared to IR-CM- groups, IR+CM- groups showed three-fold increase in ROS level, but IR+CM+ groups showed significantly lower increase (1.8 folds) than IR+CM- groups (Figure 24 a

and b). One day after TBI total BMCs are also isolated and counted. Almost 95% of BMCs are ablated in IR+CM- groups, but only average of 50% of BMCs was ablated in IR+CM+ groups (Figure 3.25).

We then examined the radiation-induced small intestine damages. One week after TBI, integrities of villus were severely damaged in IR+CM- groups, but IR+CM+ groups showed relatively intact villus structure, preserving longer villus length than IR+CM- groups (Figure 3.26a and b). TUNEL assay and Ki-67 staining results also revealed that CeO₂/Mn₃O₄ can protect both villus and crypt cells from IR, maintaining mitotic activity of stem and progenitor cells in crypts (Figure 3.27a and b). To confirm regenerative capacity of crypt cells after IR, we isolated crypts from mouse 30 min after TBI, and cultured them in in-vitro organoid culture condition. Intestinal organoids from IR+CM+ groups presented normal organoid phenotypic characteristics including central lumen, crypt budding, and villus, but crypts from IR+CM- groups could not even form spherical cyst for 7 days of culture (Figure 3.28a). Therefore, success rate of crypts forming organoid is drastically decreased in IR+CM- groups, but it was significantly improved in IR+CM+ groups comparable to the IR-CM- groups (Figure 3.28b).

Finally, we conducted long-term damage assessment by harvesting organs from survived CeO₂/Mn₃O₄-pretreated mice 150 days after TBI. Both duodenum and jejunum of survivors showed no sign of tumorigenesis or pathogenesis. There was no significant difference in crypt number or fibrotic change observed in survivors compared to the control group (Figure 3.29). No sign of lung fibrosis was observed in survivors and survivors showed no significant difference in liver, spleen, and kidney histology compared to control group (Figure 3.30).

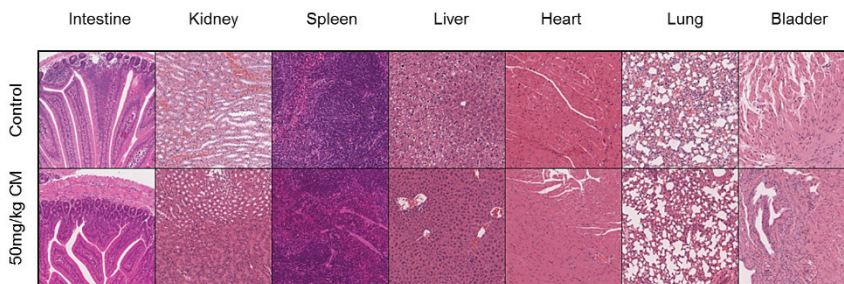
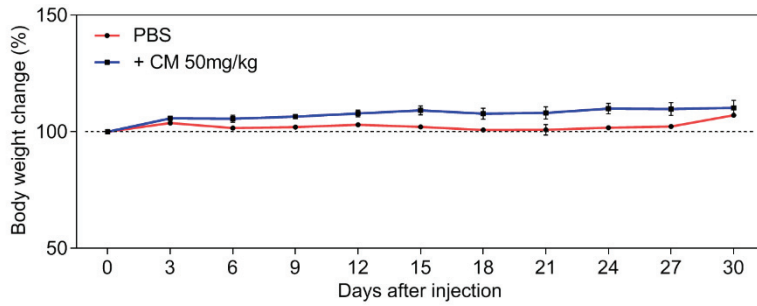


Figure 3.18. *In vivo* toxicity analysis by measuring weight changes and histology analysis in various organs.

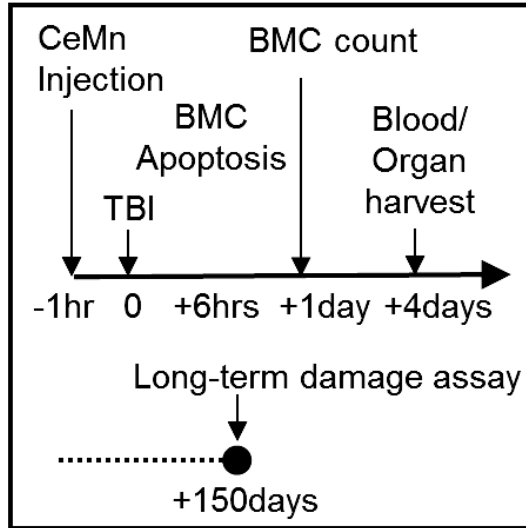


Figure 3.19. Timeline for in vivo radioprotection assays.

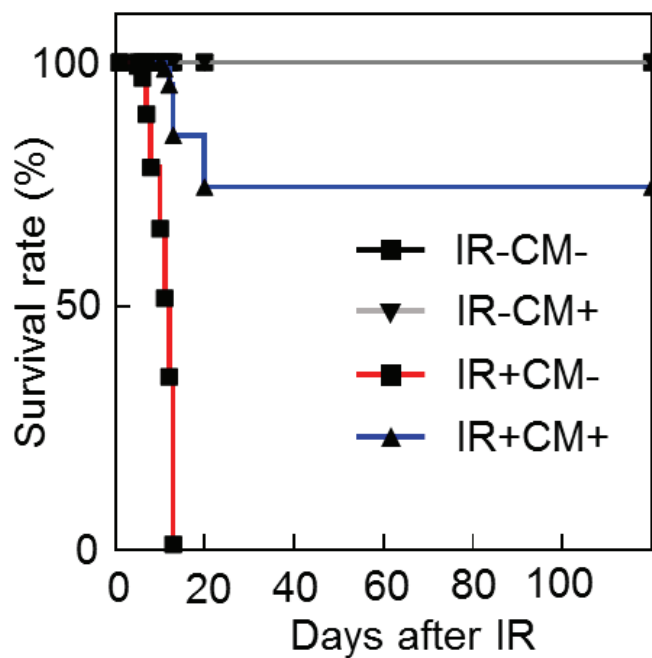


Figure 3.20. Kaplan meier survival graph for IR-CM+, IR-CM+, IR+CM-, and IR+CM+ groups after 13 Gy TBI up to 120 days. (n=15).

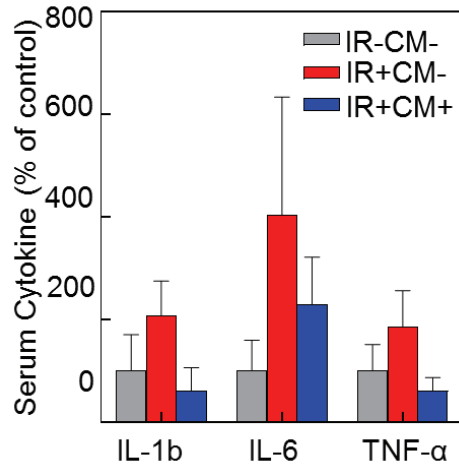


Figure 3.21. Serum IL-1b, IL-6, TNF-a levels were quantified 2 hrs after TBI. (n=5).

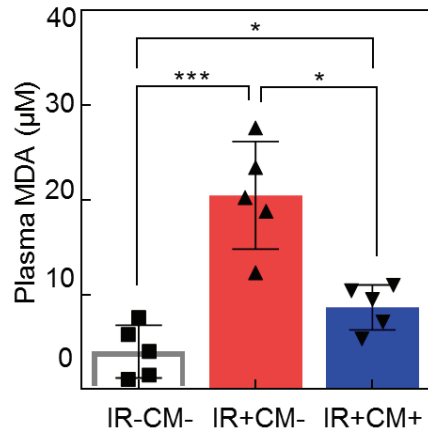


Figure 3.22. Acute blood ROS level was estimated by quantifying plasma MDA levels one day after TBI (n=5).

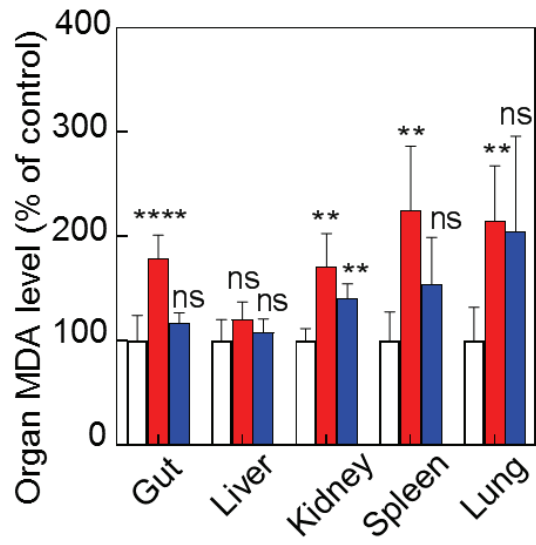


Figure 3.23. MDA levels in five critical organs were quantified (n=5).

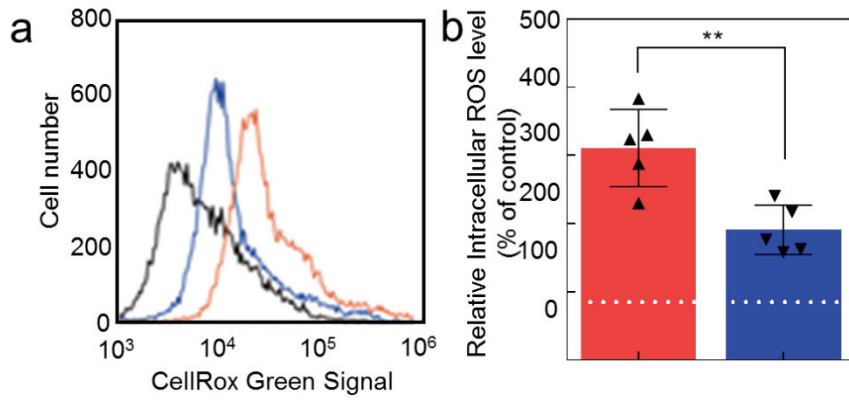


Figure 3.24. a) Intracellular ROS levels of BMC were measured by FACS with CellRox Green 6 hrs after TBI (n=5). b) Relative Intracellular ROS levels of BMC were quantified based on the FACS results. IR-CM- as 100% (n=5).

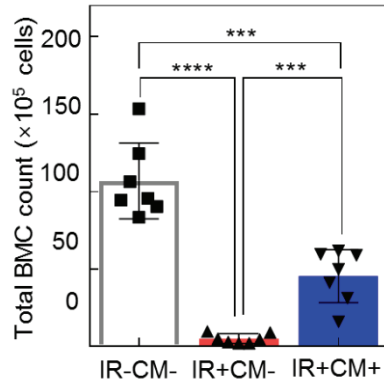


Figure 3.25. Total number of live BMCs extracted from tibia are counted by Trypan blue assay (n=7).

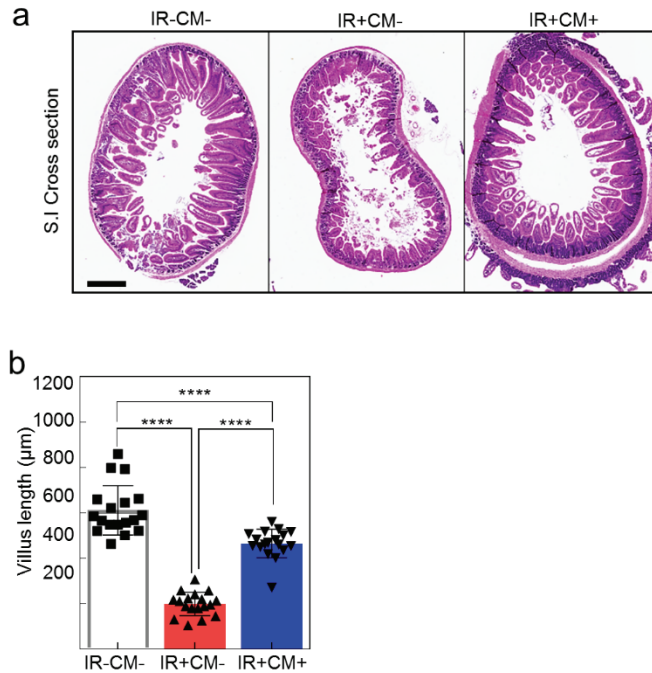


Figure 3.26. a) Intestinal villus morphologies are visualized by H&E staining in cross-sectional view. Scale bar = 1mm (n=5). b) Based on villus length is measured in (a) (n=18).

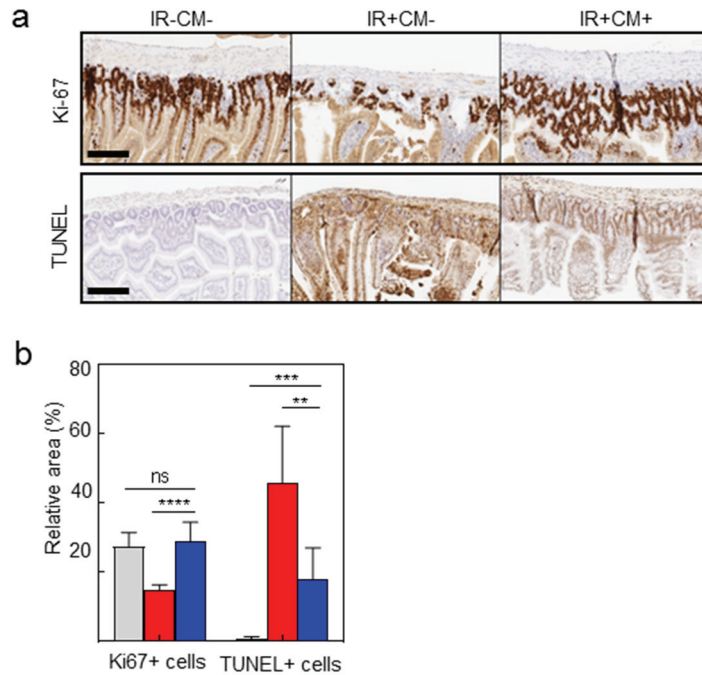


Figure 3.27. a) Ki67 is stained to visualize proliferative stem cells in crypts, and TUNEL is for apoptosis assessment. Scale bar = 200 μ m (n=5). b) Ki67+ and TUNEL+ areas per field are quantified based on the images from Figure 3f (n=7).

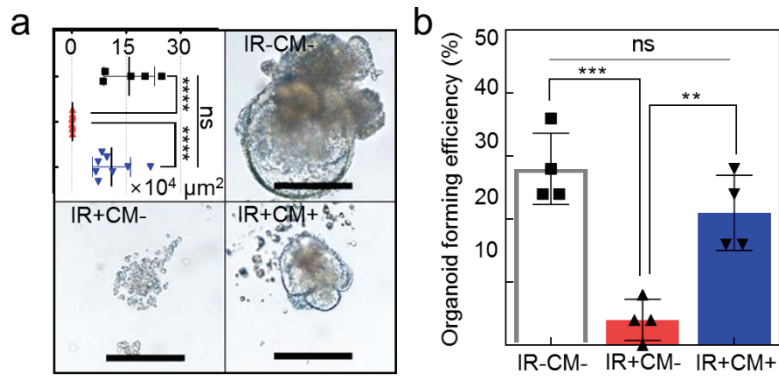


Figure 3.28. Number of organoids formed per 1000-seeded crypts is counted and expressed as percentage (n=4). *: $p < 0.05$, **: $p < 0.01$, ***: $p < 0.005$, Images in each corresponding group were equally enhanced in PowerPoint to provide better visual clarity.

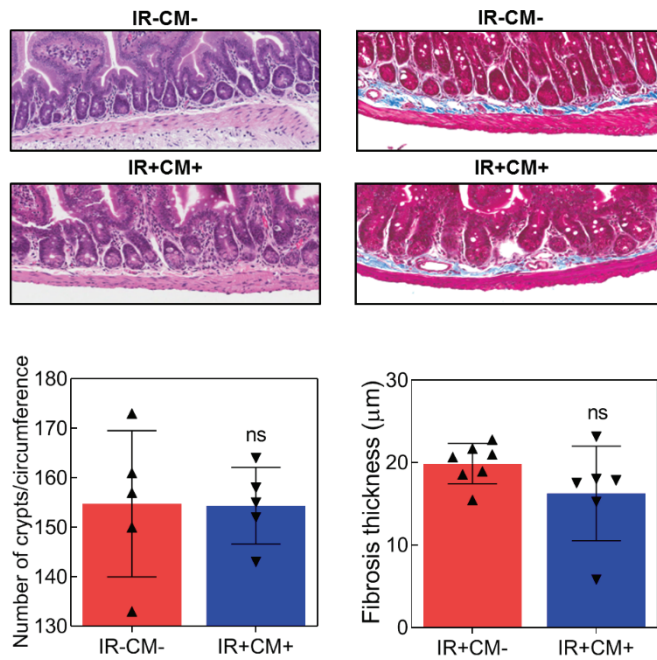


Figure 3.29. Long term toxicity analysis. Crypt number or fibrotic change was analyzed by histology

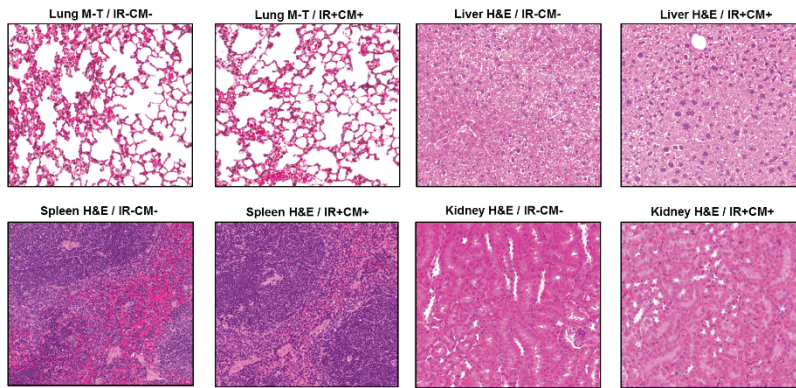


Figure 3.30. Long term toxicity in key organs. Fibrosis was analyzed in key organs using histology analysis.

3.4 Conclusion

In conclusion, we report a highly catalytic $\text{CeO}_2/\text{Mn}_3\text{O}_4$ that exhibit powerful antioxidant activity to protect from ROS induced IR damage. The Mn ions is deposited to CeO_2 nanocrystal to synthesize heterostructured $\text{CeO}_2/\text{Mn}_3\text{O}_4$. The Mn ions induces oxygen vacancies on CeO_2 surface which increases oxygen adsorption efficiency. Moreover Mn_3O_4 grown on the surface of CeO_2 nanocrystal is epitaxially strained, and the surface catalytic activity is tuned so that catalytic performance can be further enhanced. This characteristics boosts antioxidant activity of nanocrystal, and effectively protects from ROS induced IR damage with very small effective dose. $\text{CeO}_2/\text{Mn}_3\text{O}_4$ are utilized as a radio-protectant to protect ARS induced by TBI. In the hIO model, we successfully demonstrated protection of regenerative intestinal stem cells, and further confirmed by mRNA sequencing. Furthermore, in mouse model, $\text{CeO}_2/\text{Mn}_3\text{O}_4$ could effectively improve survival rate from TBI by mitigating both hematopoietic and gastrointestinal manifestations. These highly catalytic $\text{CeO}_2/\text{Mn}_3\text{O}_4$ are poised to create new possibilities for next-generation radio-protectant.

**Most of the contents of this chapter will be published in the article,
“Heterostructured Ceria-Manganese Oxide nanocrystals as an
Antioxidant for mitigation of Acute Radiation Syndrome.” (*In
preparation*)

3.5 References

- [1] I. O. Djordjevic, D. Trivanovic, M. Jovanovic, M. Ignjatovic, B. Secerov, M. Mojovic, D. Bugarski, G. Bacic, P. R. Andjus, *Croat Med J.* **2014**, *55*, 45.
- [2] M. M. Garau, A. L. Calduch, E. C. Lopez, *Rep. Pract. Oncol. Radiother.* **2011**, *16*, 123.
- [3] T. B. Elliott, N. E. Deutz, J. Gulani, A. Koch, C. H. Olsen, C. Christensen, M. Chappell, M. H. Whitnall, M. Moroni, *Comp Med.* **2014**, *64*, 456.
- [4] M. Lopez, M. Martin, *Rep Pract Oncol Radiother.* **2011**, *16*, 138.
- [5] J. F. Hainfeld, F. A. Dilmanian, D. N. Slatkin, H. M. Smilowitz, *J. Pharm. Pharmacol.* **2008**, *60*, 977.
- [6] J. Colon, N. Hsieh, A. Ferguson, P. Kupelian, S. Seal, D. W. Jenkins, C. H. Baker, *Nanomedicine* **2010**, *6*, 698.
- [7] D. J. Grdina, J. S. Murley, Y. Kataoka, *Oncology* **2002**, *63*, 2.
- [8] J. Wu, X. Wang, Q. Wang, Z. Lou, S. Lu, Y. Zhu, L. Qin, H. Wei, *Chem. Soc. Rev.* **2019**, *48*, 1004.
- [9] C. K. Kim, T. Kim, I-Y. Choi, M. Soh, D. Kim, Y-J. Kim, H. Jang, H-S. Yang, J. Y. Kim, H-K. Park, S. P. Park, S. Park, T. Yu, B-W.

- Yoon, S-H. Lee, T. Hyeon, *Angew. Chem. Int. Ed.* **2012**, *51*, 11039.
- [10] H. J. Kwon, M-Y. Cha, D. Kim, D. K. Kim, M. Soh, K. Shin, T. Hyeon, I. M. Jung, *ACS Nano* **2016**, *10*, 2860.
- [11] H. J. Kwon, D. Kim, K. Seo, Y. G. Kim, S. I. Han, T. Kang, M. Soh, T. Hyeon, *Angew. Chem. Int. Ed.* **2018**, *130*, 9552.
- [12] N. Singh, M. A. Savanur, S. Srivastava, P. D'Silva, G. Muges, *Angew. Chem. Int. Ed.* **2017**, *56*, 14267.
- [13] J. Yao, Y. Cheng, M. Zhou, S. Zhao, S. Lin, X. Wang, J. Wu, S. Li, H. Wei, *Chem. Sci.* **2018**, *9*, 2927
- [14] Z. Chen, J-J. Yin, Y-T, Zhou, Y. Zhang, L. Song, M. Song, S. Hu, N, Gu, *ACS Nano* **2012**, *5*, 4001.
- [15] A. A. Vernekar, D. Sinha, S. Srivastava, P. U. paramasivam, P. D'Silva, G. Muges, *Nat. Commun.* **2014**, *5*, 5301.
- [16] S. Shibuya, Y. Ozawa, K. Watanabe, N. Izuo, T. Toda, K. Yokote, T. Shimizu, *PLoS ONE* **2014**, *9*, e109288
- [17] C. Xu, X. Qu, *NPG Asia Materials* **2014**, *6*, e90.
- [18] L. Bu, N. Zhang, S. Guo, X. Zhang, J. Li, J. Yao, T. Wu, G. Lu, J-Y. Ma, D. Su, X. Huang, *Science* **2016**, *354*, 1410.
- [19] M. Luo, S. Guo, *Nat. Rev. Mater.* **2017**, *2*, 17059.

- [20] H. Wang, S. Xu, C. Tsai, Y. Li, C. Liu, J. Zhao, Y. Liu, H. Yuan, F. A. Pedersen, F. B. Prinz, J. K. Norskov, Y. Cui, *Science* **2016**, *354*, 1031
- [21] P. Strasser, S. Koh, T. Anniyev, J. Greeley, K. More, C. Yu, Z. Liu, S. Kaya, D. Nordlund, H. Ogasawara, M. F. Toney, A. Nilsson, *Nat. Chem.* **2010**, *2*, 454
- [22] C. Booth, G. Tudor, J. Tudor, B. P. Katz, T. Macvittie, *Health Phys.* **2012**, *103*, 383.
- [23] S. Umar, *Curr Gastroenterol Rep.* **2010**, *12*, 340.

Bibliography

1. Journal Publication

- 1) Suji Choi[⊥], **Sang Ihn Han**[⊥], Dongjun Jung[⊥], Hye Jin Hwang[⊥], Chaehong Lim, Soochan Bae, Ok Kyu Park, Cory M. Tschabrunn, Mincheol Lee, Sun Youn Bae, Ji Woong Yu, Ji Ho Ryu, Sang-Woo Lee, Kyungpyo Park, Peter M. Kang, Won Bo Lee, Reza Nezafat, Taeghwan Hyeon*, and Dae-Hyeong Kim*, “Highly conductive, biocompatible, and soft nanocomposite using ultralong Ag-Au core-sheath nanowires.” Nat. Nanotechnol., 13, 1048 (2018).

([⊥]**These authors contributed equally to this work**)

- 2) Suji Choi[⊥], **Sang Ihn Han**[⊥], Dokyoon Kim[⊥], Taeghwan Hyeon,* and Dae-Hyeong Kim*, “High-performance stretchable conductive nanocomposites: materials, processes, and device applications.” Chem. Soc. Rev., 48, 1566 (2019).

([⊥]**These authors contributed equally to this work**)

- 3) Ji Eun Lee, Seung-Ho Yu, Dong Jun Lee, Dong-Chan Lee, **Sang Ihn Han**, Yung-Eun Sung, Taeghwan Hyeon, “Facile and economical synthesis of hierarchical carbon-coated magnetite nanocomposite particles and their applications in lithium ion battery anodes” *Energy Environ. Sci.*, 5, 9528 (2012)

- 4) Mohammadreza Shokouhimehr, Ji Eun Lee, **Sang Ihn Han**, Taeghwan Hyeon, “Magnetically recyclable hollow nanocomposite catalysts for heterogeneous reduction of nitroarenes and Suzuki reactions.” *Chem. Commun.*, 49, 4779 (2013).

- 5) Kwangsoo Shin, Jin Woo Choi, Giho Ko, Seungmin Baik, Dokyoon Kim, Ok Kyu Park, Kyoungbun Lee, Hye Rim Cho, **Sang Ihn Han**, Soo Hong Lee, Dong Jun Lee, Nohyun Lee, Hyo-Cheol Kim, Taeghwan Hyeon, “Multifunctional nanoparticles as a tissue adhesive and an injectable marker for

image-guided procedures.” *Nat. Commun.*, 8, 15807 (2017)

- 6) Dokyoon Kim, Hyek Jin Kwon, Kwangsoo Shin, Jaehyup Kim, Roh-Eul Yoo, Seung Hong Choi, Min Soh, Taegyu Kang, **Sang Ihn Han**, Taeghwan Hyeon, “Multiplexible Wash-Free Immunoassay Using Colloidal Assemblies of Magnetic and Photoluminescent nanoparticles.” *ACS Nano*, 11, 8448 (2017)
- 7) Hyek Jin Kwon, Dokyoon Kim, Kyungho Seo, Young Geon Kim, **Sang Ihn Han**, Taegyu Kang, Min Soh, Taeghwan Hyeon, “Ceria nanoparticle systems for selective scavenging of mitochondrial, intracellular, and extracellular reactive oxygen species in Parkinson's disease.” *Angew. Chem. Int. Ed.*, 56, 11399 (2017)

초 록

나노재료는 나노 크기일 때 나타나는 독특한 성질 때문에 의료, 촉매, 스트레처블 디바이스를 포함한 다양한 분야에서 활용되고 있다. 의료분야에서 나노재료의 활용에서 가장 큰 관심사 중 하나는 독성 문제이다. 효과적인 접근법은 나노재료의 성능을 극대화하여 투여 농도를 최소화 하거나 독성이 없는 이차 물질을 이용하여 기존에 독성이 있던 나노물질의 독성을 낮추는 방법이 있다.

최근에는 이중금속 나노재료를 활용하여 성능을 극대화하거나 기존 단일 금속 나노물질이 가지고 있던 단점을 보완하는 연구가 활발하게 진행되고 있다.

첫 번째는 이중금속 금-은 나노와이어를 활용한 높은 전도도와 신축성, 그리고 생체친화성을 갖는 나노복합체의 제작과 생체전자공학으로의 응용에 관한 연구이다. 은나노와이어는 높은 전도도와 대량생산이 가능하다는 장점 때문에 높은 전도성을 갖는 나노복합체에 많이 사용이 되어왔다. 하지만 은의 독성 때문에 바이오메디컬 기기

활용에는 한계가 있었다. 이번 연구에서 은나노와이어의 표면에 금을 갈바닉 교환반응을 억제하면서 코팅을 해줌으로써 높은 전도도를 가지면서 생체 친화적인 나노복합체를 만들 수 있었다. 이는 웨어러블 전극과 체내침습용 생체 전극으로 활용하여 돼지모델에서 심장 신호를 측정할 수 있었다.

두 번째는 방사선 보호를 위한 연구로, 나노효소의 항산화 성질을 이용해 방사선 피폭 시 과량 생성되는 활성산소를 줄이는 연구이다. 일반적으로 세리아 나노입자는 뛰어난 항산화 성질 때문에 활성산소 제거를 요하는 질병모델에 많이 사용되어 왔다. 하지만 무기화합물의 독성문제는 아직 해결해야 할 문제이며 획기적인 접근법으로 나노입자의 성능을 극대화해 투여량을 최소화함으로써 부작용을 줄이는 방법이 있다. 본 연구에서 세리아 표면에 망간나노입자를 형성시켜 망간 표면에는 격자 압력을 가해 표면 촉매활성을 증가시키고 세리아 표면에는 산소 공극을 증가시켜 촉매활성을 증가시켰다. 이러한 시너지효과로 인해 세리아-망간 이중금속 나노입자는 매우 뛰어난 항산화 성질을 보여주었고 적은 투여량으로도 높은 효과를 낼 수 있었다. 세리아-망간 이중금속 나노입자는 인간 오가노이드 모델에서

방사선 보호효과를 보여주었고 추가적인 쥐 모델에서도 보호효과를 관찰할 수 있었다.

주요어: 나노입자, 이중금속, 나노바이오기술, 스트레처블 디바이스, 코어-셸, 나노와이어

학 번: 2014-30265